Transient High-Pressure Hydrogen Jet Measurements

by

Benjamin R. Petersen

A thesis submitted in partial fulfillment
of the requirements for the degree of

Master of Science
(Mechanical Engineering)

at the
UNIVERSITY OF WISCONSIN-MADISON
2006

Abstract

Jets produced by prototype multi-hole gaseous injectors were visualized using schlieren methods. Hydrogen and helium were injected at pressures ranging from 1.3 bar to 104 bar into chamber densities ranging from 1.15 to 12.8 kg/m^3, resulting in jets spanning from subsonic to highly underexpanded conditions. The jet tip penetration rate was found to increase with injection pressure, and decrease with increasing chamber density, as expected. The jet angle was also measured, but variability in the results restricted the quantitative assessment of trends.

The complex expansion and shock structures within the underexpanded jets were clearly visible, and the distance between the expansion wave fronts was found to scale directly with the ratio of the exit to chamber pressure.

Two injector characteristics, the discharge coefficient and rate shape, were measured to describe injector performance. The discharge coefficient was found to range from 0.19 to 0.33, while the rate shape displayed “top hat” behavior for all conditions tested.

Five normalization models that included the effects of expansion outside the nozzle, jet angle variation, and discharge coefficient variation were investigated to analyze their importance in the collapse of the penetration rate data from the three- and seven-hole injectors.. The nondimensional penetration was found to be linearly dependent on the square root of the nondimensional time, indicating self-similar behavior for each investigated normalization scheme. The uncertainty of the slopes of individual runs was quantified and was found to vary for each method, with no clearly superior method.

Acknowledgements

I would first like to thank Professor J.B. Ghandhi for his invaluable guidance throughout this research. He has shown infinite patience in my progress as a graduate student and has provided me with opportunities that I could never repay him for.

I thank the faculty and staff of the Engine Research Center for their assistance during my two years working with them. A special thanks goes to Ralph Braun for helping me in my machining endeavors. I would also like to thank Victor Salazar and Nate Haugle for making room 118 a fun place to learn and work.

A simple "thank you" does not describe the appreciation I have for all the things my family has done for me. My brother, Bob Petersen, has been my best friend my entire life and continues to be a person I can always turn to. My sister, Sarah Petersen, continually amazes me with her incredible strength and determination as a person. My grandparents, Bob and Gladys Herr, have provided a strong foundation for our family and have two of the biggest hearts in the world. Finally, my mother, LuRae Petersen, is the true inspiration in my life. She has taught me endless lessons even when she thought I wasn't listening. I would truly not be the person I am today without her.

A very special thanks also goes to Alexis Endicott for putting up with a graduate student boyfriend and the absence associated with it. She brings a smile to my face and love into my heart each and every day. I could not have accomplished what I did in the past two years without her.

This study was funded by Ford Motor Company

Table of Contents

List of Tables

List of Figures

Nomenclature

a	constant that relates the measured value of spray or jet angle to the value used in integral control volume model
A_{eq}	area of jet using the equivalent diameter
a_c	length of source image not cutoff by knife edge
A_n	nozzle exit area
$A_{p,Z/2}$	projected area of a jet along axial distance of one half the penetration distance
C	image contrast
C_a	orifice contraction coefficient
C_d	discharge coefficient
C_f	fraction of steady centerline velocity where penetration is defined
C_t	relates turbulent diffusivity to kinematic momentum flux
C_v	orifice velocity coefficient
c_v	specific heat at constant volume
D	head vortex diameter
d_{eq}	equivalent diameter
d_n	nozzle exit diameter
d_f	nozzle diameter corrected with orifice area contraction coefficient
E	background illuminance
f_1	focal length of the initial parabolic mirror in the z-type schlieren system
f_2	focal length of the second parabolic mirror in the z-type schlieren system
h_0	enthalpy of initial state
K	entrainment constant
K_s	entrainment constant
k_d	experimental constant for centerline velocity decay
L	length of schlieren object along optical axis
l_{barrel}	barrel length
$\dot{M}$	momentum flux
$\dot{m}$	instantaneous mass flow rate of injection
$\dot{m}_{actual,ave}$	averaged actual mass flow rate from injector
$\dot{m}_{ideal}$	ideal average mass flow rate from injector
m	entrained mass
m_0	jet fluid mass
n	local index of refraction
N	nozzle exit to chamber pressure ratio
n_0	index of refraction of surrounding medium
P	pressure

P_{ch}	ambient chamber pressure
P_n	nozzle exit pressure
P_0	stagnation pressure
P_1	pressure at initial state
P_2	pressure after injection
$\dot{Q}$	heat flux
R	ideal gas constant
r	radial position
s	ratio of head vortex diameter to jet tip penetration
S	contrast sensitivity
S_c	constant used in image processing algorithm that improves contrast
T	temperature
t	time
t_{inj}	injection duration
T_n	nozzle exit temperature
t_n^+	characteristic time scale using nozzle exit parameters for jets with densities differing from the chamber fluid
$\overline{t}_{n,\theta}$	nondimensional time that includes spray or jet angle variation for jets with nonuniform density with chamber fluid
$t_{n,\theta}^+$	characteristic time scale that includes the spray or jet angle variation for jets with nonuniform density with chamber fluid
$\overline{t}_{n,\rho}$	nondimensional time for jets with the same density as the chamber fluid
$t_{n,\rho}^+$	characteristic time scale using nozzle exit parameters for jets with the same density as the chamber fluid
T_0	stagnation temperature
u	internal energy
$U(r,z)$	self-similar velocity profile
U_{CL}	jet centerline velocity
u_f	exit velocity of fluid corrected by orifice velocity coefficient
u_n	nozzle exit velocity
u^*	fluid velocity at choked conditions
V	volume
y	vertical axis
y_Z	percentage of jet penetration bypassed to measure the angle of the initial quasi-steady jet region
z	distance from the nozzle exit
z^*	distance from the nozzle exit corrected by the virtual origin
Z_f	final value of penetration used in the iterative penetration measurement

z_n^+	characteristic length scale using nozzle exit parameters for jets with densities differing from the chamber fluid
$\overline{z}_{n,\theta}$	nondimensional penetration that includes spray or jet angle variation for jets with nonuniform density with chamber fluid
$z_{n,\theta}^+$	characteristic length scale that includes the spray or jet angle variation for jets with nonuniform density with chamber fluid
$\overline{z}_{n,\rho}$	nondimensional penetration for jets with the same density as the chamber fluid
$z_{n,\rho}^+$	characteristic length scale using nozzle exit parameters for jets with the same density as the chamber fluid
Z_t	jet tip penetration
z_0	virtual origin
Z_1	intial penetration value used in the iterative penetration measurement
α	proportionality constant between nondimensional penetration and nondimensional time
ΔE	change in illuminance
Δm	change in mass
ε	angle that parallel light is redirected due to index of refraction gradient in schlieren system
Γ	proportionality constant used by Hill and Oullette [25] between penetration and time
γ	ratio of specific heats
η	nondimensional radial distance
θ	spray or jet angle of quasi-steady region
θ_f	final value of the spray or jet angle used in the iterative penetration measurement
θ_1	intial value of the spray or jet angle used in the iterative penetration measurement
ρ^*	density under choked conditions
$\tilde{\rho}$	nondimensional density, ratio of nozzle to chamber density
ρ_{ch}	chamber density
ρ_n	nozzle exit density
ρ_0	stagnation density

1.0 Introduction

1.1 Motivations

Reducing emissions has been a primary driving force in recent engine technology development. Carbon-, nitrogen-, and sulfur-based emissions have been linked to many significant health and environmental issues. Carbon dioxide is a greenhouse gas, oxides of sulfur produce acid rain, and carbon monoxide can be lethal. These issues, among many others, have warranted many nations to impose regulatory controls on the production of engine-out emissions. The Clean Air Act's Tier 1 and Tier 2 standards have lowered light duty vehicle carbon monoxide, oxides of nitrogen, and particulate matter emissions significantly over the past decades and newer controls such as the Kyoto Protocol involve reductions in greenhouse gases including carbon dioxide. New engine technologies that reduce emissions and are more fuel efficient need to be developed to relieve the environment of excessive pollution and also comply with increasingly stringent regulations. Adding complexity to the situation is the ever-increasing pressure to reduce our dependency on foreign oil.

Hydrogen-fueled engines are believed to be a possible solution to many of the current emission problems. Hydrogen combustion produces no carbon or sulfur related emissions and its production does not necessarily involve fossil fuels. Initial implementation of hydrogen utilized external mixture control strategies to deliver fuel to the engine. Backfire and pre-ignition problems were found to be prominent and initially caused doubt in hydrogen as a viable fuel [1]. Direct injection has subsequently been shown to significantly reduce or eliminate these combustion anomalies and is currently a primary focus in the development of the hydrogen engine [2].

An important physical process within a directly injected engine is the mixing between the injected fuel and the air within the cylinder. This process essentially controls the combustion and, therefore, understanding the physics behind the injection process is necessary to optimize the overall performance of the direct-injection engine. Current injector designs have multiple small holes in the nozzle tip and utilize high pressures to supply a sufficient amount of hydrogen and promote proper mixing. This results in multiple underexpanded jets issuing into the cylinder and interacting with each other. A fundamental understanding of the important characteristics of jets including time and length scales, penetration history, basic geometry and structure, and underexpansion effects will allow for a better overall understanding of the physical processes within the directly injected hydrogen engine.

1.2 Objectives

The main objective of this research is to develop a better overall understanding of transient turbulent gaseous jets including incompressible, compressible, and underexpanded jets. Underexpanded jets play a crucial role in the combustion inside any direct-injection gaseously fueled engine and an improved understanding will allow for easier combustion optimization along with better, more realistic computer simulations. Since there are a lot of similarities in the structure and scaling between all types of jets, studies done on incompressible and even steady jets provide a basis for understanding and modeling underexpanded transient jets. Additional objectives include the optimization of a schlieren system to clearly image gaseous jets and to determine the rate shape and discharge coefficient of several prototype injectors.

1.3 Approach

Four different injectors with 3, 7, 9, and 13 nozzle holes were used to inject hydrogen and helium jets into a quiescent constant volume chamber. A schlieren optical system in conjunction with a high speed digital camera was used to image the jets at a wide range of injection pressures and chamber gas densities. The highest values of chamber density were comparable to densities seen within typical hydrogen-fueled engines. The jet images were processed to remove static imperfections and penetration and jet angle measurements were subsequently performed. The measurements obtained at a wide range of conditions allowed for underexpanded, compressible, and incompressible jets to be studied. Several penetration rate normalization methods were investigated to determine the proper jet-scaling relations. Each method was tested by quantifying the collapse of the nondimensional data. The mass flow rates as a function of time and discharge coefficients were also measured to determine the main characteristics of each injector.

1.4 Outline

A literature review of hydrogen engine development, gaseous jets, including compressible and incompressible jets, and schlieren systems is provided in Chapter 2. Chapter 3 describes the z-type and double pass schlieren systems used in this study along with the specifications and descriptions of the optical spray chamber used to visualize the jets and the spray chamber used in measuring the discharge coefficients and rate shapes. Chapter 3 also provides an overview of all experimental conditions, measurement techniques, and image processing methods that were used throughout the study. Chapter 4 displays a selection of results and a discussion of important trends seen within the raw

penetration data. Chapter 5 investigates various methods of nondimensionalizing the penetration data and includes the results of the discharge and rate shape measurements. Chapter 6 provides conclusions and recommendations for future studies.

2.0 Literature Review

2.1 Hydrogen Engine Development

Internal combustion engines that utilize hydrogen as either a primary or supplementary fuel have been researched and developed extensively over many years; the main attraction being low total emissions with absolutely no carbon-related emissions. Studies dating back to 1820 by Rev. W. Cecil were conducted to examine the properties of hydrogen as an alternative to petroleum-based fuels. In the 1930's thousands of vehicles were modified to run on hydrogen in Europe and during the World Wars hydrogen was seriously studied because of fear of a possible gasoline shortage. By the 1970's, increasing worries of gasoline shortages and initial fears of the effects of carbon-based pollution prompted increased efforts to develop the hydrogen engine [1]. Hydrogen has unique fuel characteristics relative to typical gasoline and other popular fuels. Table 2.1 shows the main fuel parameters for various fuels [1,3,4].

Table 2.1 Fuel Parameters of Various Popular Fuels [1,3,4].

Parameter	Diesel	Gasoline	Methane	Hydrogen
Density [kg/m^3]	830	730-780	0.72	0.089
Molecular Weight	~170	~110	16.043	2.016
Lower Heating Value [MJ/kg]	42.5	43.5	50	120
Boiling Temperature [C]	180-360	25-215	-162	-253
Ignition Limits [Vol-%]	0.6-5.5	1.0-7.6	5.3-15	4-76
Ignition Limits [λ]	0.5-1.3	0.4-1.4	0.7-2.1	0.2-10
Minimum Ignition Energy [mJ]	0.24	0.24	0.29	0.02
Self-Ignition Temperature [C]	~250	~350	595	585
Diffusion Coefficient [m^2/s]	-	-	1.9×10^{-6}	8.5×10^{-6}
Adiabatic Flame Temp. at Stoich. [C]	2000	1980	1851	2042
Quenching Distance [mm]	-	2	2.03	0.64
Laminar Flame Speed [cm/s]	40-80	40-80	40	200

Some of these fuel characteristics are advantageous for utilization in an engine.

- Wide flammability limits: (4-75% by volume – stoichiometric: 66% by volume) allow for hydrogen engines to run under very lean conditions.
- High flame speed: decreases losses due to non-ideal combustion processes.
- High octane number: (130) allows for increased efficiency due to a higher compression ratio.

While other characteristics present obstacles in the development of the hydrogen engine.

- Low minimum ignition energy: results in backfire and pre-ignition problems.
- Low energy density: significant volumes of hydrogen are necessary to provide comparable energy levels relative to current fuels.
- High flame temperature: results in higher wall heat losses.

With these advantages and disadvantages, along with others not listed here, engine developers have begun building and testing hydrogen-fueled engines in the hope to provide cleaner more efficient engines and possibly develop a hydrogen infrastructure for future technologies such as the fuel cell [2].

2.1.1 External Mixture Formation

Initial implementation of hydrogen fuel technologies included the usage of external mixture formation by either injecting hydrogen into an intake manifold or near the intake valve with port fuel injection [2,5]. Two major combustion problems occur

with these fuel control strategies. First, backfire or backflash occurs when the fresh charge is ignited before the intake valve is closed and results from the hydrogen mixing with hot residual gases that remain in the cylinder after combustion. Since the minimum ignition energy of hydrogen, 0.02 mJ, is relatively small (10% of normal gasoline), hydrogen shows a large propensity to backfire, especially when using manifold fuel injection at stoichiometric conditions. Port fuel injection can be properly timed so that a very rich, non-ignitable mixture is introduced to residual that has already been cooled by fresh intake air and thus reduces or eliminates backfire. The second combustion anomaly is pre-ignition and occurs when the new charge is ignited after the intake is closed but before the spark plug is fired. This occurs during compression and is a result of the hydrogen mixing with hot residual or contacting hot spots such as the spark plug or exhaust valves. It causes very large peak pressures and acoustic oscillations that can cause significant damage to the engine hardware. Again, pre-ignition is a result of the low ignition requirement of hydrogen. Pre-ignition is the main drawback of using port fuel injection because it reduces the maximum compression ratio and torque output of the engine. It has been reported that a port-injected hydrogen engine produces 35% less torque at low speeds and peak power is reduced by as much as 50% at high speeds relative to gasoline engines, mainly due to the inability to optimize engine parameters because of pre-ignition [4].

A problem with external mixture formation not directly related to combustion is that it causes an inherently low volumetric efficiency. The low density of hydrogen causes the intake hydrogen to consume 30% of the aspirated air volume. This causes a reduction in the maximum mean effective pressure and energy density inside the engine,

reducing power output. The only option is to increase the intake pressure, but pre-ignition limits the possible amount of boosting [6].

2.1.2 Internal Mixture Formation

Internal mixture formation, or direct injection, can eliminate many of the combustion anomalies and breathing problems associated with external mixture formation strategies. This is accomplished by appropriately timing the injection event. Injecting the hydrogen after the intake valve has closed effectively eliminates the possibility of backfire. Also, the hot residual gases are more easily mixed with cool air with direct injection, reducing pre-ignition. At a stoichiometetric ratio, 30% more air can be delivered to the cylinder when hydrogen is injected after the intake valve is closed, resulting in much higher energy density capabilities and a better volumetric efficiency [6]. Parameters such as start of injection and injection duration also play an important role in performance and emissions and can be optimized with direct injection.

The injector performance is critical to the overall performance of a direct-injection hydrogen engine. It must be able to cover a wide range of flow rates under varying load conditions and also promote proper mixing between the injected hydrogen and air. The injector must provide small amounts of hydrogen at idling conditions, but also very large amounts in very small time periods at high loads and speeds [6]. These facts combined with the low density and low lubricity of hydrogen put a huge demand on the injector. Although, direct injection has been proven to be a better option than external mixture formation, current injector designs limit the engine to low to medium speeds [6].

2.3 Overview of Jets

2.3.1 Steady Jets

Jets are a canonical flow that have been widely studied, especially steady jets. Although the main concern with automotive injections is their transient behavior, steady jets provide a basis for understanding the structure and scaling of transient jets.

2.3.1.1 Structure

The basic structure of a steady jet includes a potential core that has not felt the effects of viscosity and, therefore, has a velocity equal to that at the nozzle exit. Next, the flow goes through a transitional development region, and then finally becomes fully developed. Figure 2.1 diagrams these regions of a steady circular jet [7].

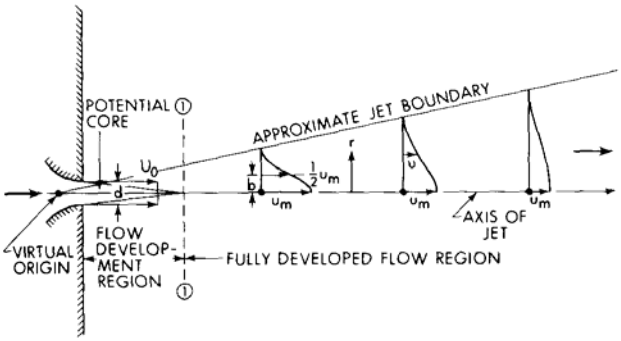

Figure 2.1. Definition sketch of circular turbulent jets [7].

In the fully developed region the flow becomes self-similar and the radial velocity profile, *U(r,z),* normalized by the centerline velocity, U_{CL}, is only a function of the nondimensional distance, $\eta = 2r / d_n$, where *r* is the radial position and d_n is the diameter of the nozzle exit. These relations are represented in equations (2.1) and (2.2).

$$\frac{U(r,z)}{U_{CL}} = f(\eta) \tag{2.1}$$

and $$\frac{U_{CL}}{u_n} = \frac{k_d}{(z/d_n)} \tag{2.2}$$

where z is the distance from the exit, u_n is the flow velocity at the nozzle exit, and k_d is a constant that has been experimentally been determined to be approximately 5.0 [8]. As seen in equation (2.2), the centerline velocity scales with the inverse of distance from the exit plane.

2.3.1.2 Exit Diameter Scaling Relations

An incompressible jet with a density different than that of the surrounding fluid still shows similarity characteristics and has been shown to behave like a jet of similar density as its surroundings when the nozzle diameter is replaced by the equivalent diameter given in equation (2.3) [8]:

$$d_{eq} = d_n \left(\frac{\rho_n}{\rho_{ch}} \right)^{1/2} \tag{2.3}$$

where ρ_n is the density of the injected fluid at the nozzle exit and ρ_{ch} is the density of the chamber fluid. For incompressible jets the nozzle exit density, ρ_n, is density of the injected fluid at the chamber pressure. Studies by Ricou and Spalding [9] and Birch et al. [10] have experimentally shown that the equivalent diameter modification properly correlates non-uniform density jet relations with uniform jet relations. An equivalent relation has been used with compressible jets ($M > 0.3$) to correct for both the effects of compressibility and also the differing densities between the injected and ambient fluids [8]. In this case ρ_n is the density of the injected fluid at the nozzle exit pressure, which differs from the chamber pressure due to compressibility effects. When the nozzle diameter, d_n, is replaced by its respective equivalent diameter in equation (2.2), the position of a fluid element as a function of time under incompressible or compressible

conditions can be determined by integration of the centerline velocity. These relations are shown in equations (2.4) and (2.5) [11,12]:

$$U_{CL} = \frac{dz}{dt} = k_d u_n \left(d_{eq}\right) \frac{1}{z} \tag{2.4}$$

$$z = \sqrt{2 k_d u_n \left(d_{eq}\right) t} \tag{2.5}$$

These relations provide a general scaling for the penetration of transient jets, shown in equation (2.6) [11,12].

$$z \propto \left(u_n d_{eq} t\right)^{1/2} \tag{2.6}$$

2.3.2 Incompressible Transient Jets

2.3.2.1 Structure

The structure and properties of incompressible transient jets or impulsively started jets have been studied for a wide range of applications. Turner (1962) [13] described the structure of plumes when studying atmospheric mixing in buoyant plumes. A plume was described as consisting of a spherical cap called a spherical head vortex that is supplied with additional buoyancy and momentum from a plume below. It was shown that the plume displays self-similarity characteristics throughout its evolution. Figure 2.2 illustrates this initial description of a jet or plume.

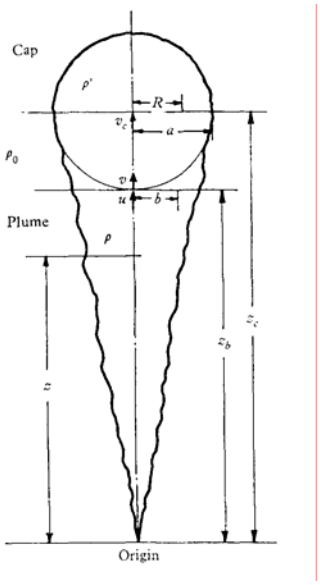

Figure 2.2. Turner's model of starting plume or jet [13].

2.3.2.2 Penetration Scaling Relations

Many subsequent authors have used Turner's plume model as the basic structure of a transient starting jet. Abramovich and Solan (1973) [14] used this model to develop analytical expressions for the velocity of the spherical vortex in the near and far fields of a liquid jet under laminar conditions with Reynolds numbers ranging from 80 to 500. It was found that the functional form for the velocity, inversely proportional to distance, of the spherical vortex was the same as the functional form for the axial velocity of a steady-state jet only with differing constants. The velocity of the spherical vortex was found to be approximately half that of a fluid element in a steady jet. Abramovich and Solan [14] showed that the half width and maximum axial velocity show similarity characteristics, both making the jet appear to start from a virtual origin different from the geometric origin. The virtual origin was found to be proportional to the exit diameter and the square root of the Reynolds number. A previous study by Sato and Sakao [15] also found that

an offset or virtual origin was needed to obtain agreement between experiment and theory with the origin moving downstream with increasing Reynolds number.

Witze (1980) [16] utilized features of Turner's structural model to develop differential equations involving the jet position, velocity, and the spherical vortex volume. The jet was approximated as a spherical vortex that is supplied with mass and momentum from a quasi-steady jet, but entrains no fluid itself. Characteristic time and length scales given by:

$$t^{+}_{n,\rho} = \frac{d_n}{u_n} \tag{2.7}$$

$$z^{+}_{n,\rho} = d_n \tag{2.8}$$

were developed for jets with the same density as the surrounding quiescent fluid, signified by the subscript ρ. The scales were found to properly collapse the penetration data taken of incompressible air jets that were injected into ambient air with Reynolds numbers ranging from 6,000 to 12,000. Penetration time was defined as the time it takes for the axial velocity to reach 70% of the steady state value for a specific location. Witze's data [16] showed a linear dependence between penetration and time at early times in the injection and a square root dependence at later times.

Lahbabi et al. (1993) [17] investigated incompressible jets by injecting ink into water to investigate starting jets with Reynolds numbers of 2,600. Their penetration data correlated well with the relations developed by Witze with a best fit given by:

$$\overline{z}_{n,\rho} = 2.1 + 2.9\sqrt{\overline{t}_{n,\rho}} \tag{2.9}$$

where

$$\overline{t}_{n,\rho} = \frac{t}{t^{+}_{n,\rho}} \tag{2.10}$$

and $$\overline{z}_{n,\rho} = \frac{Z_t}{z^+_{n,\rho}} \tag{2.11}$$

with Z_t being the jet tip penetration, and $\overline{t}_{n,\rho}$ and $\overline{z}_{n,\rho}$ are the nondimensional time and penetration for jets with the same density as the surrounding fluid.

Johari et al. (1997) [18] also studied impulsively started dyed water jets with Reynolds numbers ranging from 5000 to 20,000 using a Laser Induced Flourescence (LIF) flow visualization technique. The penetration data was normalized with the same time and length used by Witze for jets with the same density as the ambient medium. The results were presented in the following form:

$$\overline{z}_{n,\rho} = \alpha\left(\overline{t}_{n,\rho}\right)^{1/2} \tag{2.12}$$

where the jet tip penetration, Z_t, was corrected with the virtual origin, z_0, although virtual origin effects were assumed to be minimal. The proportionality constant, α, ranged from 2.14 to 2.58, with an average of 2.4. This value is compared to the value of 2.9 reported by Lahbabi et al. [17].

Joshi and Schreiber (2006) [19] also examined dyed water jets injected into a quiescent water tank with Reynolds numbers of 12,600. The penetration was normalized in the same manner used by Witze and other authors and the proportionality constant, α, was found to be approximately 3.0.

Abraham et al. (1994) [20] developed a similar relationship between penetration and time for an idealized incompressible jet with a differing density than the ambient surroundings using scaling arguments. The developed relationship is given by:

$$\frac{z}{d_n\left(\frac{\rho_n}{\rho_{ch}}\right)^{1/2}} \propto \left(\frac{tu_n}{d_n\left(\frac{\rho_n}{\rho_{ch}}\right)^{1/2}}\right)^{1/2} \tag{2.13}$$

This relationship gives rise to length and times scales given by:

$$z_n^+ = \left(\frac{\rho_n}{\rho_{ch}}\right)^{1/2} d_n = d_{eq} \tag{2.14}$$

$$t_n^+ = \left(\frac{\rho_n}{\rho_{ch}}\right)^{1/2} \frac{d_n}{u_n} = \frac{d_{eq}}{u_n} \tag{2.15}$$

Data from computer simulations of gaseous jets was found to approximately collapse to a single curve when these scales were utilized. The collapse was complete with respect to nozzle diameter, d_n, for all times, while the collapse was only approximate with $(\rho_n/\rho_{ch})^{1/2}$ at early times in the injection. This was attributed to differing virtual origins and incomplete jet development at early times.

Hill and Ouellette (1999) [21] reviewed the self-similar characteristics of transient turbulent jets and developed an analytical relationship for the penetration. They also employed the Turner model [13] to approximate the geometry of a gas jet. In their model the jet is constantly supplied with momentum through the orifice, and the momentum is, in turn, passed between the quasi-steady jet and the head vortex. The entrainment of the low momentum ambient fluid was assumed to follow the relationship reported by Ricou and Spalding [9]:

$$\frac{m}{m_0} = K_s \frac{z}{d_n} = K\left(\frac{\rho_{ch}}{\rho_n}\right)^{1/2} \frac{z}{d_n} \tag{2.16}$$

where m is the entrained mass, m_0 is the jet fluid mass, and the entrainment coefficient K = 0.32 [9]. The jet penetration was assumed, based on dimensional grounds, to follow the form:

$$Z_t = \Gamma \left(\frac{\dot{M}}{\rho_{ch}} \right)^{1/4} t^{1/2} \tag{2.17}$$

where $\dot{M}$ is the momentum flux through the orifice. The scaling constant Γ was found to be a function of K_s and s, the ratio of the head vortex diameter, D, to the jet tip penetration, Z_t through:

$$\Gamma^4 + \Gamma^2 K_s \left[\frac{(1-s)^2}{\sqrt{\pi}(2-s)s^3} \right] - \frac{24}{\pi(2-s)s^3} = 0 \tag{2.18}$$

The value for s was taken as 0.25 ± 0.05 from data of Rizk [22].

Although Hill and Oullette [21] approached the problem in a different manner than previous authors, the time scale, length scale, and functional dependence between the penetration and time associated with eq. (2.17) are equivalent to those developed by Abraham et al. (1994) [20]. By expanding the terms, eq. (2.17) takes on the following form:

$$\dot{M} = \rho_n u_n^2 A_n \tag{2.19}$$

$$\frac{Z_t}{d_{eq}} = \alpha \left(\frac{t u_n}{d_{eq}} \right)^{1/2} \tag{2.20}$$

$$\alpha = \Gamma \left(\frac{\pi}{4} \right)^{1/4} \tag{2.21}$$

Hill and Ouellette [23] investigated jets with downstream (beyond the near-nozzle region where a Mach disc can form and expansion waves are present) density ratios (injection to

ambient) of approximately 1.0, which corresponds to $K_s \sim 0.32$. For this K_s value, Γ was found from eq. (2.18) to be 3.0. The jet data shown by Hill and Ouellette [23] were also found to agree with this value.

Abraham (1996) [11] derived an expression for a transient gas jet by integrating the centerline velocity of a steady turbulent jet, as was introduced in the steady state jet portion of this chapter. The steady centerline velocity relationship used was that of Schlichting [24];

$$U_{CL} = \frac{3 d_{eq} u_n}{16 \pi^{1/2} C_t z} \tag{2.22}$$

where C_t is a parameter that relates the turbulent diffusivity to the kinematic momentum flux. By defining the tip position as the location where the velocity is a fraction, C_f, of the steady centerline velocity, the following expression for the location of the jet tip as a function of time was developed.

$$\left(\frac{Z_t}{d_{eq}} \right)^2 = \left(\frac{3 C_f}{8 \pi^{1/2} C_t} \right) \frac{t}{d_{eq} / u_n} \tag{2.23}$$

The entrainment constant, K, of eq. (2.16) can be related to the constant C_t by

$$K = 16 \pi^{1/2} C_t \tag{2.24}$$

Many values have been proposed for the constants C_t and K [11] for the fully developed region, and the value varies from 0.26 to 0.142 and, therefore, is only known within a factor of two.

The expression for jet tip penetration reported by Abraham [11] is equivalent to the relation developed by Hill and Ouellette [21] where Γ can be expressed as:

$$\Gamma = \left(\frac{3C_f}{4\pi C_t} \right)^{1/2} \tag{2.25}$$

A Γ value of 3.0 and a C_t of 0.0113, which corresponds to a K value of 0.32, results in a C_f value of 0.142. The other reported entrainment values result in Γ varying between 2.11 and 3.6 for the same value of C_f.

In summary, the previously mentioned authors [11-23] all use the same scaling relations with respect to penetration and time. The basic form is given by:

$$\frac{z - z_0}{d_{eq}} = \alpha \left(\frac{t u_n}{d_{eq}} \right)^{1/2} \tag{2.26}$$

where d_{eq} is replaced with d_n for jets of uniform density and $d_{eq} = d_n \left(\rho_n / \rho_{ch} \right)^{1/2}$ for jets with non-uniform density. The main discrepancies arise in the reported values of the proportionality constant, α. Table 2.2 shows the values of α from some of the authors.

Table 2.2. Values of α.

Author(s)	Slope (α)
Hill and Oullete [21]	2.82
Johari [18]	2.14 - 2.58
Lahbabi [17]	2.9
Abraham (1994) [20]	2.5
Joshi and Schreiber [19]	3.0

Naber and Siebers [25] studied the effects of ambient gas density on the penetration and dispersion of diesel sprays and developed nondimensional parameters that included the effects of dispersion or spray angle. Their data showed that as the ambient gas density is increased the spray angle also increases. The increased spray angle is a result of additional entrainment of ambient fluid mass. The relation between

entrained mass, m_0, the ambient density, ρ_{ch}, and spray angle, θ, is given in equation (2.27).

$$m_0 \propto \rho_{ch} d_n u_n \tan(\theta/2) \tag{2.27}$$

where θ is the spray angle. The characteristic time and length scales that were developed and associated parameters are given in eqs. (2.28) to (2.32) and were shown to fully collapse the data better than scaling mentioned for incompressible jets.

$$z^+_{n,\theta} = \frac{d_f \sqrt{\tilde{p}}}{a \tan\left(\theta/2\right)} \tag{2.28}$$

$$t^+_{n,\theta} = \frac{d_f \sqrt{\tilde{\rho}}}{a \tan\left(\theta/2\right) u_f} \tag{2.29}$$

$$\tilde{\rho} = \frac{\rho_n}{\rho_{ch}} \tag{2.30}$$

$$d_f = \sqrt{C_a} d_n \tag{2.31}$$

$$u_f = C_v \sqrt{2 \frac{\left(P_n - P_{ch}\right)}{\rho_n}} \tag{2.32}$$

where a is a constant with the value of 0.66 that relates to the tangent of the measured angle θ to the tangent of the spray dispersion angle used to develop a penetration correlation, C_a is the area contraction coefficient of the orifice, C_v is the orifice velocity coefficient and the subscripts *ch* and *f* pertain to chamber and fuel conditions respectively. A penetration correlation was developed using an integral control volume approach [25] and is given in eq.(2.33). This relation was also noted to be applicable to isothermal incompressible gas jets.

$$\overline{t}_{n,\theta} = \frac{\overline{z}_{n,\theta}}{2} + \frac{\overline{z}_{n,\theta}}{4}\sqrt{1+16\overline{z}_{n,\theta}^2} + \frac{1}{16}\ln\left(4\overline{z}_{n,\theta} + \sqrt{1+16\overline{z}_{n,\theta}^2}\right) \tag{2.33}$$

with $\overline{z}_{n,\theta}$ being the nondimensional penetration and $\overline{t}_{n,\theta}$ the nondimensional time. Their penetration data correlate well with this relation and collapse within ±10% with the application of the proposed scales. The scatter was attributed to the turbulent nature of the spray. As in eq.(2.33), the nondimensional penetration was shown to vary linearly with nondimensional time at early times (up to approximately $\overline{t}_{n,\theta} = 0.5$) and with the square root of nondimensional time at later times (after $\overline{t}_{n,\theta} = 10$), similar to jets. It should also be mentioned that the authors noted that as ambient density is increased sprays act more like incompressible jets with a density ratio of 1.0. They also briefly investigated hydrogen jets and found for an ambient to fuel density ratio of 0.7 the jet half angle had a value of 13 degrees.

2.3.3 Compressible Starting Jets

The main focus of this research is on compressible, underexpanded jets. When the pressure ratio between the outlet and inlet of an orifice or nozzle is sufficiently dropped to cause the pressure at the exit to be higher than the ambient surroundings, the complex flow that results is termed an underexpanded jet [12]. At the nozzle exit the flow is choked and expands upon leaving the nozzle. A complex pattern of expansion waves result at the outer rim of the exit as shown in Fig. 2.3. The expansion waves reflect from the free boundary of the jet and become compression shocks that form a barrel shaped structure that is terminated by a normal shock also called the Mach disk [12]. The Mach disk forms if the nozzle exit to chamber pressure ratio is above 2.1 [27].

Flow immediately after the Mach disk is subsonic, but these barrel shock structures can be repeated several times diminishing in strength due to viscous effects.

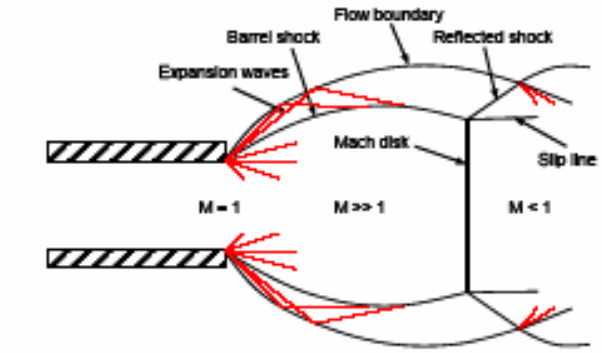

Figure 2.3. Structure of an underexpanded jet [26].

For moderately underexpanded flows with a nozzle to chamber pressure ratio below 2.1, a Mach disk does not form and instead the barrel shock is able to intersect at the flow axis [27,28].

An underexpanded jet is characterized by having an exit pressure higher than the ambient surroundings. The pressure, temperature, and density at the nozzle exit, assuming isentropic flow, are given in equations (2.34) through (2.36) [12]:

$$P_n = P_0\left(\frac{2}{\gamma+1}\right)^{\gamma/(\gamma-1)} \tag{2.34}$$

$$T_n = T_0\frac{2}{\gamma+1} \tag{2.35}$$

$$\rho_n = \rho_0\left(\frac{2}{\gamma+1}\right)^{1/(\gamma-1)} \tag{2.36}$$

where γ is the ratio of specific heats, the subscript n denotes nozzle exit conditions and 0 denotes stagnation conditions.

Ewan and Moodie (1986) [29] reviewed models of the velocity profile and velocity decay of underexpanded jets. They modeled an underexpanded jet as a fully expanded jet with a larger diameter at a point downstream from the nozzle exit that had the same mass flow rate as the original underexpanded jet. The diameter of the fully expanded jet is given by a manipulation of the continuity equation and by assuming that the flow is isothermal and no mixing occurs between the nozzle exit and Mach disk, and is shown in equations (2.37) and (2.38).

$$\rho_n A_n u_n = \rho_{ch} A_{eq} u_n \tag{2.37}$$

$$d_{eq} = d_n \left(\frac{\rho_n}{\rho_{ch}} \right)^{1/2} \tag{2.38}$$

These relations are equivalent to those suggested in eq. (2.3) to correct for nonuniform density and compressibility effects. The equivalent diameter scaling allowed Kleinstein's [30] formulation for velocity decay along the centerline of a fully expanded jet along with Warren's [31] modification to the compressible eddy viscosity to provide good agreement with Ewan and Moodie's data [29]. A modification to the length scale was also needed and is given by z^* in equation (2.39):

$$z^* = z - 2l_{barrel} \tag{2.39}$$

where l_{barrel} is the length of initial barrel shock and z* is the corrected distance from the jet origin. This correction is supported by Eggins and Jackson's [32] data that shows the velocity equilibrates two barrels lengths downstream of the nozzle exit. Ewan and Moodie [29] also provided a correlation between the barrel length, l_{barrel}, exit diameter, d_n, and the nozzle exit to ambient pressure ratio, N, given in equation (2.40).

$$l_{barrel} = 0.77 d_n + 0.068 d_n^{1.35} N \tag{2.40}$$

In summary, Ewan and Moodie [29] approximated an underexpanded jet as a fully expanded jet with a Mach number of unity with an equivalent mass flow rate at a distance of two barrel lengths downstream of the nozzle exit.

Hill and Ouellette (1999) [21] applied the scaling of eq. (2.17) to underexpanded methane jet data acquired by Miyake *et al*. [33], Chepakovich [34], and Hill and Ouellette [21]. The scaling constant Γ was found to remain approximately 3.0 for higher values of ρ_n/ρ_{ch} (≈1-2), but slightly decreased at a ρ_n/ρ_{ch} of 0.63. For the underexpanded cases the exit momentum flow was reduced by 10 percent from choked conditions to accommodate for the frictional effects inside the nozzle. Hill and Oulette (1999) [21] also developed a CFD model to approximate an underexpanded jet as a perfectly expanded jet with an enlarged initial diameter to match the mass flow rate. It was also noted that by assuming the flow is isothermal near the nozzle exit, the momentum flux is conserved between the two jets. Their simulation showed fair agreement with data collected by Witze [16], especially at later times in the injection.

Ra et al. (2005) [12] also did numerical simulations of transient underexpanded jets. They first approximated properties of the underexpanded jet in the same manner, a larger sonic jet with the same mass flow at the location of the Mach disk. The flow was further approximated by integrating the centerline velocity equation of an incompressible jet given by Schlichting [24] to produce inflow boundary conditions for the simulation, reducing the massive change in length scales. This method was found to produce good results when compared to experimental data and theoretical relations.

2.2 Schlieren Optical System

2.2.1 Basic Concepts

A schlieren optical system was used throughout this research to aid in imaging the jets produced by gaseous injectors. An example of a schlieren system is shown in Fig. 2.4.

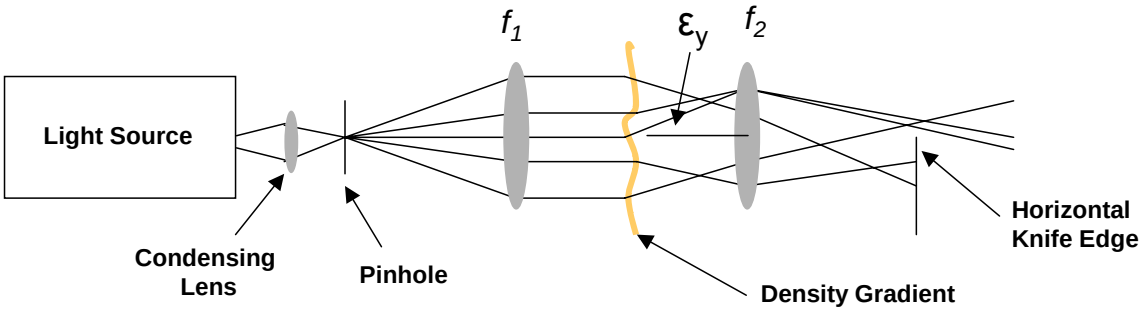

Figure 2.4. Schlieren Optical System

A schlieren system works on the principle of index of refraction differences associated with gases of differing density [35]. Parallel light is produced and directed through a test section where the phenomenon of interest is placed. When a gradient in density is present in the test section, the parallel light is bent by an angle, ε, due to the differing indices of refraction associated with the density gradient. This angle, ε, is given by:

$$\varepsilon = \frac{L}{n_0}\frac{\partial n}{\partial y} \tag{2.41}$$

where L is the length of the schlieren object along the optical axis of the system, n is the local index of refraction, and n_0 is the refractive index of the surrounding medium. The light exiting the test section is then refocused by a lens or mirror. At the focus of this lens or mirror, a knife edge is placed to block portions of the remaining light. If the knife edge is oriented in a horizontal fashion, the knife blocks light that is bent downward by a

negative density gradient in the vertical direction. This causes a dark spot to appear on the screen or camera that is placed behind the knife edge. Light not blocked by the knife edge shows up as a relatively bright spot on the image. Together, the light and dark areas create contrast and result in a clear representation of the expelled gas that would be otherwise invisible to the naked eye.

2.2.2 Sensitivity

The sensitivity and contrast produced by the schlieren system are important performance parameters. Contrast is the ratio of the change in illuminance, ΔE, at a point in the image and the general background illuminance, E, and is also given by [35]:

$$C \equiv \frac{\Delta E}{E} = \frac{f_2 \varepsilon}{a_c} \tag{2.42}$$

where f_2 is the focal length of the second lens or mirror and a_c is the length of the source image that is not cutoff by the knife edge. The contrast sensitivity, S, is the rate of change of image contrast with respect to refraction angle and is given by:

$$S = \frac{dC}{d\varepsilon} = \frac{f_2}{a_c} \tag{2.43}$$

A high value of sensitivity allows for small refraction angles and, hence, small density gradients to be imaged. As seen in eq. (2.43), sensitivity can be increased by using large focal length lenses or mirrors and a large amount of cutoff by the knife-edge. It should be noted that while using a large amount of cutoff increases sensitivity, it also reduces the brightness of the signal received by the photo-detection equipment. The sensitivity of a system should be optimized with respect to the availability of equipment [35].

2.2.3 Light Source Selection

The selection of the light source is also important to the performance of a schlieren optical system. The two major characteristics of a good light source are incoherent light and an appreciable source size. An automotive headlight is an example that has previously been used with good results in other schlieren systems [35]. A laser has neither of the advantageous qualities and is not well suited for usage in schlieren systems. First, the speckle pattern resulting from the coherent nature of a laser beam causes the resultant image to be distorted with a speckle pattern overlaying the phenomenon of interest. Secondly, the extent of a laser beam is relatively small, approaching a point source. When the beam is refocused at the knife edge it appears as a very small circle and adjusting the amount of cutoff is difficult. Essentially, the laser setup is an "on" or "off" system, either the entire light source is unblocked by the knife-edge or is completely blocked.

2.2.4 Knife Edge Orientation

The direction of the density gradients imaged by the system is determined by the orientation of the knife edge. When the knife edge is orientated in a horizontal fashion, vertical density gradients are imaged. Light that passes through the test chamber and is bent downward by vertical density gradients are blocked by the knife edge, while the light affected by horizontal density gradients are unaffected by the knife-edge. Likewise, a vertical knife edge interacts with density gradients in the horizontal direction and the image shows more contrast and detail in the horizontal direction.

3.0 Experimental Overview

3.1 Experimental Apparatus

3.1.1 Injectors

Four prototype injectors developed by Westport Innovations were used to produce transient gaseous jets at a wide range of conditions including high pressures (≥ 100 bar). The four injectors are identical except for the number of holes and hole arrangement on each injector's tip. The injectors have three, seven, nine, or thirteen holes, each having a total orifice area of 1.5 mm^2. Figure 3.1 displays a diagram of a typical injector tip explaining the injector tip hole spacing parameters. The three-hole injector has three 0.80 mm diameter holes radially spaced 120 degrees apart with the axis of each hole 45 degrees from the injector axis. The seven-hole injector has one central on-axis hole surrounded by a ring of six holes radially spaced 60 degrees apart that are orientated 30 degrees from the axis of the injector. Each of these holes has a diameter of 0.52 mm. The nine-hole injector has two rings of 0.46 mm diameter holes. The inner ring has three holes spaced 120 degrees radially and orientated 30 degrees off-axis and the outer ring has six holes spaced 60 degrees radially and 50 degrees off-axis. The rings are rotated relative to each other so that no two holes are on the same radius of the injector tip. The thirteen-hole injector has one central hole and two rings with six holes radially spaced 60 degrees apart. The holes in both rings are orientated 30 degrees from the injector axis and are also staggered such that no two holes are on the same radius. All of the holes in the thirteen-hole injector tip have a diameter of 0.38 mm. Figure 3.2 displays schematics of the hole layout of each injector tip.

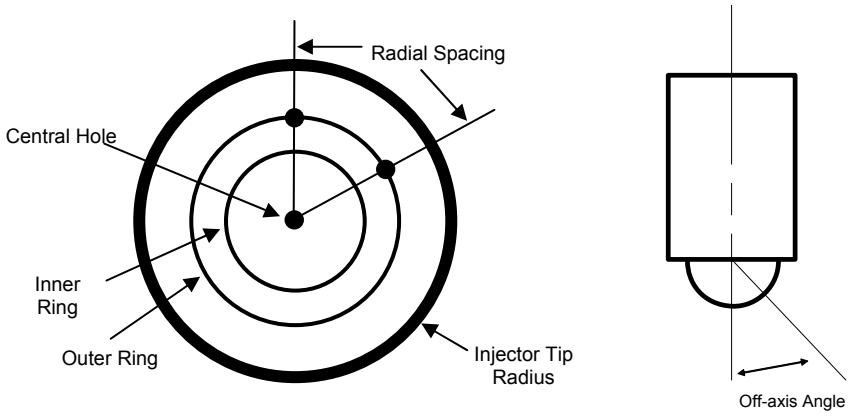

Figure 3.1. Diagram of injector tip with relevant parameters.

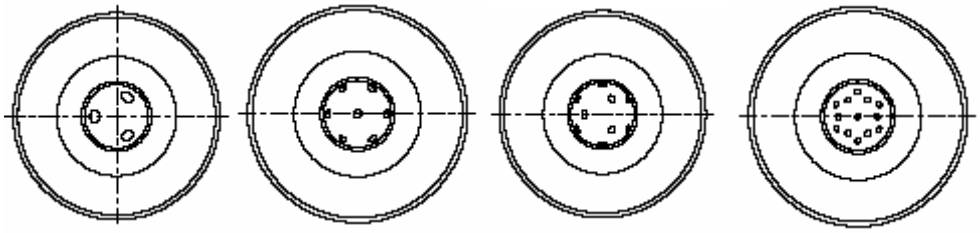

Figure 3.2. Schematic for hole arrangements in the **a)** three-hole **b)** seven-hole **c)** nine-hole and **d)** 13-hole injectors.

3.1.2 Optical Test Chamber

An optical vessel was developed to provide a quiescent, pressurized environment for various flows to propagate into. The chamber consists of a 245 mm long, 152 mm inner diameter flanged steel pipe with a thickness of 6.35 mm. The pipe is capped at each end by 24.8 mm thick steel plates. Each end plate has a 88.9 mm diameter 12.7 mm thick quartz window either centered or offset 27.2 mm. The offset window configuration allows for optical access throughout the chamber through rotation of the end plates. Three pipe-threaded holes were placed in the side of the vessel for gas delivery and discharge and also electrical power access. The total volume inside the test chamber is approximately 5500 mm^3. A 39.5 mm hole in the top of the vessels allows the injectors to

be mounted vertically in a separate aluminum holding piece that is fastened to the top of the vessel. The complete chamber and individual end plates are shown in Figs. 3.3 and 3.4.

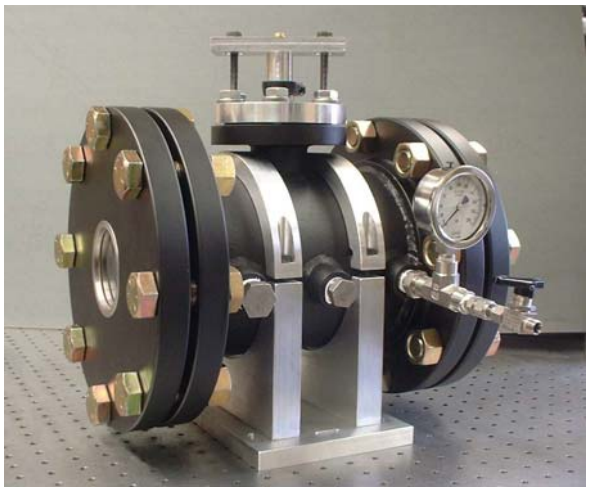

Figure 3.3. Optical pressure vessel.

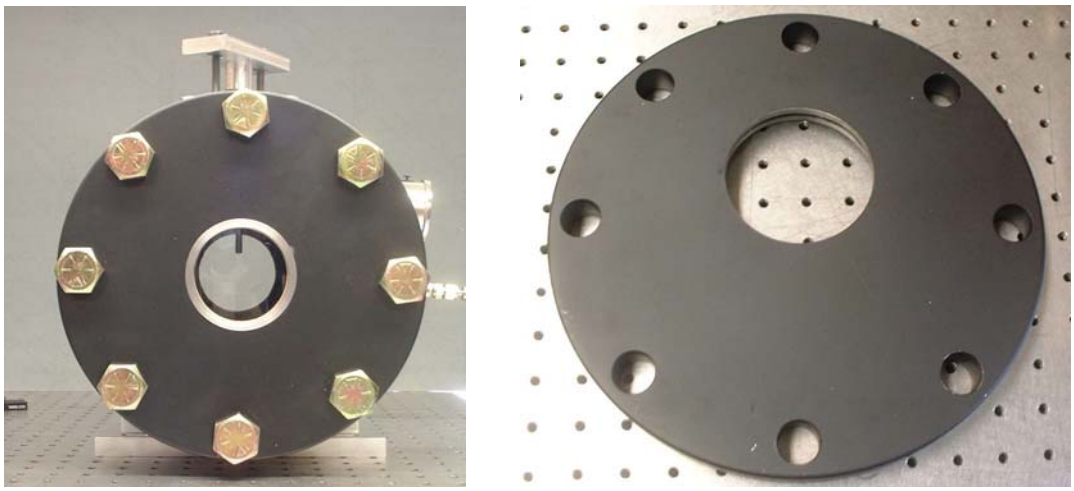

Figure 3.4. Centered and offset end plates.

3.1.3 Schlieren Optical Systems

3.1.3.1 Z-type Schlieren System

The Z-type schlieren system used to visualize the gaseous jets is shown in Fig. 3.5. An *f*/1.4 condenser lens imaged the light source onto a 1 mm pinhole to create a well defined source. Light from the pinhole was collimated by a 1140 mm focal length *f*/10.5 parabolic mirror before passing through the test section. A matching parabolic mirror then produced an image of the source onto an adjustable knife edge, which was oriented so as to enhance the contrast of the jet leading edge.

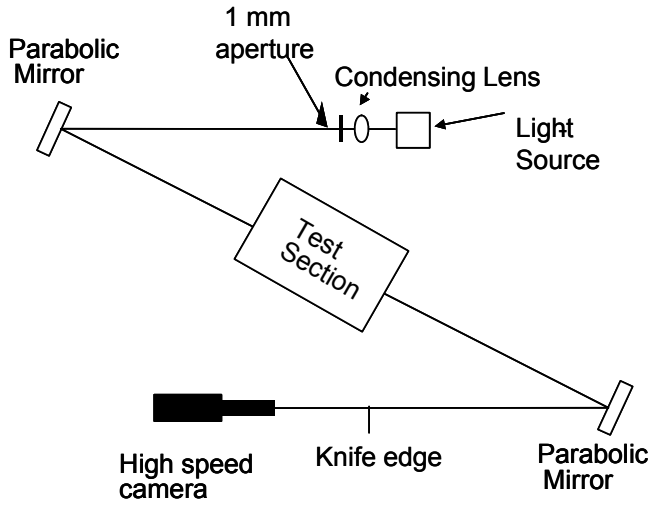

Figure 3.5. Z-type schlieren system.

3.1.3.2 Double-pass Schlieren System

A double pass schlieren system was used to image the jet patterns "end-on", or directly towards the tip of the injector. The injector was mounted horizontally in the back wall of the test chamber through a circular mirror with a hole to accommodate the injector tip. This mirror reflected the parallel light back through the test section, out the

initial window and back towards the parabolic mirror. This system is shown in figure 3.6.

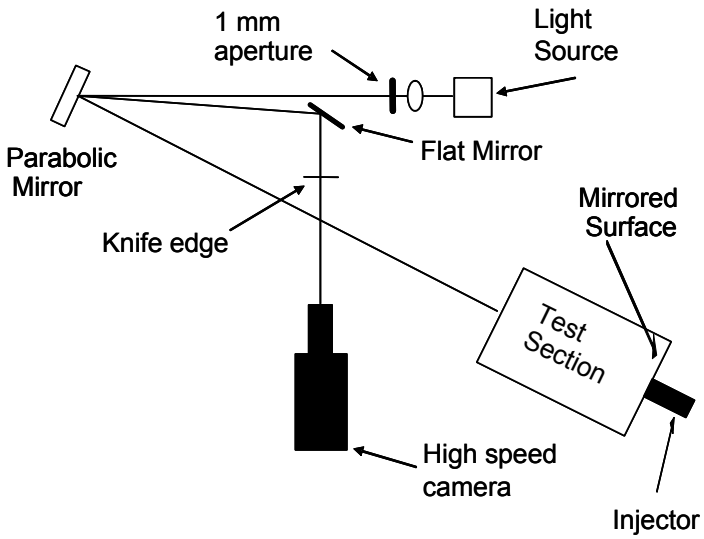

Figure 3.6. Double pass schlieren system.

The reflected light was slightly misaligned so that a small flat mirror could be used to redirect the light away from the original light source. The knife edge and camera were the same as in the z-type system. Since the light passes through the test section twice and is, therefore, deflected by the density gradients twice, the sensitivity of this type of system is naturally greater than that of a z-type system.

3.1.3.3 Aberrations

Two types of optical aberrations are associated with the z-type and double pass schlieren systems. The first being coma, which arises when the direction of reflected light depends on the position of the point of reflection. This happens by using the parabolic mirrors at a tilted angle and causes a point source to be focused as a line. The aberration becomes larger when the parabolic mirrors are tilted at more severe angles. An attractive feature of the z-type system is that coma is cancelled out by arranging the

second or refocusing mirror at an equivalent angle as the first mirror. A z-type system is therefore absent of any coma. Coma cannot be eliminated from a double pass system and some blurring or 'ghosting' will always be present. The second aberration is called astigmatism and also causes the system to fail at focusing light to a single point. Instead, the light is focused to two lines that are perpendicular to each other and also becomes worse with larger values of mirror tilt angle. Astigmatism is not corrected by a second parabolic mirror, as is the case for coma aberrations. To minimize the effect of astigmatism, the mirror tilt angles were kept to a minimum, approximately 12 degrees for both systems.

3.1.4 Rate Shape Test Chamber

To measure the discharge coefficient and mass flow rate as a function of time for each injector a spherical test chamber with access for a thermocouple, an Omegdyne model PX61C1-100AV absolute pressure transducer, and a 7061 Kistler piezoelectric relative pressure transducer was developed. The chamber is spherical with a diameter of 101.6 mm and is 2.56 mm thick. The top of the sphere is flat to accommodate for connection to a flat aluminum piece that holds the injector. The two pieces are clamped together using six 1/4 inch steel bolts and sealed by a static o-ring face seal. Figure 3.7 displays the rate shape test chamber setup.

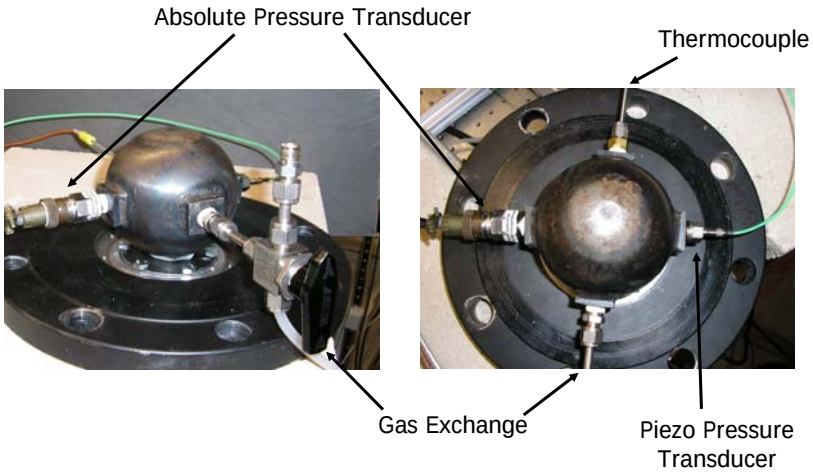

Figure 3.7. Rate shape test chamber setup.

3.2 Experimental Methods

3.2.1 Image Processing

Jet visualization was the main experimental focus of this study and was used to investigate the flow structures of gaseous jets produced by the prototype injectors. The previously mentioned schlieren systems were used to image the gaseous jets under a wide range of conditions and several image processing techniques were used to measure the jet tip penetration and jet angle as functions of time. Jet patterns were imaged both vertically and end-on or directly towards the tip of the injector.

The original images taken of each injection event were 8-bit black and white images. A simple image processing algorithm was used to improve the contrast of the original images and remove static imperfections in or on the optical equipment. The algorithm that was used is shown in eq.(3.1). Each pixel in the original image is divided by the corresponding pixel in a background reference image taken prior to each injection process. This quotient is then reduced by one and multiplied by a constant, S_c. Finally a median value of 128 is added to create the pixel intensity of the new corrected image. If the corresponding pixels in the original and background reference images are equivalent,

the intensity in the new image is 128. This causes anything that does not change relative to the background reference to have a gray color (pixel intensity =128) and any transient object such as a gaseous jet to have much greater contrast.

$$\left(\frac{\text{Image}}{\text{Background Reference}} - 1\right) S_c + 128 = \text{New Image} \tag{3.1}$$

3.2.2 Penetration Measurements

The jet tip penetration was measured using two different techniques depending on the interaction and overlap between the individual jets in the flow pattern. The first technique was utilized with jet patterns where some overlap was observed between jets and individual jets could not be isolated. The pixel intensity was measured along the centerline of an individual jet, or in cases where several jets coalesce, the centerline of a group of jets. The vertical penetration was then defined as the location where the centerline intensity fell below a certain value, starting from the bottom of an image. Figure 3.8 further illustrates this technique.

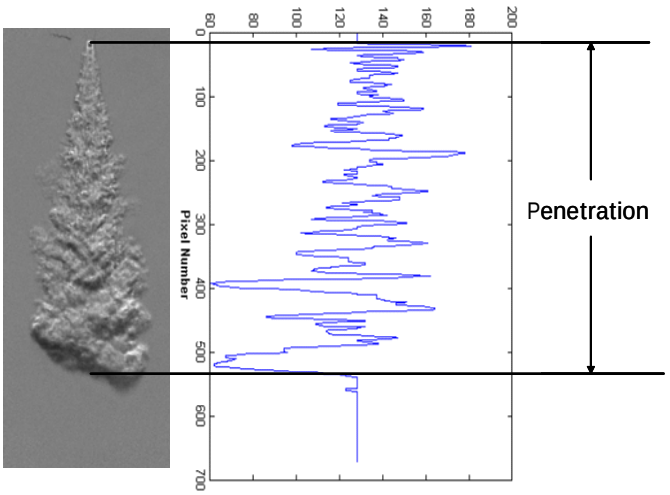

Figure 3.8. Description of penetration measurement, plot shows pixel intensity (upper horizontal axis) along centerline of center jet.

Since a majority of the jets are not aligned with the axis of the injector and thus not parallel to the image plane, a trigonometric correction factor was necessary to convert the measured vertical penetration to the total penetration. This correction method is shown in Fig. 3.9, which also illustrates how this technique introduces some inherent error to the total penetration measurement. Due to the rounded geometry of the jet head the vertical measurement and trigonometric correction overpredicts the actual penetration of an individual jet.

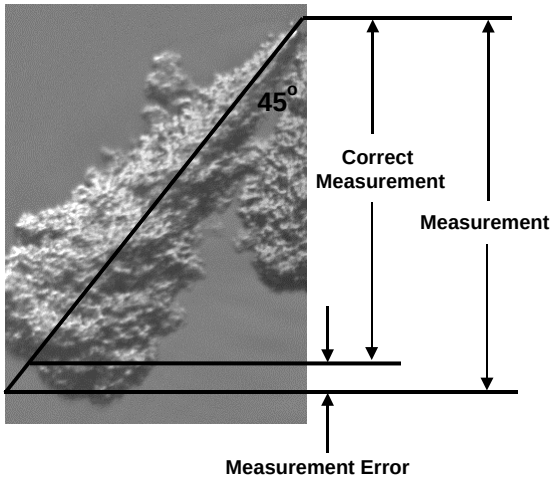

Figure 3.9. Measurement error associated with the projection of the head vortex.

The second method of measuring the penetration was used with jet patterns where an individual jet could be isolated. It involves an iterative procedure developed by Naber and Siebers [25] and includes determination of the angle, θ, of the quasi-steady jet region that excludes the head vortex. The jet angle, θ, is calculated by measuring the projected area, $A_{p,Z/2}$, contained within the jet up to half of its penetration, $Z_t/2$, and approximating the jet as a triangle in this initial region before the head vortex. The relation for calculating θ is illustrated in Fig. 3.10 and is given in eq. (3.2).

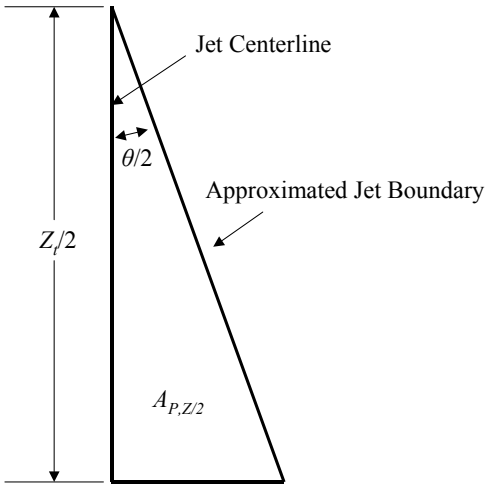

Figure 3.10. Approximated jet geometry for determination of jet angle, θ [25].

$$\frac{\theta}{2} = \tan^{-1}\left(\frac{A_{P,Z/2}}{\left(Z_t/2\right)^2}\right) \tag{3.2}$$

This relation could not be used here due to schlieren effects near the nozzle exit causing the area of the jet to be larger near the origin. A slight modification was made to eq. (3.2) to eliminate the near field portion of the jet from the calculation and is shown in Fig. 3.11 and equation (3.3).

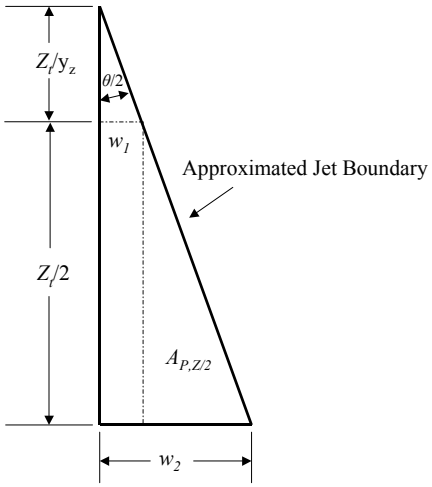

Figure 3.11. Modified area relation for determination of the jet angle θ.

$$\frac{\theta}{2} = \tan^{-1}\left(\frac{1}{1+4y_z}\frac{A_{P,Z/2}}{(Z/2)^2}\right) \tag{3.3}$$

where y_z determines the initial portion of the jet that is eliminated from the jet angle calculation. A derivation of these jet angle relations is provided in Appendix A.1. The method, illustrated in Fig. 3.12, starts with a penetration, Z_1, greater than the length of the jet and works back towards the jet origin. The jet half area, $A_{p,Z/2}$, jet angle, θ, and the amount of an arc that is inside the jet are iteratively calculated at incremental penetration values. The arc is defined by a radius equal to half of the penetration, $Z_t/2$, with an included angle of $\theta/2$. The final penetration measurement, Z_f, is then defined as the length where half an arc with an angle of $\theta_f/2$ is inside the head vortex of the jet.

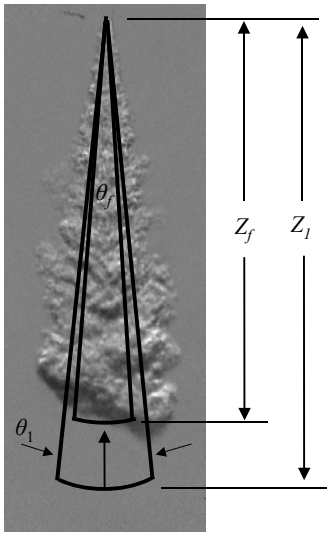

Figure 3.12. Illustration of iterative penetration measurement method.

In order to use this method the jet needed to be isolated from the background in each individual image. This was done using an edge detection function in Matlab to determine the outline of the jet. The result of the edge-detection algorithm is shown in Fig. 3.13.

Figure 3.13. Result of edge-detection on jet image.

A significant number of additional structures within the jet are identified by the edge-detection and were filled in from the right-most to the left-most of these structures as shown in Fig. 3.14.

Figure 3.14. Final result of jet isolation.

3.2.3 Rate Shape Determination

The rate shape or mass flow rate of each injector was measured using a simple thermodynamic model illustrated in Fig. 3.15. The rate shape was calculated by measuring the pressure in the rate shape chamber throughout the injection process and using the following relation;

$$\dot{m} = \frac{c_v V}{R\left(h_0\left(T_0\right) - u\left(T\right) + c_v T\right)} \frac{dp}{dt} \tag{3.4}$$

where $\dot{m}$ is the mass flow rate, V is the chamber volume, h_0 is the enthalpy of the gas in the chamber at the initial temperature, T_0, c_v is the specific heat at constant volume, u is the internal energy, and R is the ideal gas constant. This relation is a combination of continuity and the first law of thermodynamics. This process was also assumed to be adiabatic as noted in Fig. 3.15 and the gases were assumed to be ideal.

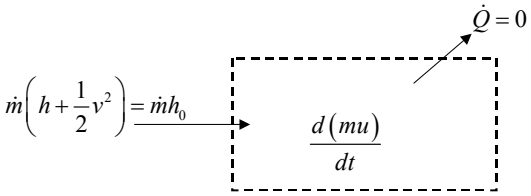

Figure 3.15. Thermodynamic model of injection process.

3.2.4 Discharge Coefficient

The discharge coefficient of each injector was measured to further characterize their performance and was determined by measuring the absolute pressure before and after an injection event. The injection length was increased and sufficient time was allowed for heat transfer to occur and the temperature to drop to its initial value. The ideal gas law was then used to calculate the amount of mass injected into the chamber. The mass injected into the chamber, Δm in a single injection is given by:

$$\Delta m = \frac{(P_2 - P_1)V}{RT} \tag{3.5}$$

where P_2 is the pressure after injection and P_1 is the initial pressure. The approximated average mass flow rate, $\dot{m}_{actual,ave}$ is then calculated by dividing the injected mass, Δm, by the injection duration, t_{inj}. The ideal average mass flow rate, $\dot{m}_{ideal}$ was calculated assuming the flow is choked at the nozzle exit and using the following relation;

$$\dot{m}_{ideal} = \rho^* u^* A_n \tag{3.6}$$

where A_n is the nozzle exit area, and ρ^* and u^* are the density and velocity at choked conditions, given by;

$$\rho^* = \rho_0 \left(\frac{2}{\gamma + 1} \right)^{\gamma/(\gamma - 1)} \tag{3.7}$$

$$u^* = \sqrt{\gamma R T^*} \tag{3.8}$$

where;

$$T^* = T_0 \left(\frac{2}{\gamma + 1} \right) \tag{3.9}$$

with the superscript * denoting choked conditions and the subscript *0* denoting stagnation conditions. The discharge coefficient is then given by:

$$C_D = \frac{\dot{m}_{actual,ave}}{\dot{m}_{ideal}} \tag{3.10}$$

3.3 Experimental Conditions

3.3.1 Vertical Imaging

3.3.1.1 Entire Jet Pattern

Initially, the jets produced by the prototype injectors were imaged vertically or normal to the injector axis. No attempt was made to isolate individual jets and, thus, the entire jet pattern was imaged for each injector. The experimental conditions for this arrangement were chosen to provide gaseous jets at both incompressible and compressible (including underexpanded) conditions. By sweeping from severely underexpanded conditions down to low Mach number flows, the effects of compressibility, underexpansion, and shock structures can be investigated relative to incompressible jets. The conditional parameters that were varied in this study were; injection pressure, injected gas, chamber density, and chamber gas. The injected gas was varied between hydrogen and helium to investigate the effects of differing injection gas properties including the ratio of specific heats, γ. Nitrogen was also injected into a nitrogen atmosphere to isolate the density field independent of the mixing processes. Nitrogen was primarily used as the chamber gas while carbon dioxide was also used in order to increase the density at the maximum chamber pressures.

The first conditions included a range of injection and chamber densities indicative of hydrogen engine cylinder conditions. The injection pressures and gases along with chamber pressures and gases for these conditions are shown in Table 3.1 with the injector indicated by the number of holes in the specific injectors nozzle tip. Table 3.2 displays the same conditions with corresponding injection and chamber densities.

Table 3.1. Stagnation injection pressure, injected gas, chamber pressure, and chamber gas used for injectors specified by the number of holes in injector's tip.

			Chamber Pressure [bar]				
			1	3.4	4.6	7.2	
			N_2	N_2	CO_2	CO_2	N_2
Injection Pressure [bar]	104	H_2	3,7,9,13	3,7,9,13	3,7	3,7,9,13	3,7,9,13
		He	3,7,9,13	3,7,9,13	7	3,7,9,13	3,7,9,13
	70	N_2	3,7,9,13	3,7,9,13			3,7,9,13
	52	H_2	3,7,9,13	3,7,9,13	3,7	3,7,9,13	3,7,9,13
		He	3,7,9,13	3,7,9,13	7	3,7,9,13	3,7,9,13
		N_2	3,7,9,13	3,7,9,13			3,7,9,13

Table 3.2. Stagnation injection density, injected gas, chamber density, and chamber gas used for injectors specified by the number of holes in injector's tip.

			Chamber Density [kg/m^3]				
			1.15	3.80	8.17	12.82	8.17
			N_2	N_2	CO_2	CO_2	N_2
Injection Density [kg/m^3]	8.50	H_2	3,7,9,13	3,7,9,13	3,7	3,7,9,13	3,7,9,13
	16.09	He	3,7,9,13	3,7,9,13	7	3,7,9,13	3,7,9,13
	79.10	N_2	3,7,9,13	3,7,9,13			3,7,9,13
	4.29	H_2	3,7,9,13	3,7,9,13	3,7	3,7,9,13	3,7,9,13
	8.32	He	3,7,9,13	3,7,9,13	7	3,7,9,13	3,7,9,13
	59.61	N_2	3,7,9,13	3,7,9,13			3,7,9,13

Additional conditions were imposed on the 3 and 7 hole injectors to further investigate the effects of compressibility and underexpansion under a wider, more complete range of pressures and densities. These additional conditions are displayed in table 3.3.

Table 3.3. Stagnation injection pressure, injected gas, chamber pressure, and chamber gas used for injectors specified by the number of holes in injector's tip.

			Chamber Pressure [psig]		
			1	3.4	7.2
			N_2	N_2	N_2
Injection Pressure [bar]	18.2	H_2	3,7	3,7	3,7
		He	3	3	3
	35.5	H_2	3,7	3,7	3,7
		He	3	3	3
	69.7	H_2	3,7	3,7	3,7
		He	3	3	3
	87.2	H_2	3	3	3
		He	3	3	3

3.3.1.2 Isolated Individual Jets

In order to use the iterative method of penetration measurement, individual jets needed to be imaged with very little interaction with other jets in the flow. This was accomplished by using a blocking plate with the seven-hole injector that only allowed the central on-axis jet to propagate into the imaging plane and also by orienting the three-hole injector such that a single jet was parallel with the imaging plane with the other two jets not overlapping it. The conditions used to produce these individual jets spanned from low Mach number (≈ 0.1), incompressible flows to highly underexpanded conditions. These conditions are shown in table 3.4.

Table 3.4. Stagnation injection pressure, injected gas, chamber pressure, and chamber gas used for specified injectors single jet experiments.

			Chamber Pressure [bar]	
			1	3.4
			N_2	N_2
Injection Pressure [bar]	1.3	H_2, He	3,7	
	1.5	H_2, He	3,7	
	1.9	H_2, He	3,7	
	2.1	H_2, He	3,7	
	2.4	H_2, He	3,7	
	2.7	H_2, He	3,7	
	3.2	H_2, He	3,7	
	3.5	H_2, He		3,7
	3.8	H_2, He		3,7
	3.8	H_2, He	3,7	

3.3.2 End-on Imaging

The double-pass schlieren system was utilized to view the jets looking axially towards the injector tip to obtain a more complete picture of the jet pattern produced by each injector. The conditions tested using the end-on imaging are shown in Table 3.5.

Table 3.5 Stagnation injection pressure, injected gas, chamber pressure, and chamber gas used for injectors specified by the number of holes in injector's tip.

			Chamber Pressure [bar]		
			1	3.4	7.2
			N_2	N_2	N_2
Injection Pressure [bar]	104	He	3,7,9,13	3,7,9,13	3,7,9,13
	52	He	3,7,9,13	3,7,9,13	3,7,9,13

3.3.3 Rate Shape and Discharge Coefficient

The rate shape for each injector was measured at a wide range of injection pressures with a constant injection duration of 3 ms. Helium was injected into a helium environment for all cases. The conditions tested included stagnation injection pressures of 18.2, 35.5, 52.0, 70.0, and 104 bar with a constant chamber density of 0.16 kg/m^3. The discharge coefficient was measured under these same injection pressures and chamber density.

4.0 Overview of Results

The results of this study include images of jets and the corresponding penetration rate measurements. The jet patterns of the four prototype injectors were imaged both normal to, and along the jet axis to provide a complete qualitative view of the injection process. In this chapter selected images and penetration data are presented to provide a basic understanding of the jet structure, with relevant phenomena highlighted. Chapter 5 provides a more comprehensive analysis of the remaining penetration data.

4.1 Jet Pattern Visualizations

4.1.1 Three-Hole Injector

Figures 4.1a)-d) display images of jet patterns produced by the three-hole injector with an injection pressure, P_0, of 104 bar and a chamber density, ρ_{ch}, of 3.8 kg/m^3. The injected medium is hydrogen and the quiescent chamber medium is nitrogen. The original and corrected images are shown to display the quality of the images produced by the schlieren system prior to, and after image enhancement. The side-view images were taken with a frame rate of 4,800 fps while the end-on images were taken with a frame rate of 8,200 fps. Each jet can clearly be seen in the side-view and the end-on images, which shows that the three individual jets do not come in contact and, therefore, do not directly interact with each other. The three-hole injector also showed irregularities between jets as in figure 4.1b, where the jet in the lower left corner is considerably shorter than the remaining jets. This jet irregularity could have an important impact on the overall combustion quality by creating uneven mixing throughout the cylinder and can be attributed to differences in the geometries of each hole in the injector tip.

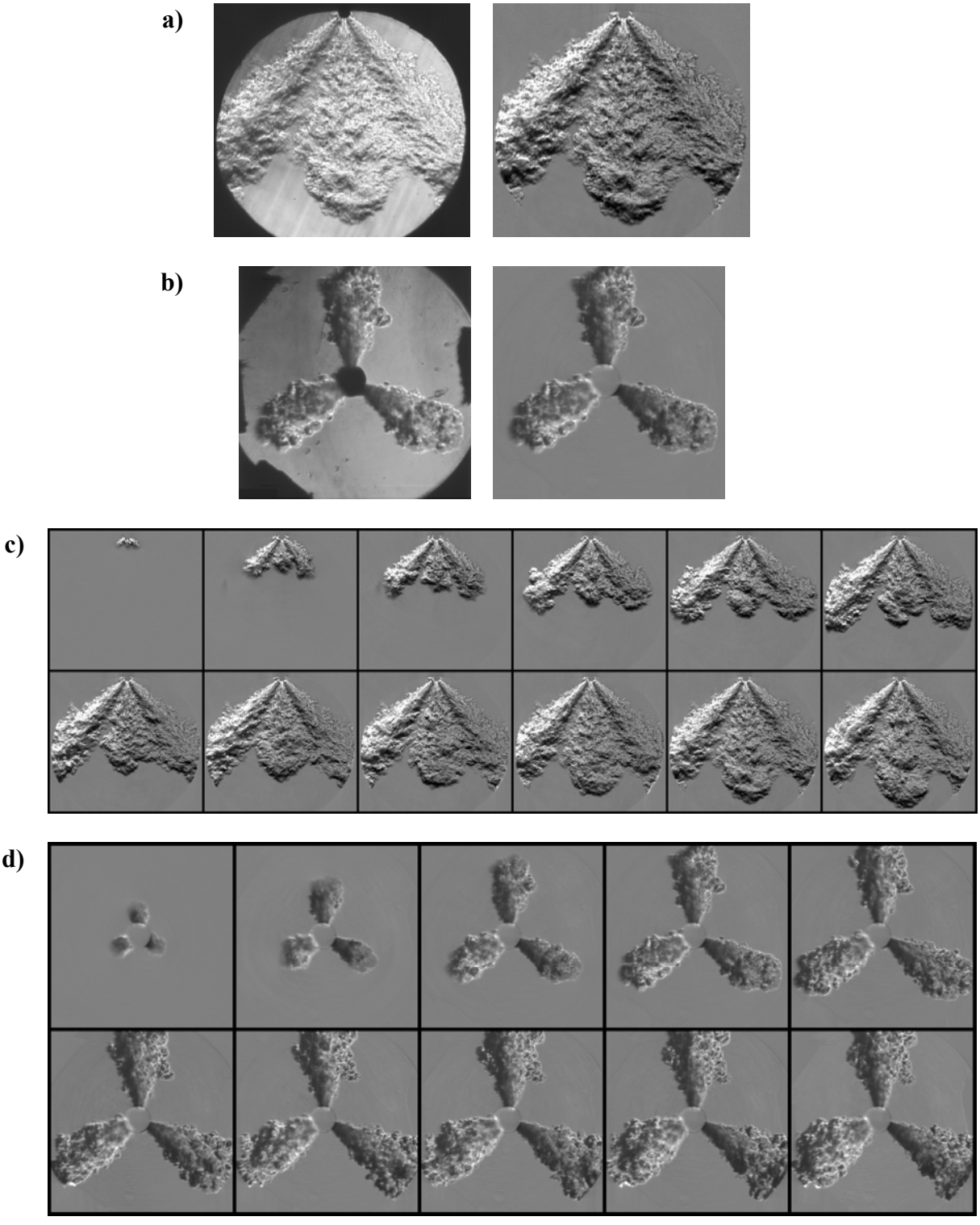

Figure 4.1. a) Original and corrected side-view images of jet pattern produced by the three-hole injector **b)** original and corrected end-on images **c)** time series of side-view images, Δt = 208 μsec **d)** time series of end-on images, Δt = 122- μsec, P_0 = 104 bar (hydrogen), ρ_{ch} = 3.4 kg/m ^{3} (nitrogen).

4.1.2 Seven-hole Injector

Figures 4.2a)-d) display images of hydrogen jet patterns produced by the seven-hole injector with an injection pressure, P_0, of 104 bar and an ambient nitrogen gas density, ρ_{ch}, of 3.8 kg/m^3. The side-view images were taken at a frame rate of 4800 fps and the end-on images at 8200 fps. The central jet and the surrounding ring of six jets can be seen in the side-view images with the end-on images showing only a small amount of interaction between the jets, confined to regions near the nozzle exit. The seven-hole injector also has a tendency to produce irregular jets. The upper right jet in Fig. 4.3b has a shorter penetration relative to the others throughout the entire injection.

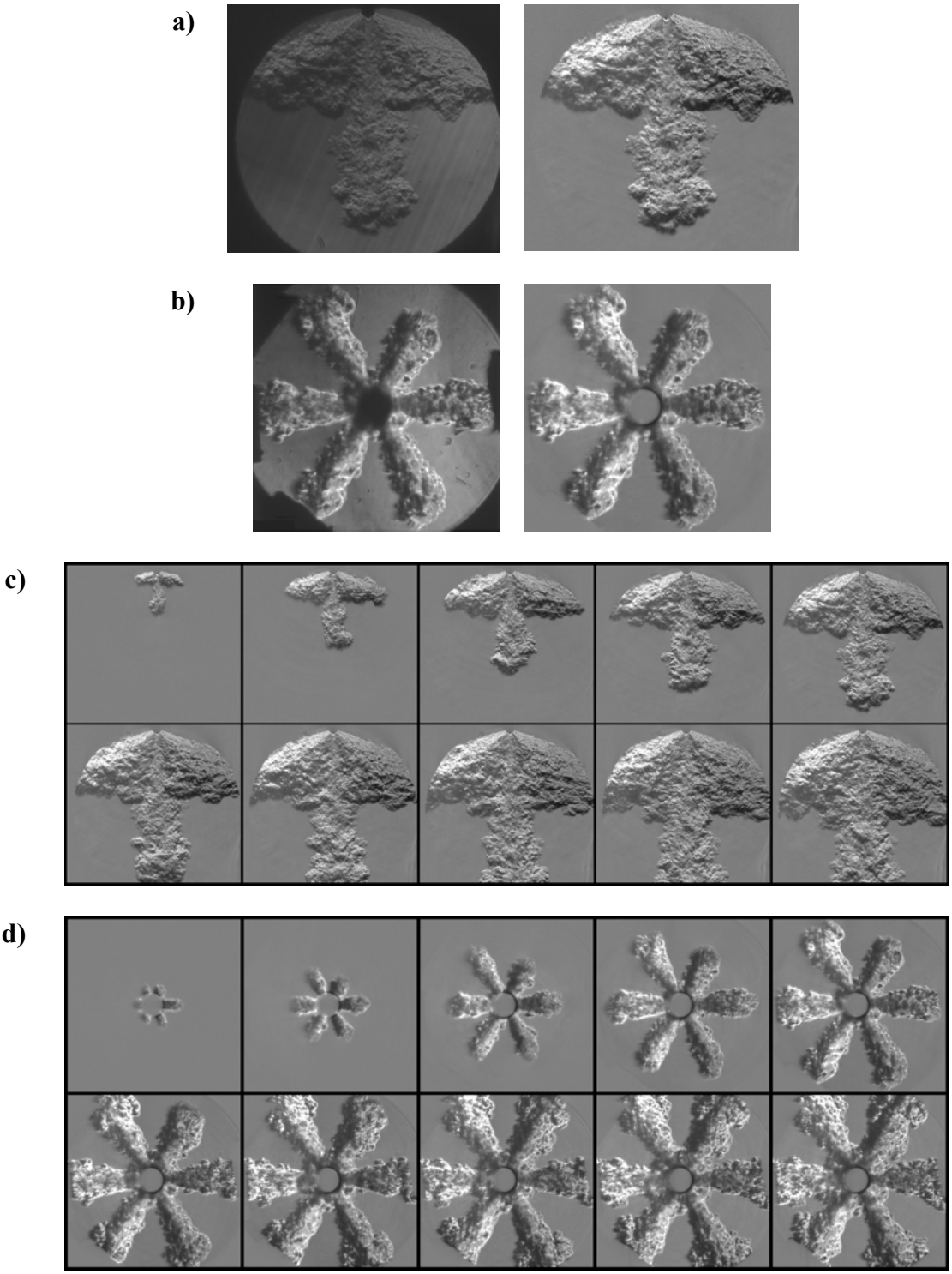

Figure 4.2. a) Original and corrected side-view images of jet pattern produced by the seven-hole injector **b)** original and corrected end-on images **c)** time series of side-view images, $\Delta t = 208$ μsec **d)** time series of end-on images, $\Delta t = 122$ μsec, $P_0 = 104$ bar (hydrogen), $\rho_{ch} = 3.4$ kg/m ^{3} (nitrogen).

4.1.3 Nine-hole Injector

Figures 4.3a)-d) display images of jet patterns produced by the nine-hole injector with an injection pressure, P_0, of 104 bar and a chamber pressure, ρ_{ch}, of 3.8 kg/m^3 with the same frame rates as the previous injectors. Distinction between individual jets is difficult in both the side-view and end-on image sets due extensive overlap and interaction of adjacent jets. The end-on images show that the three adjacent jets interact and essentially coalesce into three larger jets, concentrating the injected fuel into rich regions. This coalescence reduces the amount of ambient fluid that can be entrained into the jets and, thus, less mixing takes place. Note that even though the holes in the individual rings of the nine-hole injector's tip are radially spaced evenly, the orientation of the rings causes three sets of three holes to be more closely spaced.

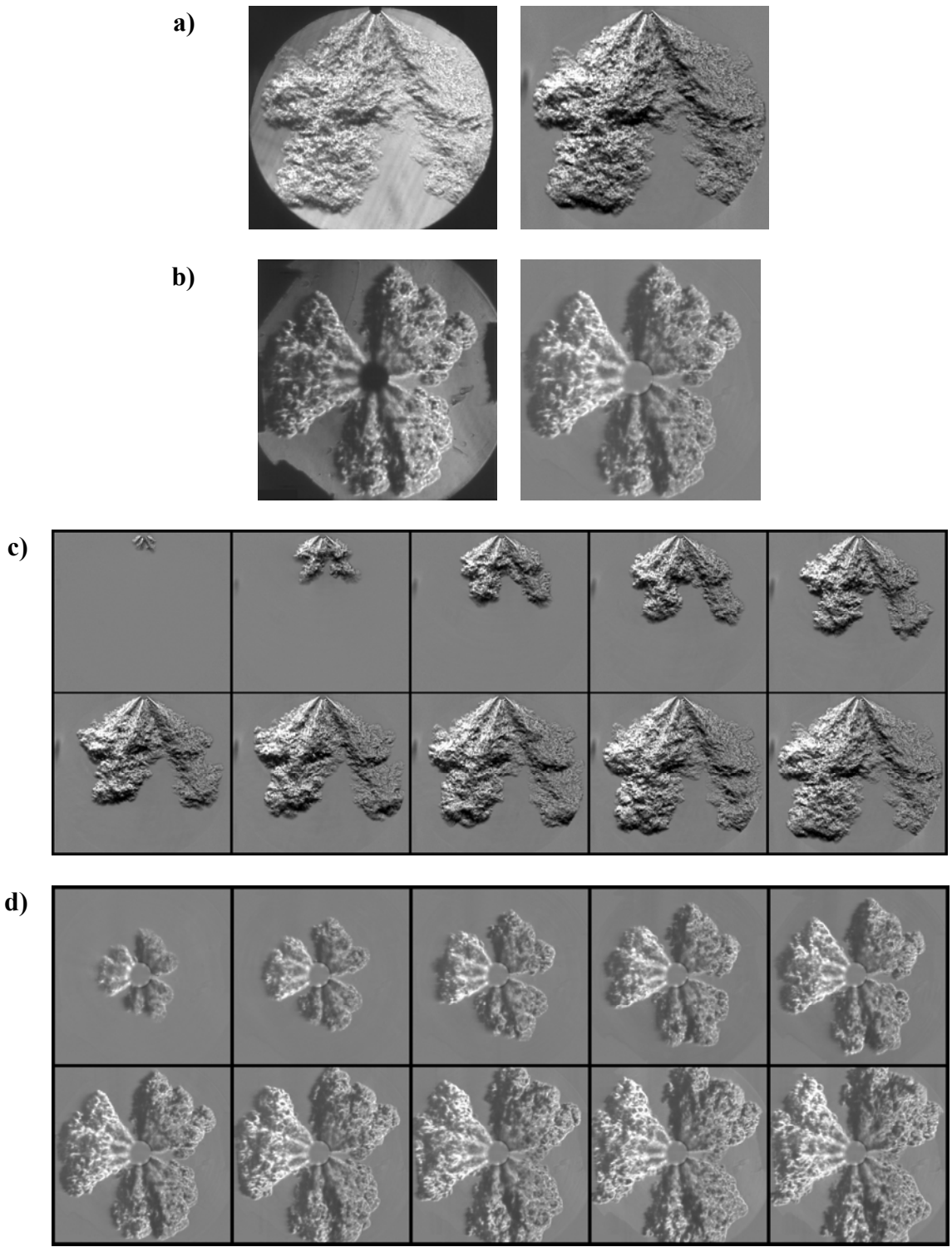

Figure 4.3. a) Original and corrected side-view images of jet pattern produced by the nine-hole injector **b)** original and corrected end-on images **c)** time series of side-view images, $\Delta t = 208$ μsec **d)** time series of end-on images, $\Delta t = 122$ μsec, $P_0 = 104$ bar (hydrogen), $\rho_{ch} = 3.4$ kg/m ^{3} (nitrogen).

4.1.4 Thirteen-hole Injector

Figures 4.4a)-d) display images of jet patterns produced by the thirteen-hole injector with an injection pressure, P_0, of 104 bar and a chamber pressure, ρ_{ch}, of 3.8 kg/m^3 with the same frame rates as the previous injectors. The injected gas was hydrogen while the chamber was filled with ambient nitrogen. Extensive interaction between jets in the flowfield causes the injected fluid to coalesce into one large jet. The designed included angle between the outer jets is 60° as shown in Fig. 4.5, but due to jet-to-jet interactions the actual angle is closer to 40°. Relatively low mixing occurs between the main fuel jet and the ambient chamber gas, which can result in unwanted combustion characteristics. Instead of mixing occurring between thirteen individual jets, entrainment can only occur at the outer edges of the single main jet. Extraneous slow-moving clouds of gas also break off near the injector tip and are later entrained back into the main jet, further affecting the mixing in the flow pattern.

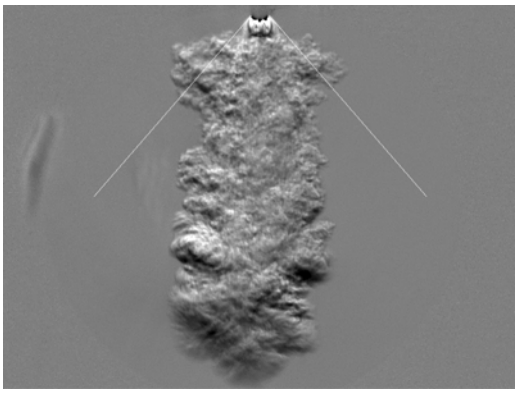

Figure 4.5. Side-view image of thirteen hole injector, P_0 = 104 bar (hydrogen), ρ_{ch} = 1.15 kg/m^3 (nitrogen).

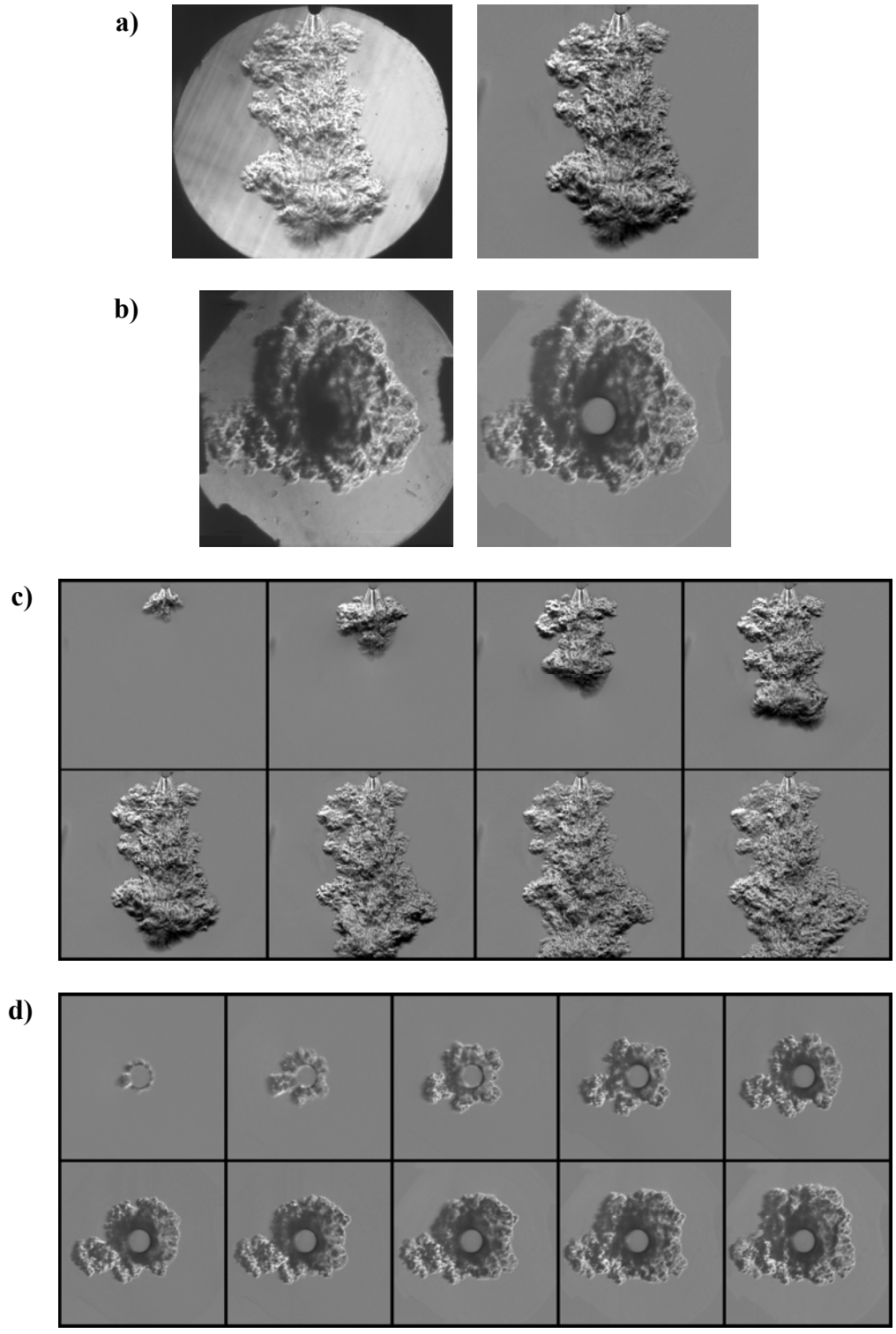

Figure 4.4. a) Original and corrected side-view images of jet pattern produced by the thirteen-hole injector **b)** original and corrected end-on images **c)** time series of side-view images, $\Delta t = 208$ μsec **d)** time series of end-on images, $\Delta t = 122$ μsec, $P_0 = 104$ bar (hydrogen), $\rho_{ch} = 3.4$ kg/m ^{3} (nitrogen).

4.2 Underexpansion Features

Diatomic jets with a stagnation to chamber pressure ratio above 1.89 are underexpanded and undergo a complex expansion process outside the nozzle exit. Intersecting expansion and compression waves create barrel shaped structures containing large gradients in density that are clearly captured by the schlieren system. These structures were present in the flows produced by each injector as shown in Figs. 4.6a) – d). The three-, seven-, and nine-hole injectors produce the classic barrel structures in individual jets while the individual structures produced by the thirteen-hole injector appear to coalesce and create a single, larger shock structure.

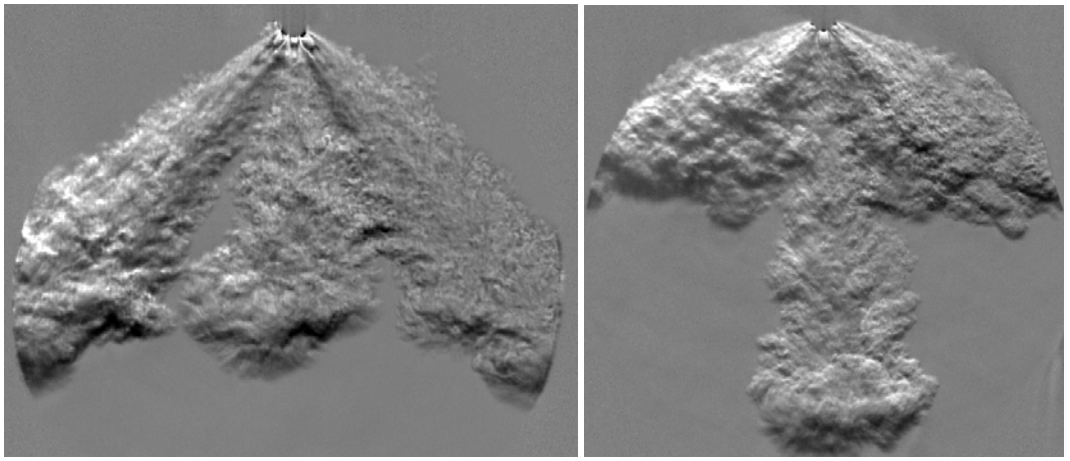

(a) **(b)**

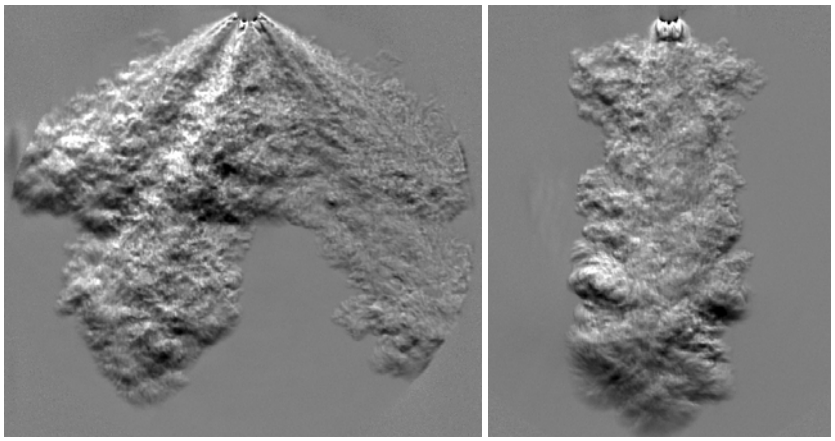

(c) **(d)**

Figure 4.6. Images displaying underexpansion features in hydrogen jets produced by the **a)** three-hole injector, **b)** seven-hole injector, **c)** nine-hole injector, and **d)** thirteen-hole injector, P_0 = 104 bar (hydrogen), Nitrogen ρ_{ch} = 1.15 kg/m^3 (nitrogen).

Figure 4.7 displays how the shock structures increase in size and also repeat further downstream as the injection pressure is increased from P_0 = 52 bar to P_0 = 104 bar. The increased pressure gradient at the nozzle exit causes the flow to expand more and thus causes the resulting waves to be stronger and increase the extent and diameter of the barrel structure. Figure 4.8 shows the measured spacing between the nozzle exit and the initial Mach disk. The spacing was found to follow a similar dependence to that measured by Ewan and Moodie [29].

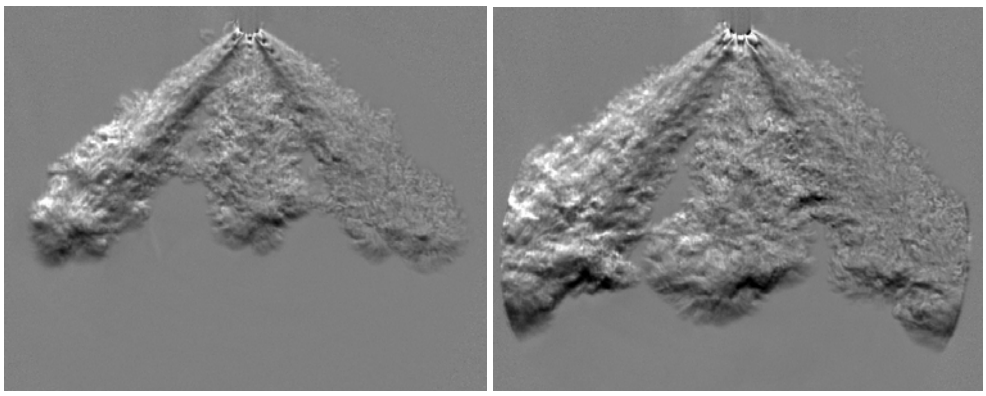

(a) **(b)**

Figure 4.7. Images displaying underexpansion features in hydrogen jets produced by the three-hole injector **a)** P_0 = 52 bar (hydrogen), ρ_{ch} = 1.15 kg/m^3 (nitrogen) and **b)** P_0 = 104 bar (hydrogen), ρ_{ch} = 1.15 kg/m^3 (nitrogen).

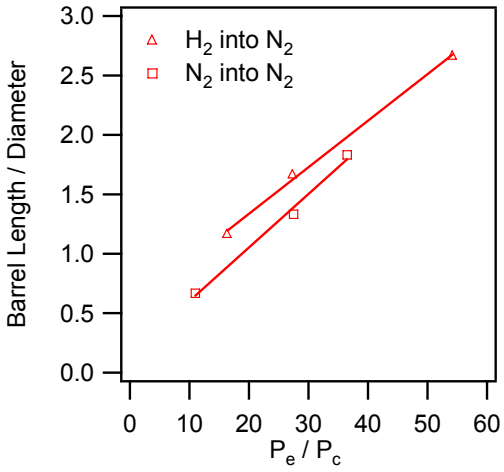

Figure 4.8. Spacing between nozzle exit and first Mach disk for hydrogen jets.

To investigate these structures independent of the mixing process, nitrogen was injected into nitrogen. The resulting images, shown in Fig. 4.9 for a single injection pressure and three different chamber densities, are a result of the complex pressure waves present in the flowfield. As the chamber density is increased the structures become smaller and are not present when the chamber density is increased to 8.17 kg/m^3. Figure 4.9a clearly shows the repeating structures extending far downstream, reducing in size, and finally damped out by the effects of viscosity. The size of these structures indicates that the pressure waves outside the nozzle exit are an important aspect of the flow and are on the order of the important length scales within the flow.

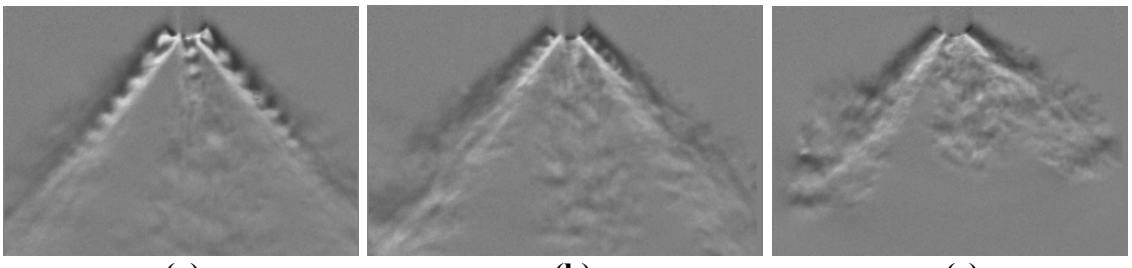

(a) **(b)** **(c)**

Figure 4.9. Nitrogen jets produced by three-hole injector, P_0 = 70 bar (nitrogen) **a)** ρ_{ch} = 1.15 kg/m^3 (nitrogen), b) ρ_{ch} = 3.80 kg/m^3 (nitrogen), and **c)** ρ_{ch} = 8.17 kg/m^3 (nitrogen).

4.3 Jet Penetration Measurements

The following section will provide examples of the penetration data collected in this study. All of the data presented was measured along the centerline of an individual jet produced by either the three- or seven-hole injector. Measurements from the other injectors are omitted because an individual jet cannot be identified within the flowfield produced by the nine- and thirteen-hole injectors.

4.3.1 Injection Pressure Dependence

Figures 4.10 and 4.11 show penetration data for the three-hole injector at various injection pressures and chamber densities of 3.8 kg/m^3 and 8.17 kg/m^3, respectively. Multiple runs of each condition are presented to show the run-to-run repeatability. As expected, the penetration increases as the injection pressure is increased, due to the additional momentum that is supplied to the jet at the injector exit. It should be noted that all of the penetration data presented in this section were corrected back to time zero by applying a linear fit to the first two data points and making the appropriate time shift back to zero time.

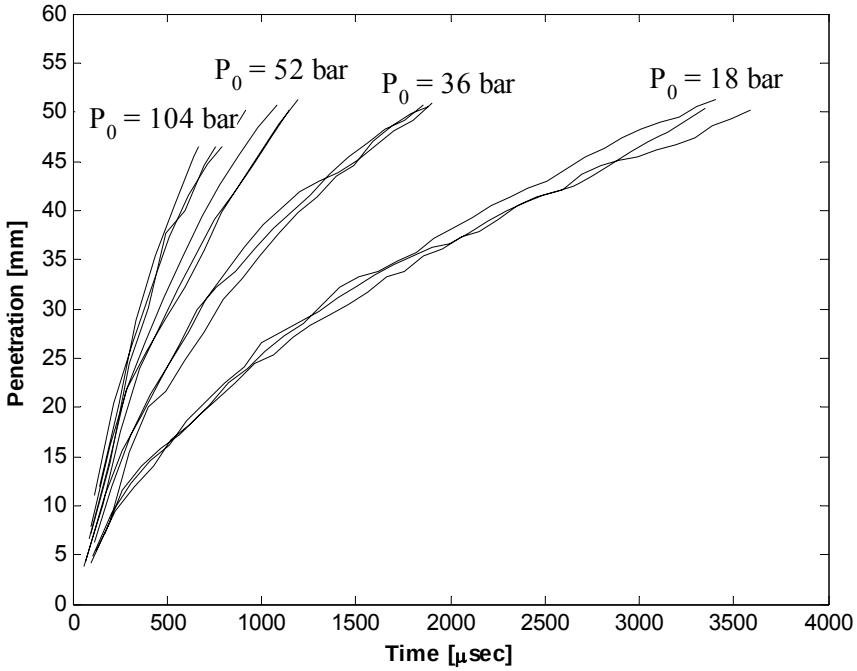

Figure 4.10. Hydrogen penetration as a function of time for three-hole injector at various stagnation injection pressures (hydrogen), ρ_{ch} = 3.8 kg/m^3 (nitrogen).

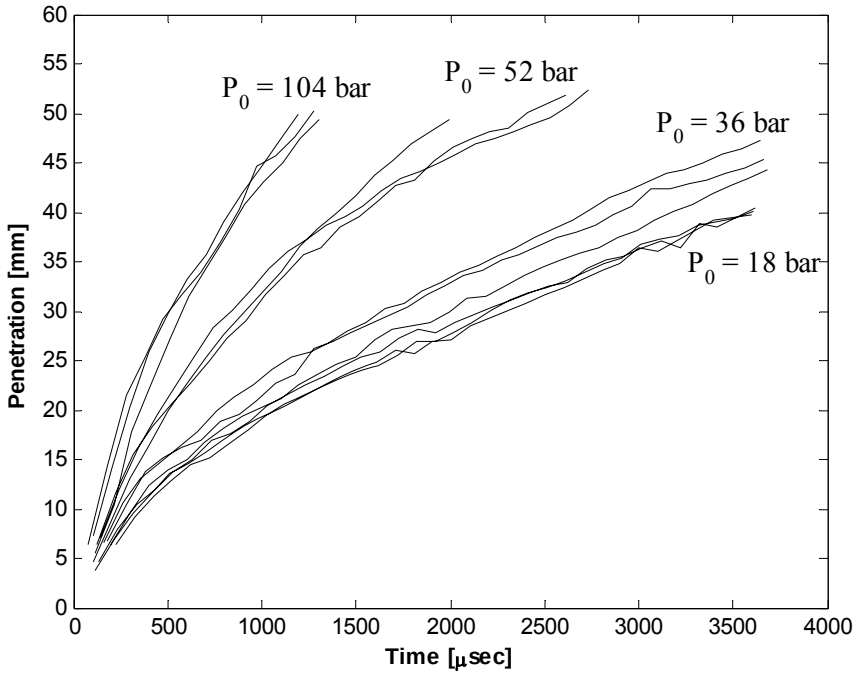

Figure 4.11. Hydrogen penetration as a function of time for three-hole injector at various stagnation injection pressures (hydrogen), ρ_{ch} = 8.17 kg/m^3 (nitrogen).

4.3.2 Chamber Density Dependence

Figures 4.12 and 4.13 show penetration data for the three-hole injector at injection pressures of 52 bar and 104 bar, respectively, for various chamber densities. The penetration decreases as the chamber density increases. This is caused by the higher inertia of the fluid elements that the injected fluid must accelerate and push aside.

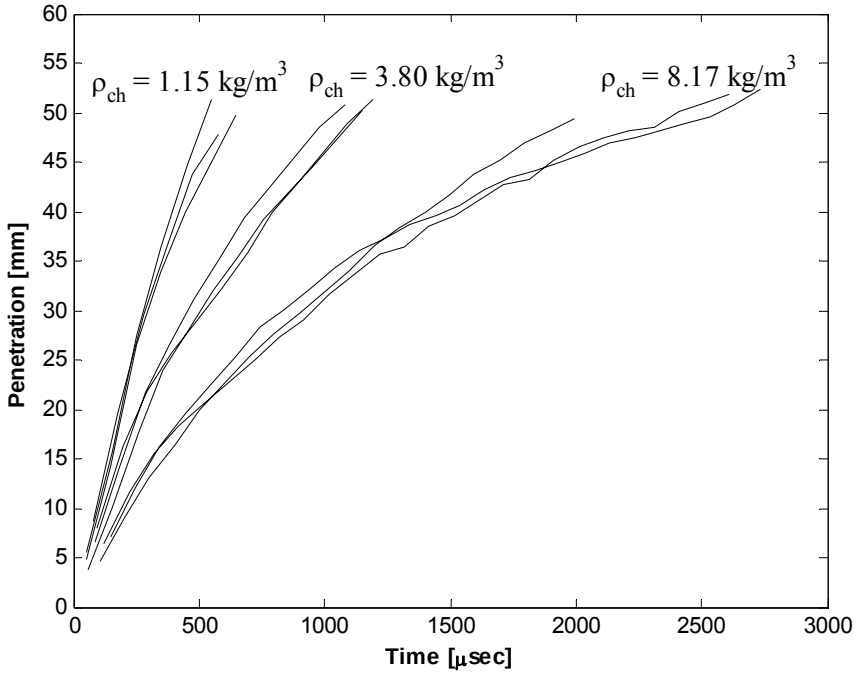

Figure 4.12. Penetration as a function of time plots for three hole injector, P_0 = 52 bar (hydrogen) at various chamber densities (nitrogen).

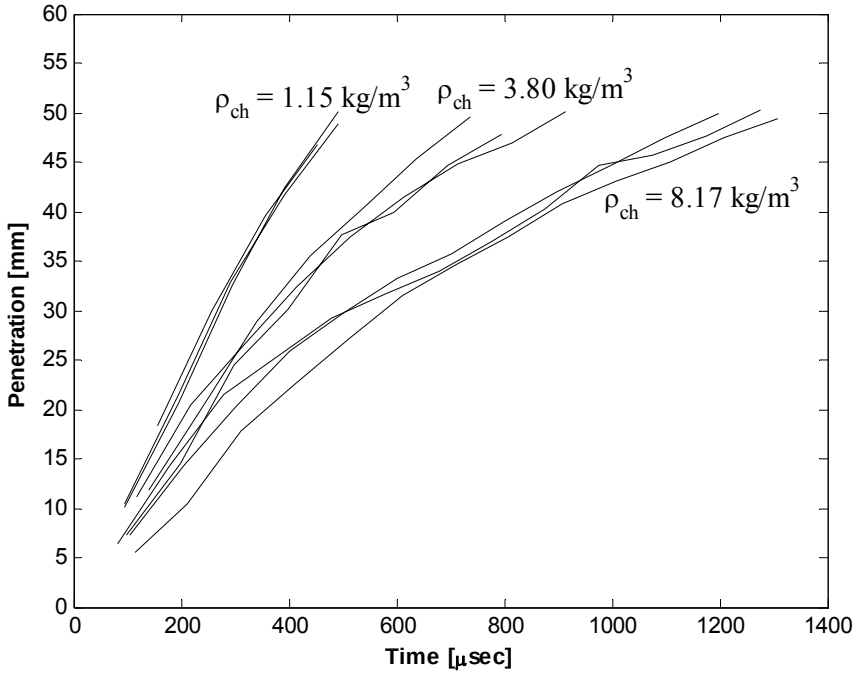

Figure 4.13. Penetration as a function of time plots for three hole injector , P_0 = 104 bar (hydrogen) at various chamber densities (nitrogen).

4.3.4 Medium Dependence

Most of the conditions tested in this study were performed using both hydrogen and helium as the injected medium, two gases with similar molecular weights and densities but different specific heat ratios, γ. Figures 4.14 and 4.15 show several penetration plots for various conditions for both the three- and seven-hole injectors, where either hydrogen or helium was injected. There is essentially no difference in the penetration behavior of hydrogen or helium jets produced by these two injectors; indicating that the ratio of specific heats, γ, does not play a major role in the penetration of these jets.

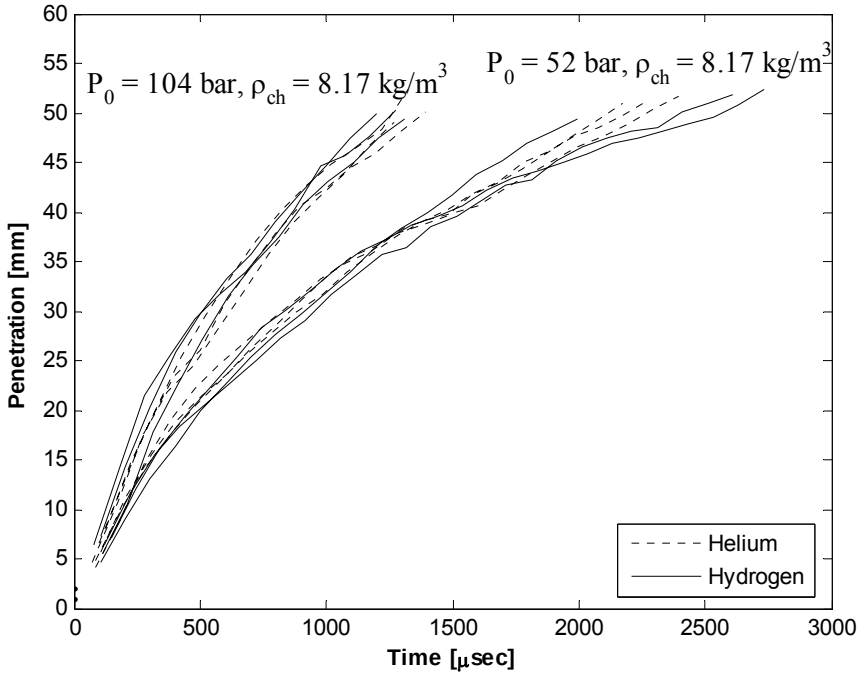

Figure 4.14. Penetration as a function of time for hydrogen or helium as injected fluid from three-hole injector, ρ_{ch} = 8.17 kg/m^3 (nitrogen).

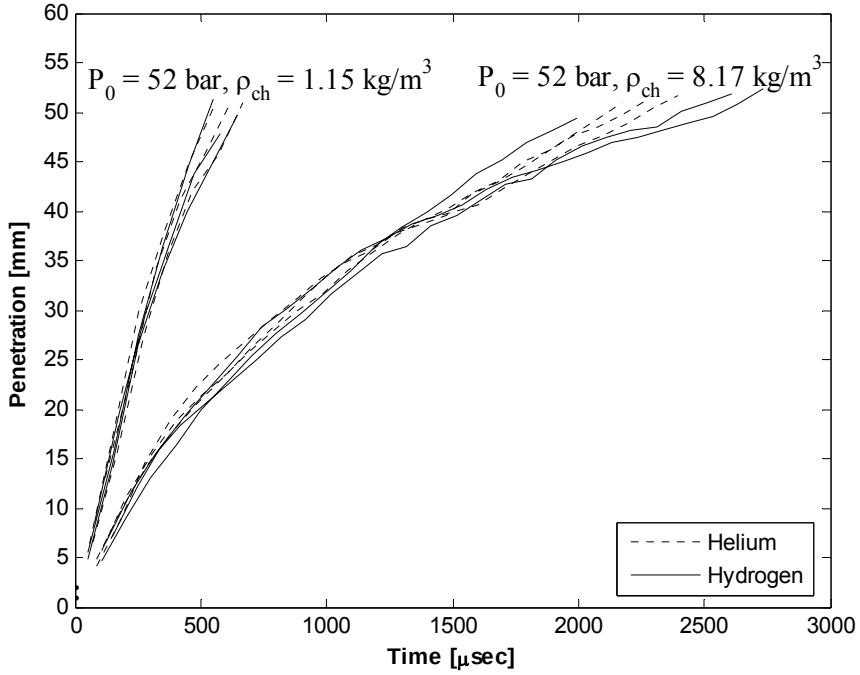

Figure 4.15. Penetration as a function of time for hydrogen or helium as injected fluid from seven-hole injector, P_0 = 52 bar.

5.0 Data Normalization

Nondimensionalization is important to identify the controlling physical parameters of a particular flow, in this case transient free jets. It can also be used to collapse data to a single relationship that encompasses a wide range of conditions. This single relationship can then be applied to similar flows, and data can easily be extracted without further experimentation. This chapter investigates different methods of normalizing jet penetration rate data to provide a single relation between nondimensional penetration and nondimensional time. The scaling relationships presented in Chapter 2 will be used and the collapse of the subsequent data will be quantified. Methods of correcting the raw penetration versus time data back to the origin will also be investigated. The data presented in this chapter came from the three-hole and seven-hole injectors exclusively, because a single unaffected jet could be isolated for these injectors.

5.1 Penetration versus Time

The raw penetration data needs to be corrected in all cases because the exact beginning of injection happens between recorded images and cannot be directly determined. The proper time shift must be made to analyze the data from an equivalent starting point, and to compare data between separate runs. The time correction is made by applying a functional fit to the data and then linearly shifting the time so the fitted curve passes through the origin. One method is to apply a linear fit to the first two penetration versus time data points, and then subtract the time axis intercept of the curve fit from the raw time data. This method is used because at early times the penetration may not follow the traditional square-root of time dependence due to either physical phenomena or transient effects of the needle lift within the injector tip. This method also

ensures that every data set for each condition appears to originate from the origin. An example of how the linear-fit time correction was applied to the data is displayed in Fig. 5.1, and Figs. 5.2 and 5.3 show all the hydrogen penetration data with the linear fit correction near the origin for the three- and seven-hole injectors.

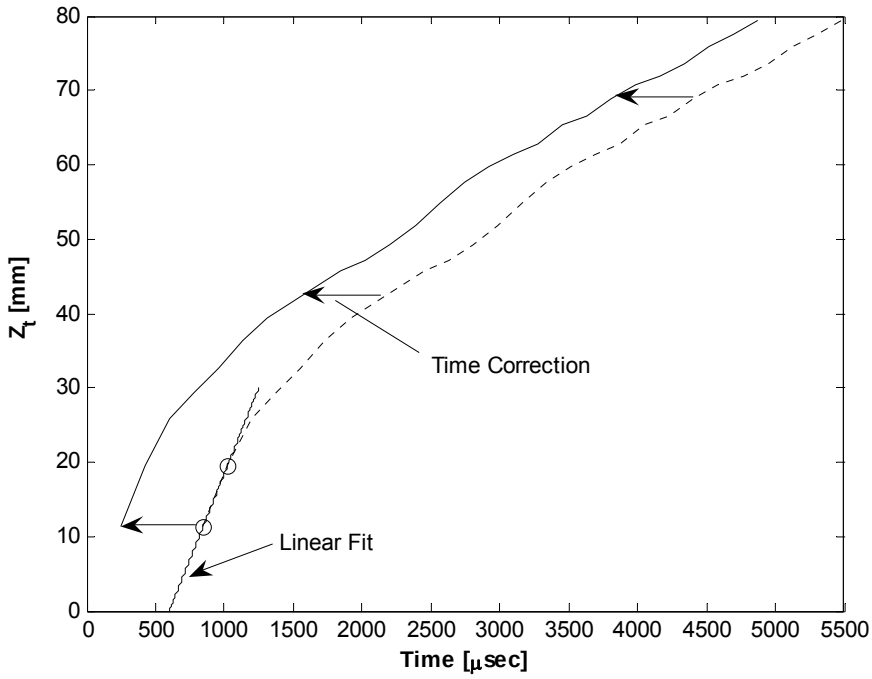

Figure 5.1. Example of linear fit to first two data points and subsequent time shift.

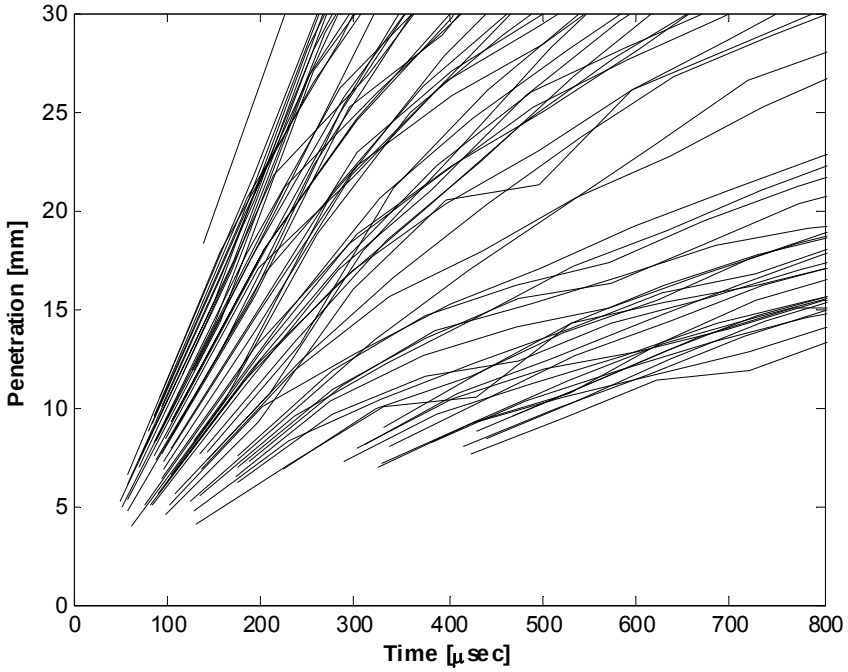

Figure 5.2. Hydrogen penetration data for three-hole injector with linear fit correction.

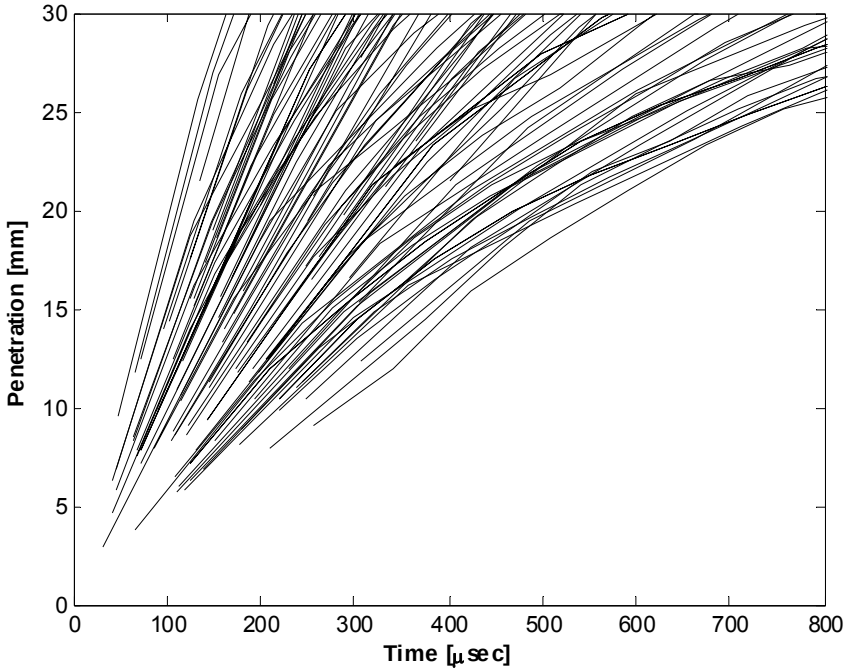

Figure 5.3. Hydrogen penetration data for seven-hole injector with linear fit correction.

Another method is to apply a square root fit to all the penetration rate data points in an individual run. The two-parameter fit that was applied to the measured data is given in equation (5.1)

$$Z_t = a_1 \left(t - t_0 \right)^{1/2} \tag{5.1}$$

where a_1 is a fitting parameter and t_0 is the time shift that is ultimately subracted from the raw data. Figure 5.4 shows an example of how this fit correction was applied, and Figs. 5.5 and 5.6 show the penetration data for both the three-hole and seven-hole injectors with the square root correction applied. The square root correction causes relatively more scatter near the origin with the data appearing to originate from numerous points, often from negative time values. This is due to the penetration data at early time not having the same time dependence as at later times.

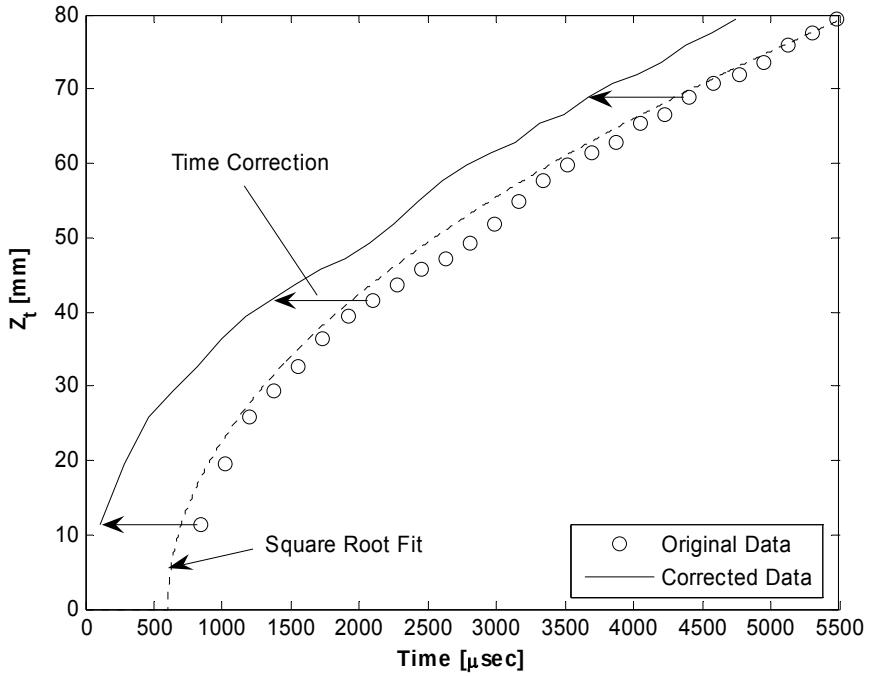

Figure 5.4. Example of square root fit to first two data points and subsequent time shift.

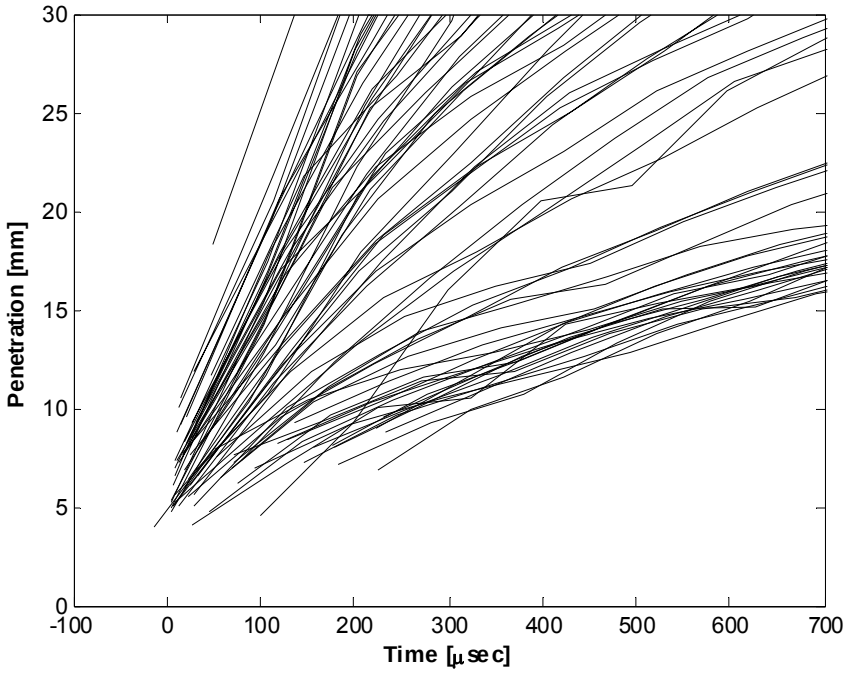

Figure 5.5. Hydrogen penetration data for three-hole injector with square-root fit correction.

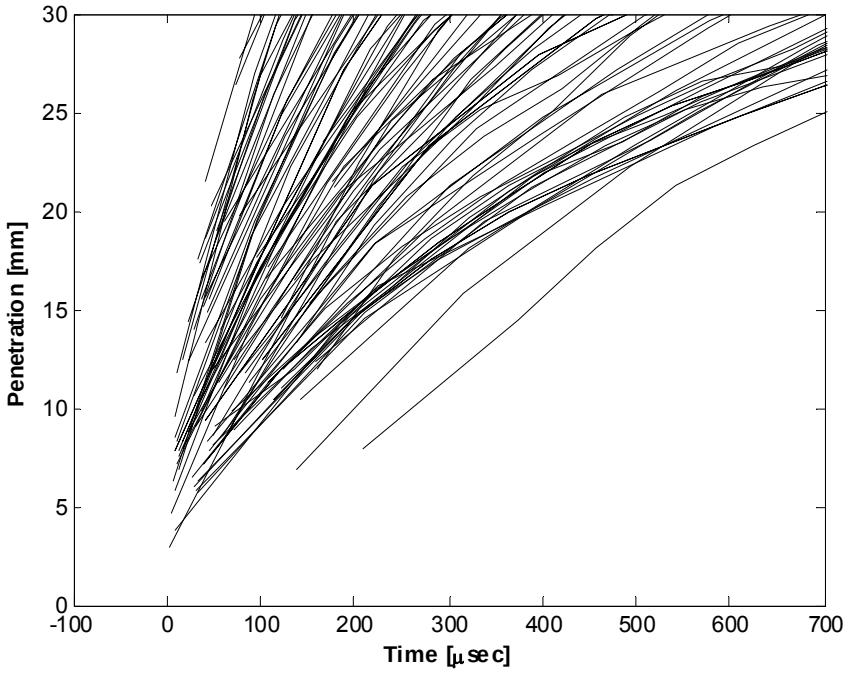

Figure 5.6. Hydrogen penetration data for seven-hole injector with square-root fit correction.

To investigate which correction method is better suited for the data it is advantageous to analyze different runs of the same condition. Figures 5.7a) and b) show penetration data from the same conditions after either the linear and square-root time corrections have been applied. It is clear that the square-root correction does a better job of collapsing the individual data from similar conditions, especially for data sets where data at early times were not able to be collected due to the velocity of the jet tip.

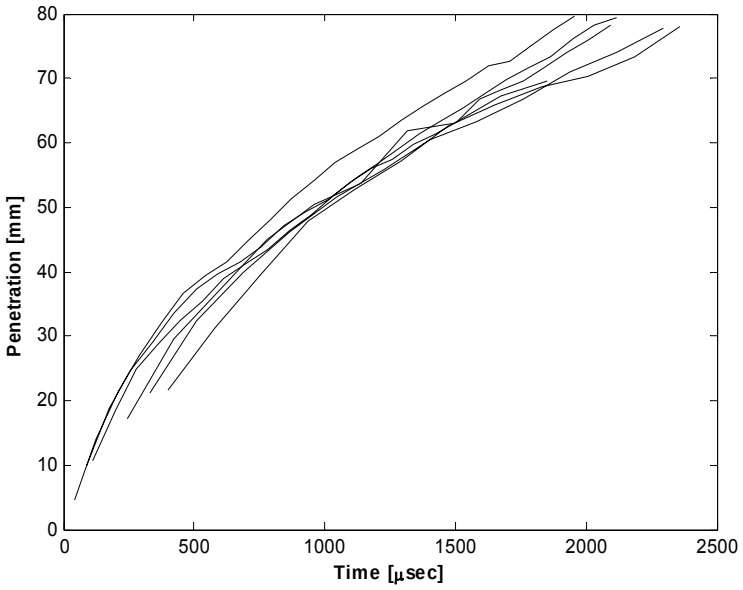

(a)

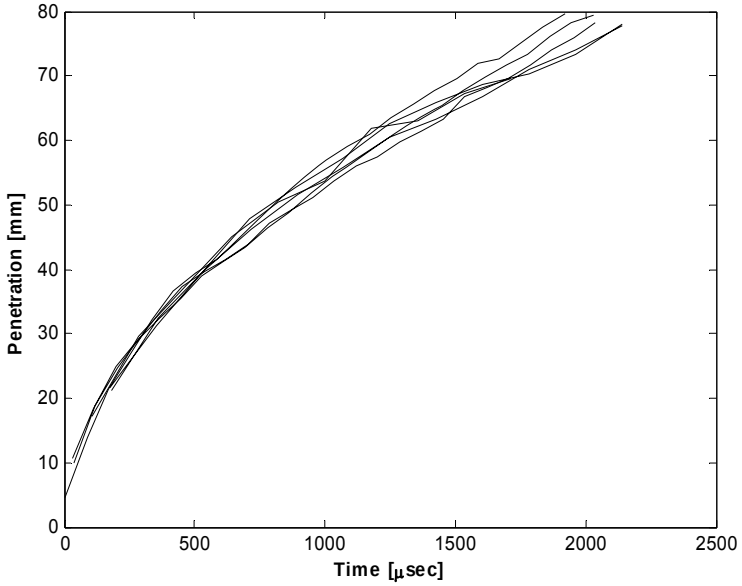

(b)

Figure 5.7. Penetration data for individual runs of the seven-hole injector, P_0 = 18.3 bar (hydrogen), ρ_{ch} = 8.17 kg/m^3 (nitrogen) **a)** linear fit time correction **b)** square root fit time correction.

Further, Naber and Siebers [25] showed that the nondimensional spray or jet penetration (equation (5.2)) has a linear dependence on time when the nondimensional time (equation (5.3)) is less than unity; i.e. $\overline{z}_{n,\theta} = \overline{t}_{n,\theta}$.

$$\overline{z}_{n,\theta} \equiv \frac{Z_t}{z^+_{n,\theta}} \quad ; \quad z^+_{n,\theta} = \frac{d_f \sqrt{\tilde{\rho}}}{a \tan(\theta/2)} \tag{5.2}$$

$$\overline{t}_{n,\theta} \equiv \frac{t}{t^+_{n,\theta}} \; ; \quad t^+_{n,\theta} = \frac{d_f \sqrt{\tilde{\rho}}}{a \tan(\theta/2) u_f} \tag{5.3}$$

A value of 0.66 was used for the constant a. For the conditions used in this study a nondimensional time of one corresponds to a time value of less than approximately 10 μs, which is before any data were collected for all experiments. Although the linear fit correction appears to do a better job of correcting the data at early times, the square-root method does a better job of correcting the penetration data overall.

5.2 Penetration versus the Square Root of Time

Plots of penetration versus the square root of time provide a visual measure of how well the data follows a square root of time dependence. Figures 5.8 and 5.9 show all of the hydrogen data for the three-hole and seven-hole injectors respectively. While the seven-hole injector data falls into straight lines, indicating a square root dependence on time throughout the investigated injection duration, the three-hole injector data has some curvature at early times. This suggests transient behavior during the intial portion of the injection and the traditional jet behavior starts downstream from the injector exit at later times. The slope of the linear portion of each data set is also different for each condition. This is due to the differences in both the momentum supplied to the jet and the density of the ambient gas for differing conditions. These both contribute to changing the rate at which the penetration changes with the square root of time.

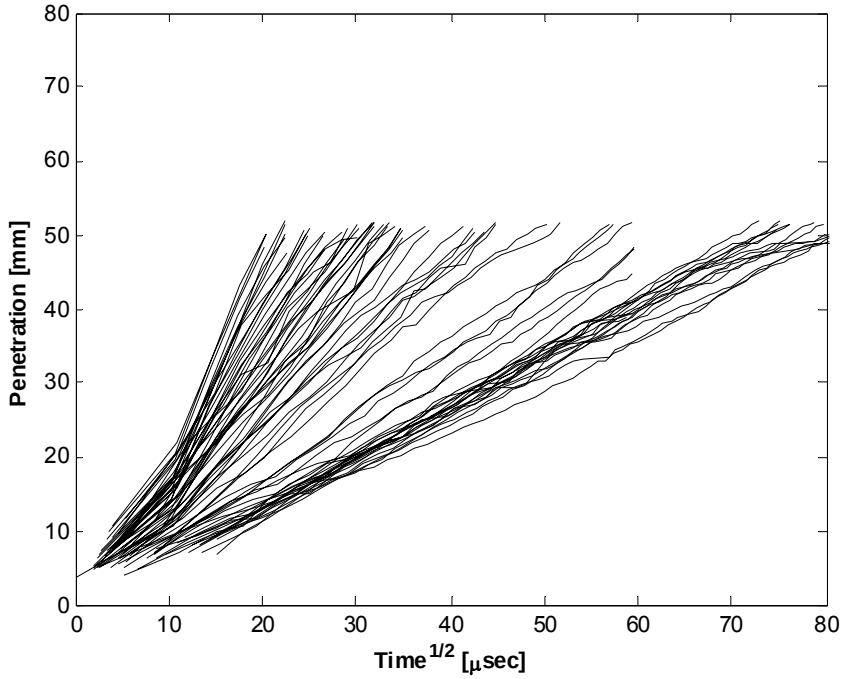

Figure 5.8. Hydrogen penetration versus the square root of time for three-hole injector.

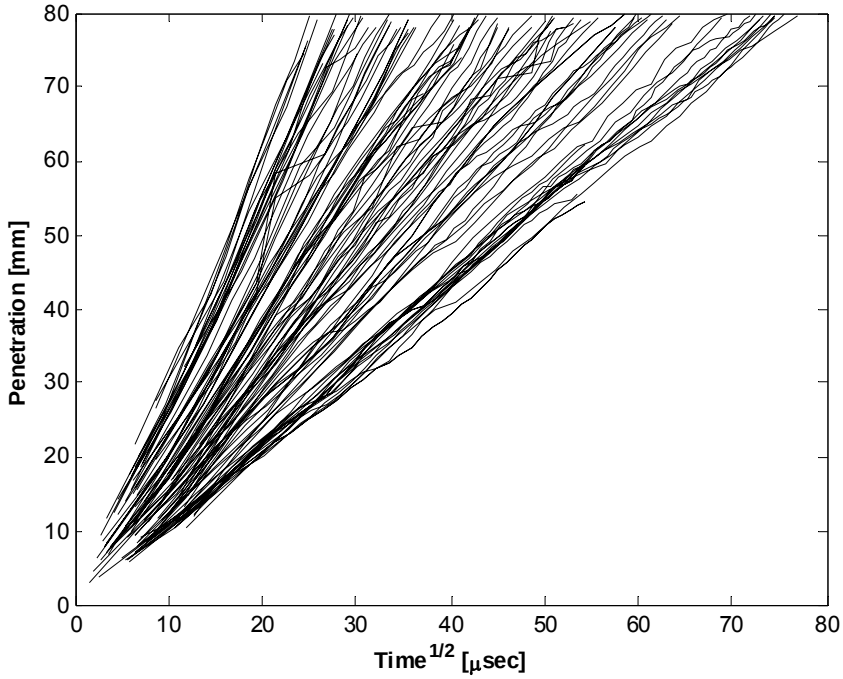

Figure 5.9. Hydrogen penetration versus the square root of time for seven-hole injector.

5.3 Penetration Rate Data Normalization

The goal of the proceeding sections is to choose the proper nondimensional parameters to collapse the slopes of the data shown in Figs. 5.8 and 5.9 to a single line. Five main jet penetration-scaling methods will be investigated and the degree to which each method collapses the data will be quantitatively evaluated. Further, injector characteristics such as the discharge coefficient and rate shape will be included to determine their effect on the nondimensionalization.

5.3.1 Subsonic Jets

Hydrogen jets with a nozzle exit to chamber pressure ratio below 1.89 and helium jets with a pressure ratio less than 2.05 are not choked at the nozzle exit and are nowhere sonic in the flowfield. Previous investigators [11,20,21,23] have shown that the proper characteristic time and length scales for subsonic, un-choked jets with non-uniform density as the chamber fluid are given in eqs. (5.4) and (5.5), with the resulting nondimensional penetration and time given in equations (5.6) and (5.7). These scaling relations use nozzle exit properties to nondimensionalize the jet tip penetration and time and will be referenced here as the nozzle exit normalization method.

$$z_n^+ = \left(\frac{\rho_n}{\rho_{ch}}\right)^{1/2} d_n = d_{eq} \tag{5.4}$$

$$t_n^+ = \frac{d_n\sqrt{\frac{\rho_n}{\rho_{ch}}}}{u_n} = \frac{d_{eq}}{u_n} \tag{5.5}$$

$$\overline{z}_n = \frac{Z_t}{z_n^+} \tag{5.6}$$

$$\overline{t}_n = \frac{t}{t_n^+} \tag{5.7}$$

Figures 5.10 and 5.11 show all the hydrogen and helium data normalized with nozzle parameters for conditions where the flow is not choked at the injector nozzle exit. The solid line in Fig. 5.10 has a slope that is the mean of the slopes of the individual cases and the dashed lines indicate the 95 percent confidence interval in the mean slope. The equations for these lines are provided in their respective plots.

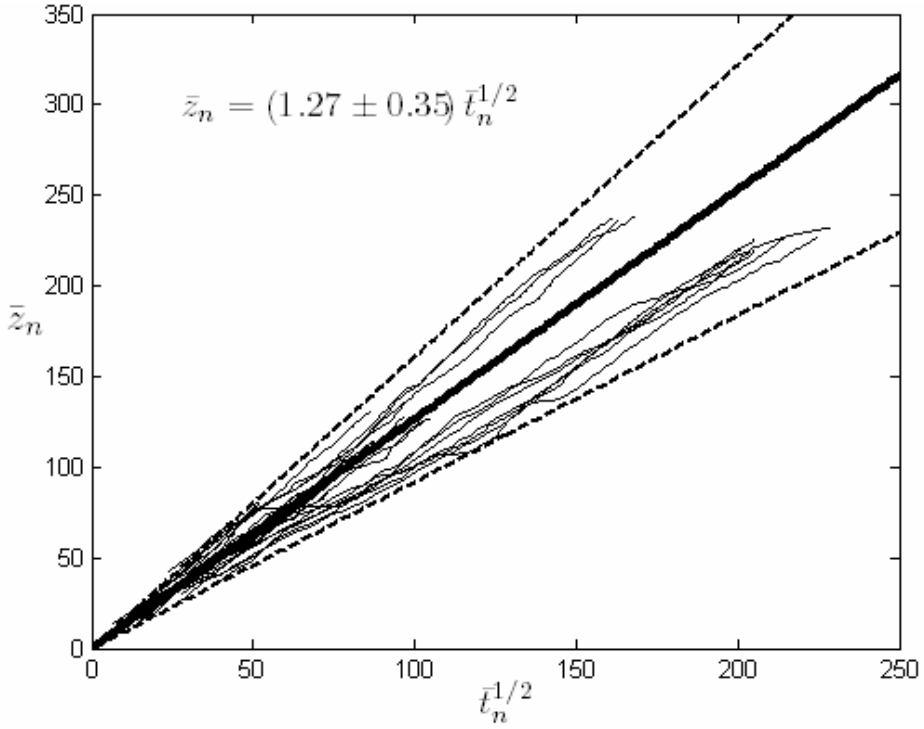

Figure 5.10. Normalized penetration as a function of the square root of the normalized time using nozzle properties for the three-hole injector, includes all non-choked hydrogen and helium injection data.

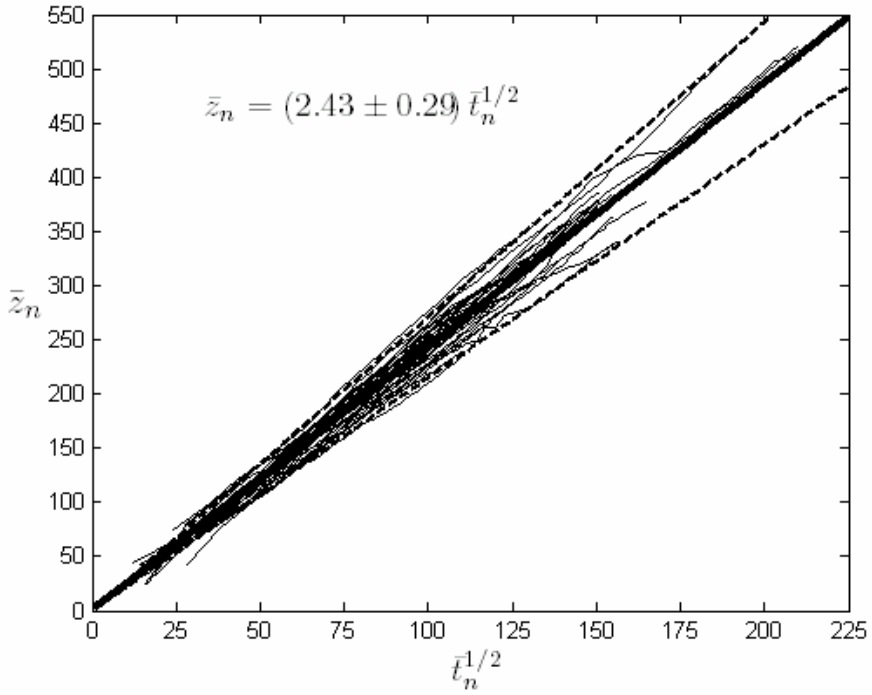

Figure 5.11. Normalized penetration as a function of the square root of the normalized time using nozzle properties for the seven-hole injector, includes all non-choked hydrogen and helium injection data.

The slope value of 1.27±0.35 determined for the three-hole injector is significantly lower than the range of previously reported values between 2.14 and 2.9 [17,18,20,21], while the 2.43±0.29 value for the seven-hole injector falls within this range. The confidence intervals represent ±27.6% of the mean slope for the three-hole injector and ±14.5% for the seven-hole injector, indicating the seven-hole injectors subsonic data collapses more tightly relative to the three-hole injector.

5.3.2 Choked Jets

5.3.2.1 Normalization of Data via Nozzle Parameters

Previous authors [21] have extended the usage of the nozzle exit scaling parameters that were used with the subsonic, unchoked jets to flows that are choked and underexpanded.

5.3.2.1.1 Three-hole Injector

Figure 5.12 shows all of the hydrogen and helium data under choked conditions from the three-hole injector normalized with the parameters given in equations (5.4) through (5.7).

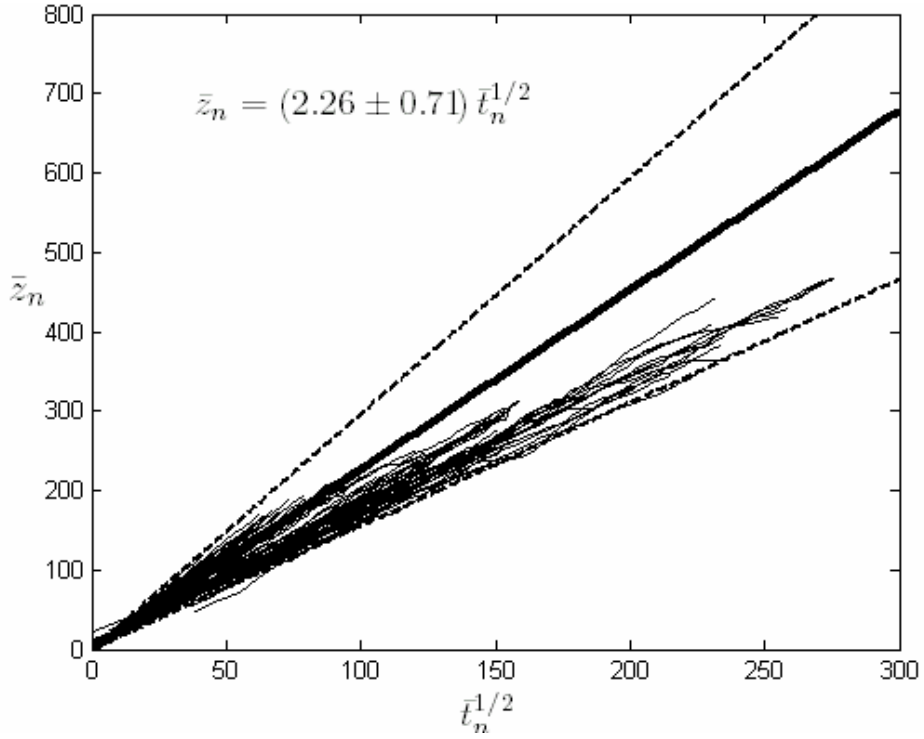

Figure 5.12. Normalized penetration as a function of the square root of the normalized time using nozzle exit properties for the three-hole injector, includes all choked hydrogen and helium injection data.

The collapse of the data is clearly not complete with this nondimensionalization scheme for this injector. The confidence interval represents ±31.4% of the mean slope value of

2.26, which is lower than the 2.82 value reported by Hill and Oulette [21] for their underexpanded data. Upon closer inspection, two subsets of the data were identified where the data, especially the slopes, collapse more closely. The first subset includes the data that has a nozzle exit to chamber pressure ratio above 3.0, $P_n/P_{ch} > 3.0$, and is shown in Fig. 5.13. These data lie in the upper left portion of the entire data set shown in Fig. 5.12 with the slopes of the data collapsing to within ±14.5% of the mean slope value. The second subset includes conditions with a exit to chamber pressure ratio below 3.0, $P_n/P_{ch} < 3.0$, and is shown in Fig. 5.14. The slopes of these data fall within ±13.7% of their associated mean slope value. The mean slope and 95 percent confidence interval of each data set are provided in their respective plots. The separation of these two subsets of data at $P_n/P_{ch} = 3.0$ could be a result of Mach disk formation at this exit pressure ratio. Prior to the formation of the Mach disk the oblique shock waves that make up the barrel shock structure are able to intersect at the jet axis. As P_n/P_{ch} increases, the oblique barrel shocks can no longer curve enough to meet at the axis and a normal shock forms the Mach Disk. This change in flow pattern may cause the separation in the penetration rate seen in the nondimensional data. Cumber et al. [27] reported the onset of the normal shock that forms the Mach disk occurs at a pressure ratio closer to 2.1, slightly lower than 3.0.

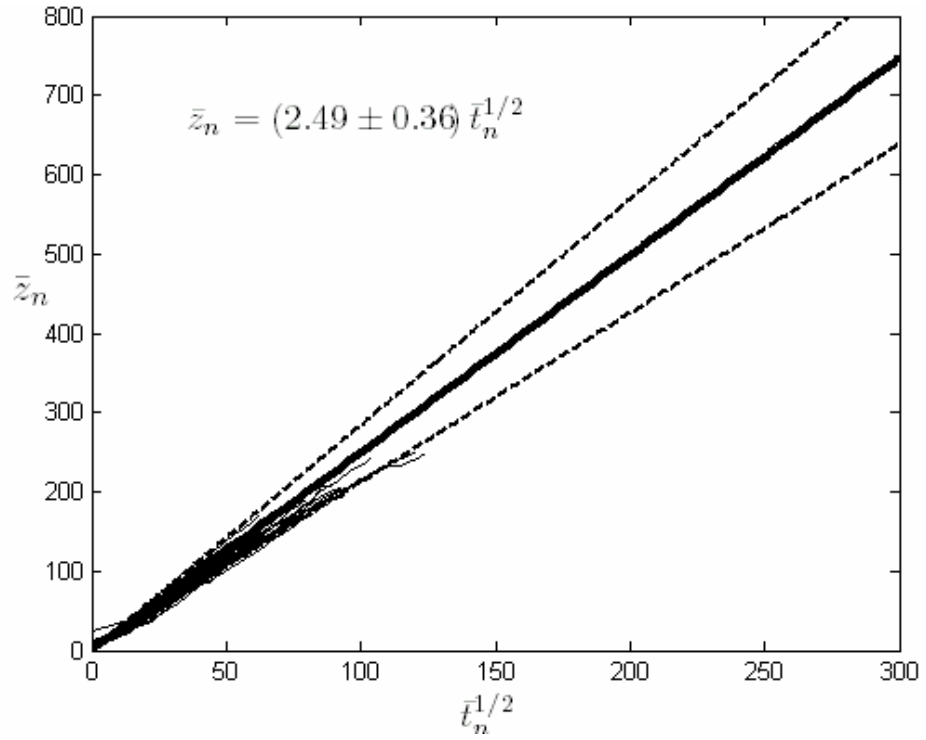

Figure 5.13. Normalized penetration as a function of the square root of the normalized time using nozzle properties for the three-hole injector, $P_n/P_{ch} > 3.0$.

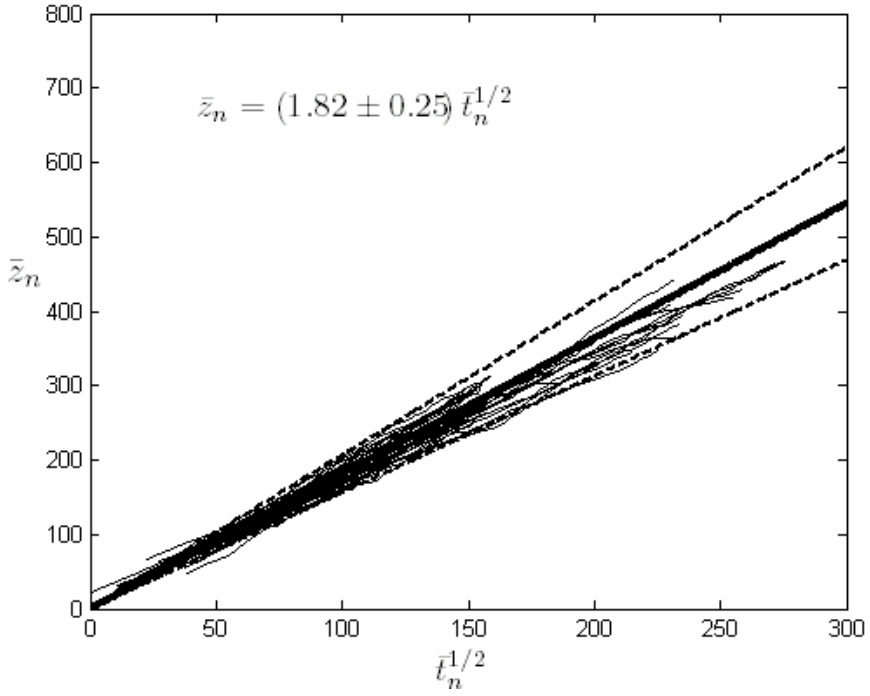

Figure 5.14. Normalized penetration as a function of the square root of the normalized time using nozzle properties for the three-hole injector, $P_n/P_{ch} < 3.0$.

5.3.2.1.2 Seven-hole Injector

The data for the seven-hole injector collapses much more completely for the hydrogen and helium data under choked exit conditions shown in Fig. 5.15. The mean slope value was found to be 2.76±0.40 for the entire data set. This confidence interval represents ±14.5% of the mean slope, compared to ±31.4% for the three-hole injector. Further, the mean slope is very similar to the value of 2.82 reported by Hill and Oulette [21].

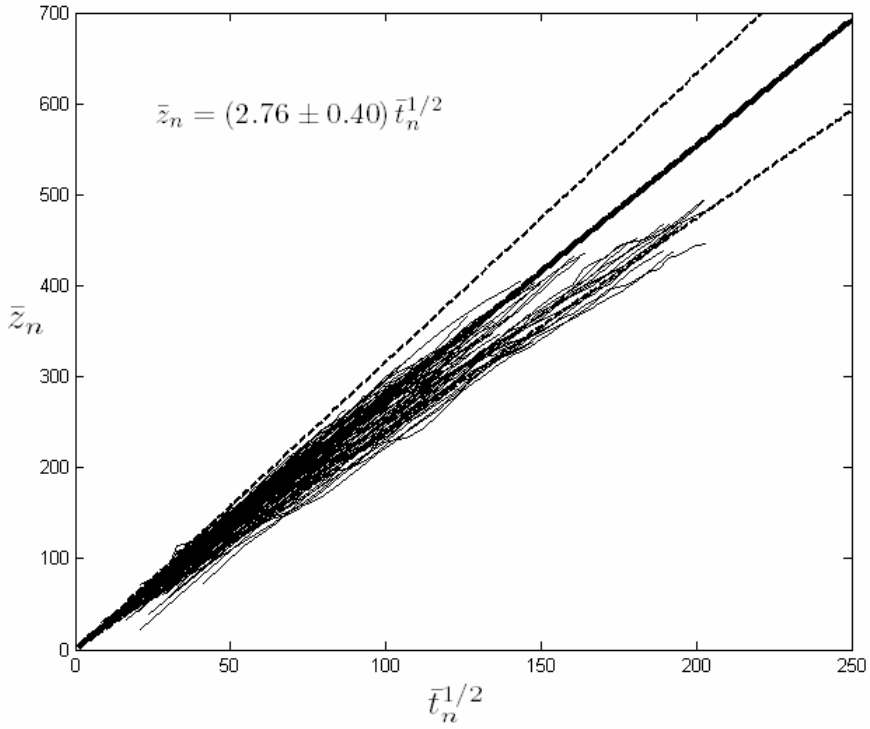

Figure 5.15. Normalized penetration as a function of the square root of the normalized time using nozzle properties for the seven-hole injector, includes all choked hydrogen and helium injection data.

A better collapse of the data can also be achieved for the seven-hole injector when the data are divided into groups where the exit to chamber pressure ratio is either above or below 1.7. Plots of these two groups are shown in Figs. 5.16 and 5.17 with the corresponding slope statistics provided in the plots. Again, the separation of data could

be a result of Mach disk formation at P_n/P_{ch}=1.7, compared to 3.0 for the three-hole injector, and 2.1 reported by Cumber et al [27]. The slopes of the data for P_n/P_{ch}>1.7 collapse to within ±9.1% of the mean value and ±13.6% for the P_n/P_{ch}>1.7 subset.

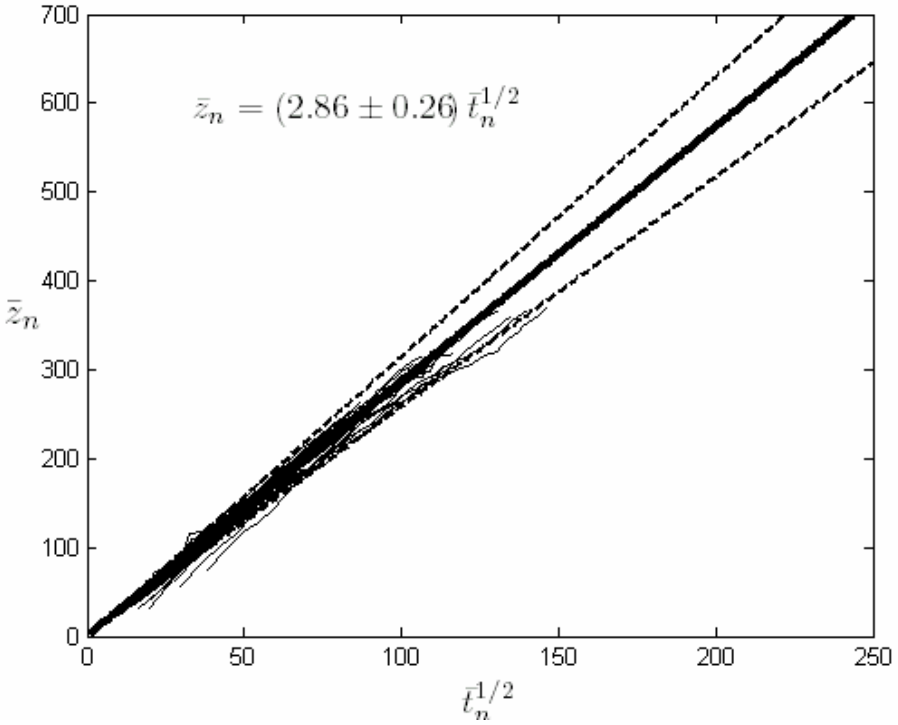

Figure 5.16. Normalized penetration as a function of the square root of the normalized time using nozzle properties for the seven-hole injector, P_n/P_{ch} > 1.7.

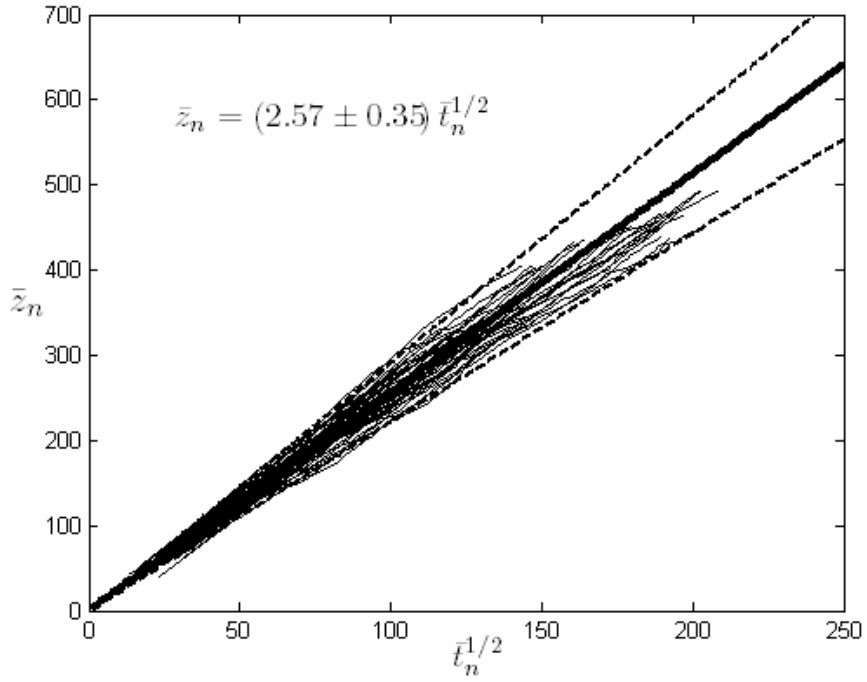

Figure 5.17. Normalized penetration as a function of the square root of the normalized time using nozzle properties for the three-hole injector, $P_n/P_{ch} < 1.7$.

5.3.2.2 Proposed Model: PMD Parameters

The previous model does not directly incorporate the complex expansion outside the nozzle exit that is present in underexpanded jets. In this study an additional model that includes the expansion and shock processes within the flow is proposed in an attempt to more completely collapse the penetration rate data. The model assumes the flow outside the nozzle expands isentropically to a location where a normal shock compresses the flow back to the chamber pressure. The location of the normal shock is termed the psuedo-Mach disk location, identified by the subscript PMD. The flow downstream of the PMD location is assumed to be a subsonic jet issuing from a larger nozzle at the chamber pressure. A schematic of this jet model is shown in Fig. 5.18. A similar model was previously used with momentum theory by Tsujimura *et al.*[36].

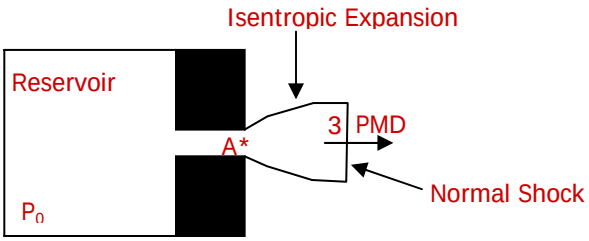

Figure 5.18. Schematic of proposed jet model.

The conditions at the PMD location are determined by combining the quasi-one dimensional isentropic flow and normal shock relations. The Mach number before the normal shock, M_3, and the area, A_{PMD}, the density, ρ_{PMD}, and the Mach number, M_{PMD}, at the PMD location are given in eqs.(5.12) through (5.15).

$$\frac{P_c}{P_0} = \frac{\dfrac{2\gamma M_3^2 - (\gamma - 1)}{\gamma + 1}}{\left(1 + \dfrac{\gamma - 1}{2} M_3^2\right)^{\gamma/(\gamma-1)}} \tag{5.8}$$

$$\frac{A_{PMD}}{A^*} = \frac{1}{M_3}\left(\frac{1 + \dfrac{\gamma - 1}{2} M_3^2}{\dfrac{\gamma + 1}{2}}\right)^{\frac{\gamma+1}{2(\gamma-1)}} \tag{5.9}$$

$$\frac{\rho_{PMD}}{\rho_0} = \frac{\dfrac{(\gamma + 1) M_3^2}{(\gamma - 1) M_3^2 + 2}}{\left(1 + \dfrac{\gamma - 1}{2} M_3^2\right)^{\frac{1}{\gamma-1}}} \tag{5.10}$$

$$M_{PMD}^2 = \frac{1 + [(\gamma - 1)/2] M_3^2}{\gamma M_3^2 - (\gamma - 1)/2} \tag{5.11}$$

The results from eqs. (5.8) – (5.11) as a function of the stagnation to chamber pressure ratio, P_0/P_{ch}, are shown in Fig. 5.19, where the results are normalized by the nozzle exit conditions for convenience. The pseudo-Mach disc diameter and density are found to follow a power-law scaling with the pressure ratio, with a ½ exponent for diameter and -1

exponent for density. The ½ power relation for the diameter agrees with the mass-balancing diameter proposed by Ewan and Moodie [13] and Birch *et al*. [14], which may explain the success that those authors experienced. There is, however, a multiplicative difference between all of the results.

It is interesting to note that the above scaling for diameter and density, and the relatively slight scaling of velocity provides a nearly constant momentum flux ratio for the pseudo-Mach disc state and the nozzle exit, i.e. $(\rho U^2 A)_{PMD}$ / $(\rho U^2 A)_n$ is weakly dependent on P_0/P_{ch}. The constant of proportionality is not, however, unity. Thus, scaling arguments based on the nozzle exit momentum will be preserved, but the quantitative value of the proportionality constant will be incorrect.

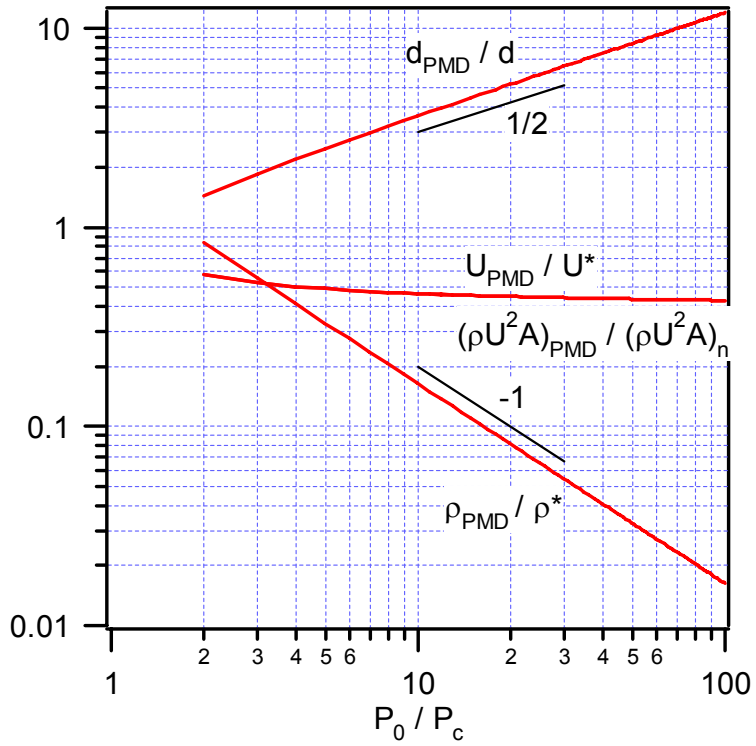

Figure 5.19. Diameter, velocity and density ratios for the pseudo-Mach disc state as compared to the nozzle exit condition.

The PMD properties can be used to create nondimensional parameters similar to the nozzle exit parameters, only the nozzle exit properties are replaced with the properties at the PMD location. The new nondimensional time and penetration are given in eqs. (5.12)and (5.13).

$$\overline{z}_{PMD} = \frac{Z_t}{d_{PMD}\left(\frac{\rho_{PMD}}{\rho_{ch}}\right)^{1/2}} \tag{5.12}$$

$$\overline{t}_{PMD} = \frac{tu_{PMD}}{d_{PMD}\left(\frac{\rho_{PMD}}{\rho_{ch}}\right)^{1/2}} \tag{5.13}$$

5.3.2.2.1 Three-hole Injector

Figure 5.20 shows all of the data from the three-hole injector recast in the PMD nondimensional variables. The collapse of the data is very similar to that of the nozzle exit parameter normalization method, with a change in the magnitude of the nondimensional scales being the main difference. The collapse of slopes using the PMD scaling is within ±34.3%, compared to ±31.4% when the nozzle exit scaling is used.

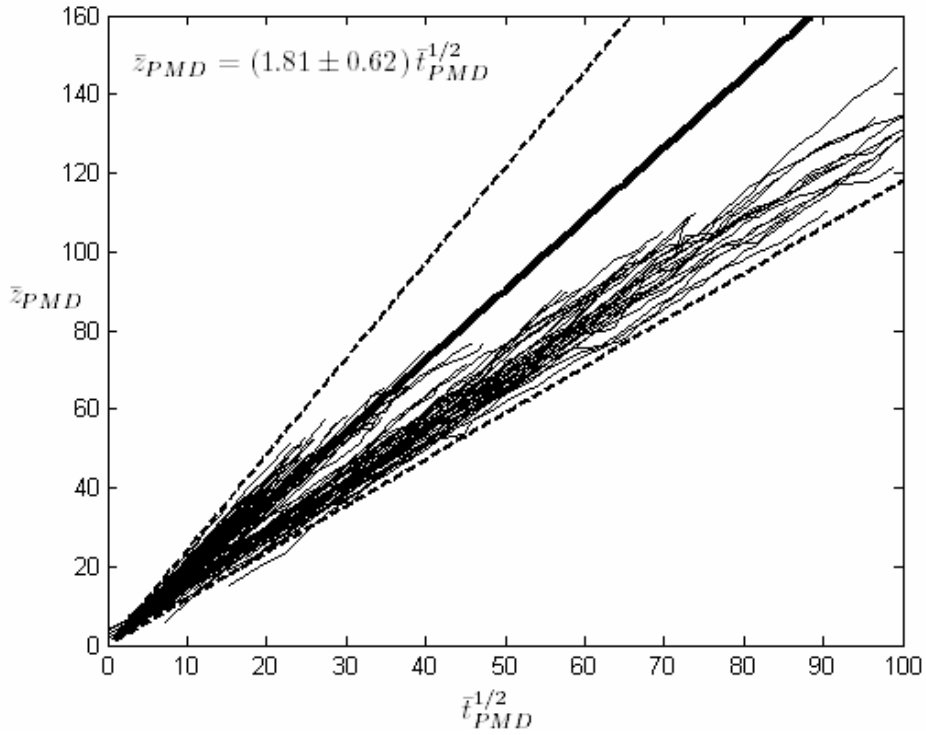

Figure 5.20. Normalized penetration as a function of the square root of the normalized time using PMD properties for the three-hole injector, includes all choked hydrogen and helium injection data.

The same two subsets again appear in the data where the data collapses more tightly. The first subset is for runs with a nozzle exit to chamber pressure ratio above three, $P_n/P_{ch} >$ 3.0, and is shown in Fig. 5.21. The collapse of the slopes in this subset is within ±15.4%. The second subset is shown in Fig. 5.22 and is for conditions with a nozzle exit to chamber pressure ration less than three, $P_n/P_{ch} <$ 3.0. The slopes of this subset collapse within 13.4%. The mean slopes and confidence intervals for these data sets are provided in their respective plots.

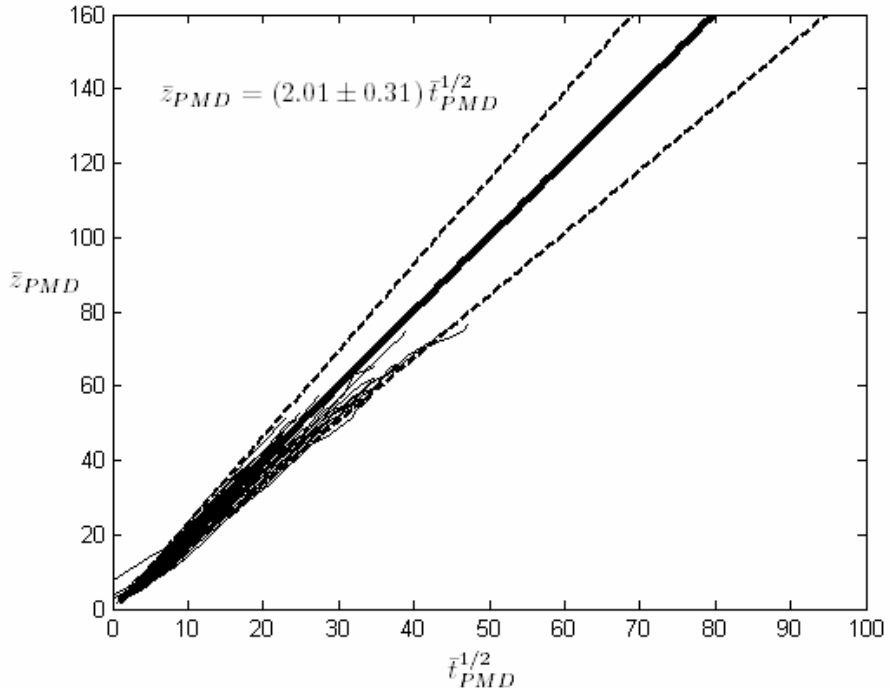

Figure 5.21. Normalized penetration as a function of the square root of the normalized time using PMD properties for the three-hole injector, $P_n/P_{ch} > 3.0$.

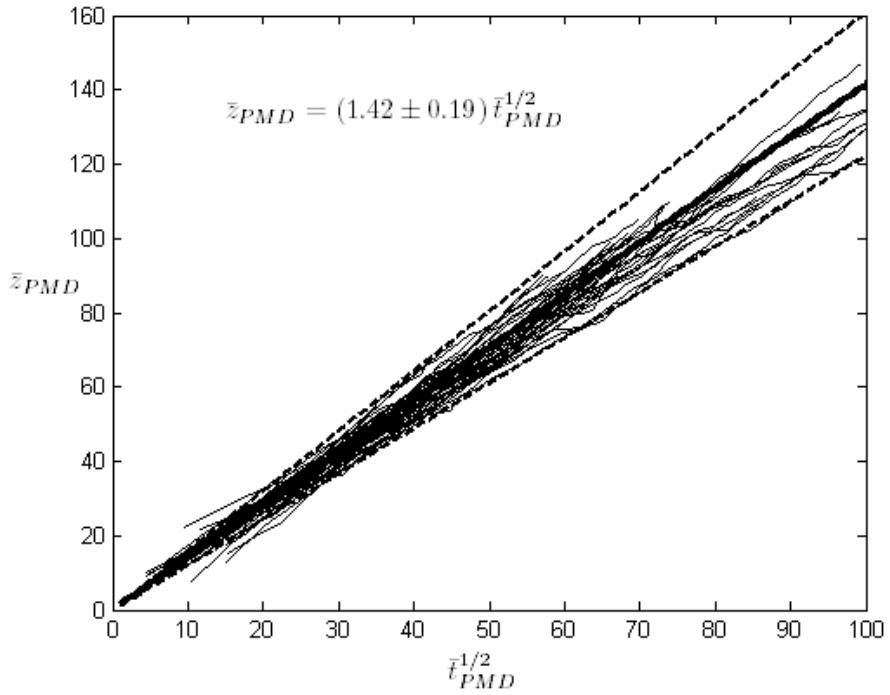

Figure 5.22. Normalized penetration as a function of the square root of the normalized time using PMD properties for the three-hole injector, $P_n/P_{ch} < 3.0$.

5.3.2.2.2 Seven-hole Injector

All of the data from the seven-hole injector normalized with the PMD parameters are shown in Figs. 5.23. The slopes collapse within ±18.0% for the entire set, compared to ±14.5% for the nozzle exit normalization. The data from conditions with an exit to chamber pressure ratio above 1.7, $P_n/P_{ch} > 1.7$, again lie to the left of the data with a pressure ratio below 1.7, $P_n/P_{ch} < 1.7$. Figures 5.24 and 5.25 show these data subsets with corresponding slope statistics.

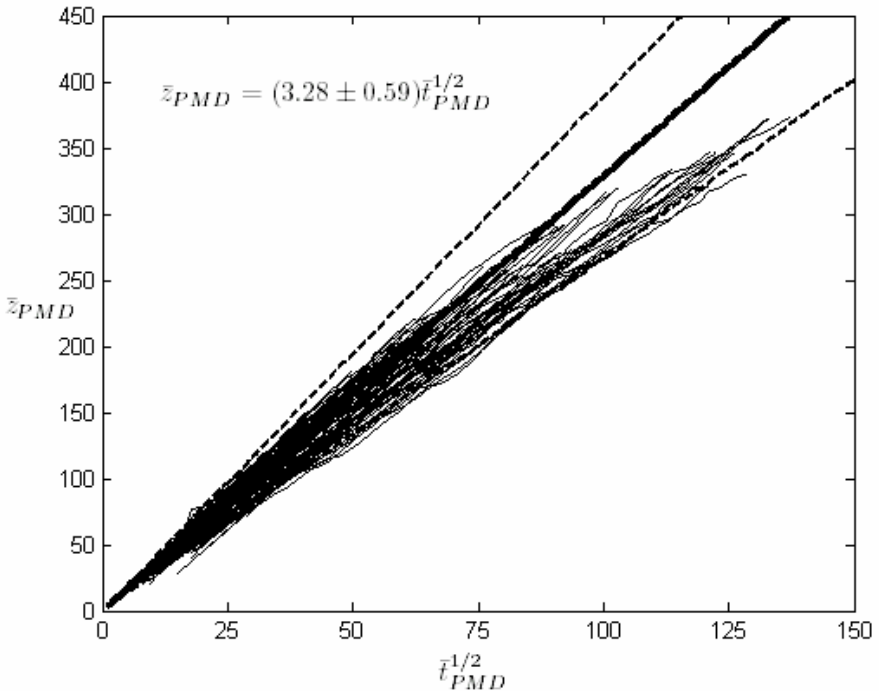

Figure 5.23. Normalized penetration as a function of the square root of the normalized time using PMD properties for the seven-hole injector, includes all choked hydrogen and helium injection data.

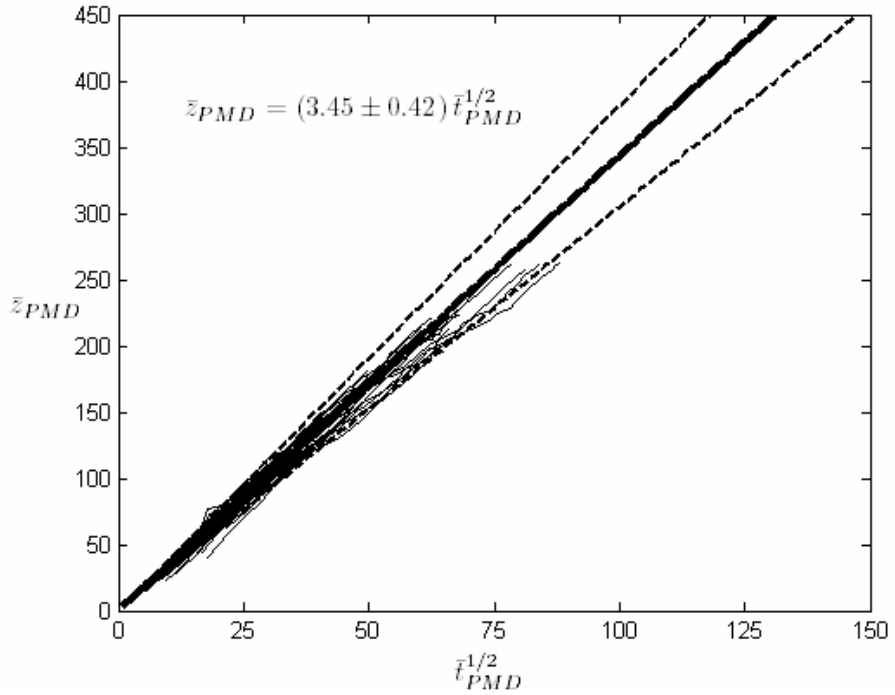

Figure 5.24. Normalized penetration as a function of the square root of the normalized time using PMD properties for the seven-hole injector, $P_n/P_{ch} > 1.7$.

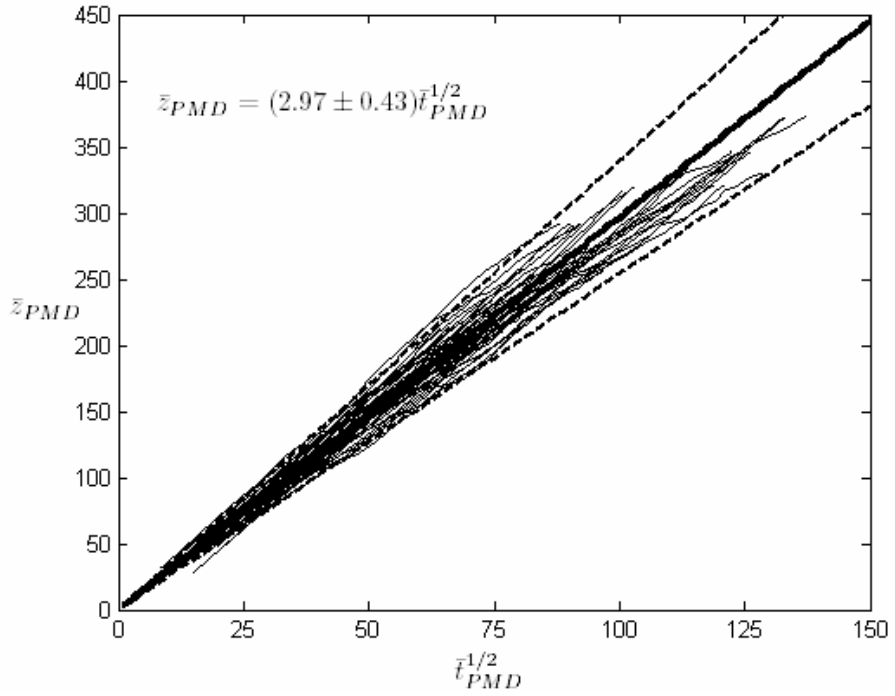

Figure 5.25. Normalized penetration as a function of the square root of the normalized time using PMD properties for the seven-hole injector, $P_n/P_{ch} < 1.7$.

5.3.2.3 Normalization via Nozzle Parameters with Jet Angle

Naber and Siebers [25] found that the inclusion of variation in jet angle, θ, in the characteristic length and time scales more completely collapsed their data and was consistent with an integral control volume model of a transient jet. The spray or jet angle, θ, incorporates the change in the amount of entrained mass for differing nozzle exit to chamber density ratios, and was found to increase with increasing ambient chamber density. The corresponding characteristic scales were presented in eqs. (5.2) and (5.3) and include nozzle exit properties and the jet angle. It should be noted that the discharge coefficient, C_d, used by Naber and Siebers [25] to determine the effective nozzle diameter, d_f, is assumed to be 1.0 in this section, while the effects of the discharge coefficient will be investigated later in this chapter.

5.3.2.3.1 Jet Angle Measurements

Figures 5.26 and 5.27 show the transient jet angle measurements associated with the iterative method of penetration measurement from the seven-hole injector for several runs with a chamber density of ρ_{ch} = 8.17 kg/m^3 and a stagnation injection pressures of P_0 = 70 bar and P_0 = 35.5 bar respectively. The jet angle, θ, is higher at early times due to the development of the head vortex and then drops to a relatively steady value. It should be noted that these are examples of the best cases.

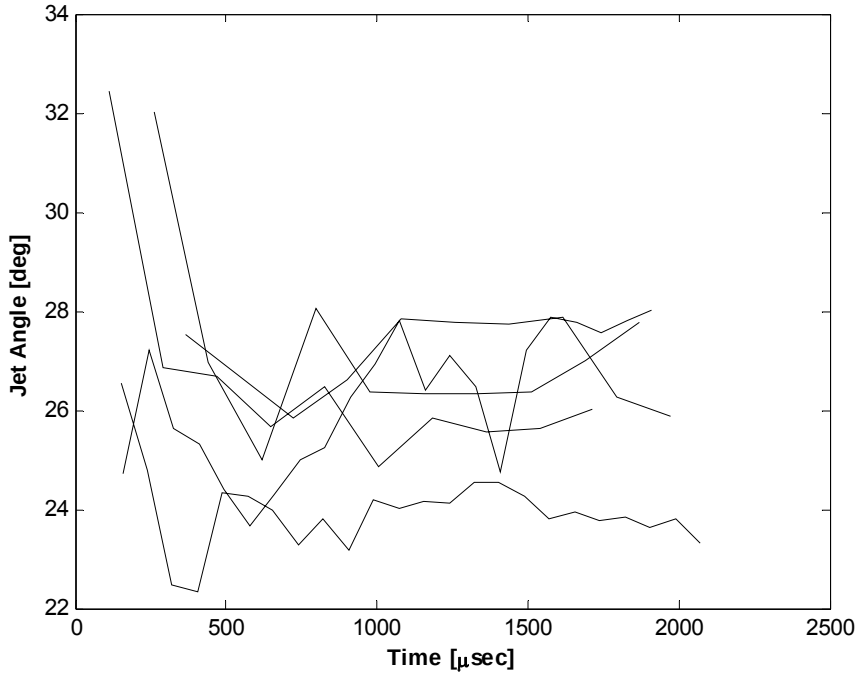

Figure 5.26. Jet angle as a function of time from seven-hole injector, P_0 = 70 bar (hydrogen), ρ_{ch} = 8.17 kg/m^3 (nitrogen).

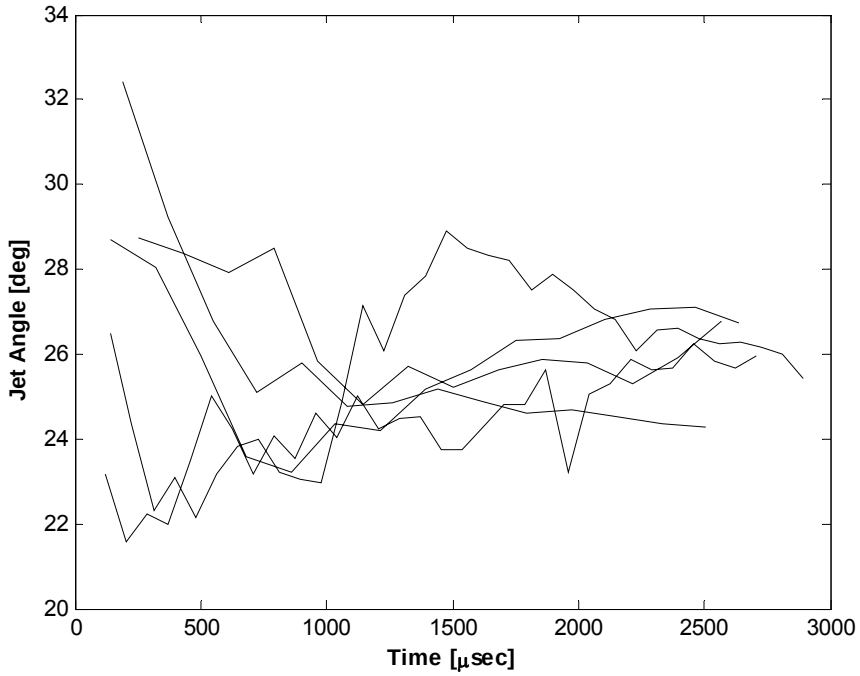

Figure 5.27. Jet angle as a function of time from seven-hole injector, P_0 = 35.5 bar (hydrogen), ρ_{ch} = 8.17 kg/m^3 (nitrogen).

The transient jet angle measurements show a significant amount of scatter and inconsistencies between individual runs of the same condition. For a majority of cases it is impossible to identify a single, steady-state value of jet angle. Upon further inspection, these transient jet angle measurements are not representative of the actual angle due to the method of isolating the jet from the background in each image. The edge-detection algorithm within Matlab and subsequent processing does not properly identify the outline of the jet and, thus, the measured jet angle is not representative of the actual jet angle. Also, the high sensitivity associated with the schlieren system may be affecting the outer edges of the jet that are imaged.

An additional algorithm was developed to more properly isolate the jet by using a threshold range to create a binary image. First, the background correction factor, S_c, from eq. (3.1) was increased to 1000 to provide a greater range of pixel intensities within each image. Pixels with an intensity between 100 and 156 were set to zero, while the remaining pixel locations were set to 1, creating a binary image. This range of intensities represents the pixels that have changed the least from the original background image and are most likely not within the jet. An example of the resulting binary jet image is shown in Fig. 5.28. As shown in Fig. 5.28 by the region between the white lines, the jet angle measurement was made in a section of the jet away from the nozzle exit and before the head vortex.

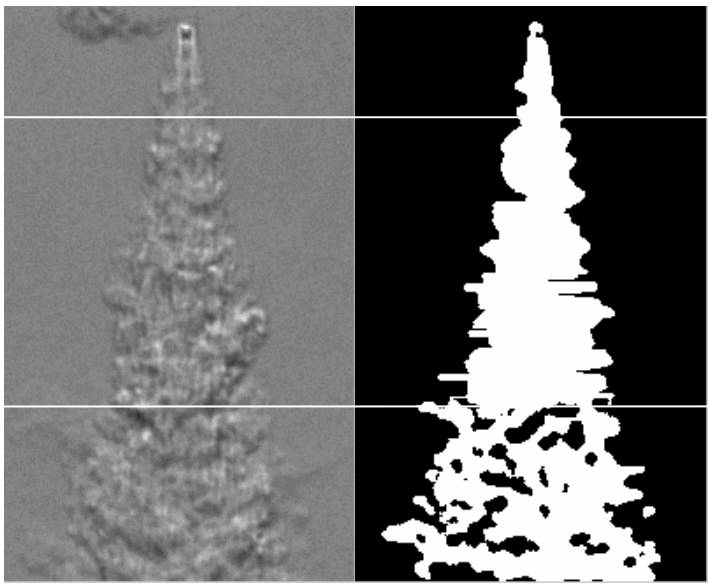

Figure 5.28. Example of jet isolation using threshold range.

Finally, the angles from ten jet images from the same run were averaged to determine a representative jet angle value. The ten images were taken from times when the jet tip was out of the field of view, and away from the transient portions of the injection. Note that the measurements made for the three-hole injector were only done on the right-most half of the jet. This was done to avoid the adjacent jet that occasionally is prominent in the images. Example images displaying the jet angle measurements for both injectors are provided in Appendix A.2. The averaged jet angles from the three- and seven-hole injectors are presented in Figs. 5.29 and 5.30 as a function of nozzle exit to chamber pressure ratio. The error bar indicated in each plot represents the 95% confidence interval in the mean value from the ten averaged images. These steady state jet angle values also show a lot of scatter in runs of the same condition and the power law fits to the data have a completely opposite trend with respect to P_n/P_{ch} for the three- and seven-hole injectors.

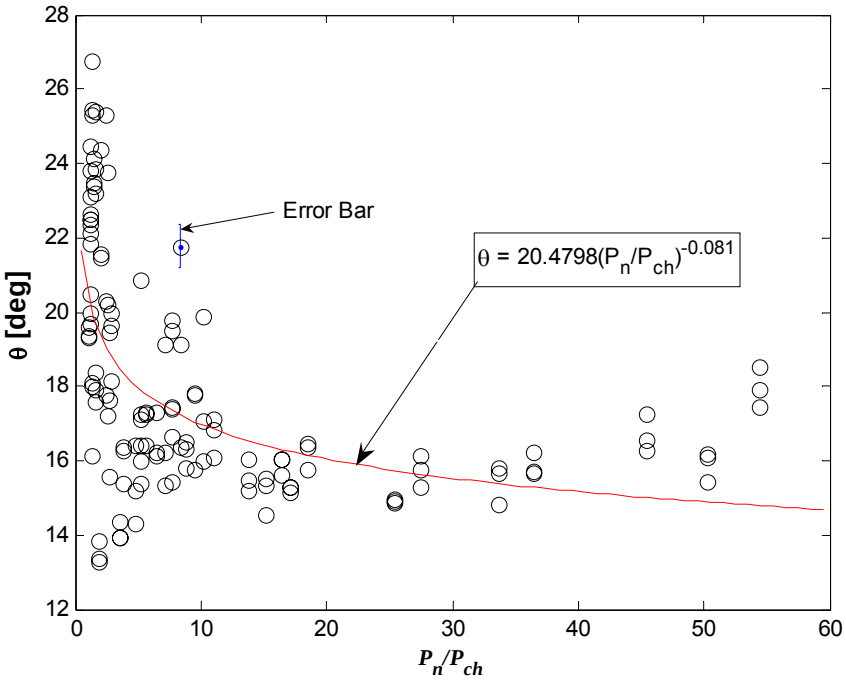

Figure 5.29. Averaged jet angle as a function of nozzle exit to chamber pressure ratio from three-hole injector.

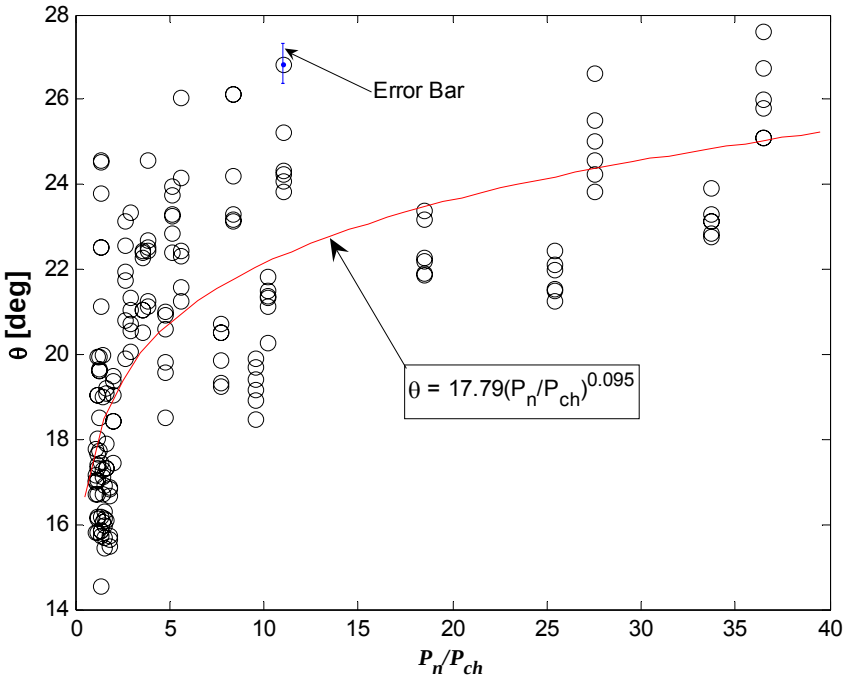

Figure 5.30. Averaged jet angle as a function of nozzle exit to chamber pressure ratio from seven-hole injector.

Although, the jet angle measurements provided in Appendix A.2 appear to be good approximations to the actual jet angle value, the significant scatter and strange trends in the data raise doubt in the accuracy of the measurements. The source of the scatter may not be the measurement technique but instead the nature of the schlieren optical system. The high sensitivity of the system used allows extraneous clouds (example in Fig. 5.31) of injected gas that are detached from the main jet to be imaged. The detached gas separates during the initial development stages of the jet, drifts into the ambient fluid, and is occasionally re-entrained by the jet. The clouds consist of the injected jet fluid but do not undergo the same physics as the main jet and, thus, should not be identified as part of the main jet body. These clouds are ultimately incorporated in the jet angle measurement, artificially increasing the jet angle value for images with these cloud-like structures present.

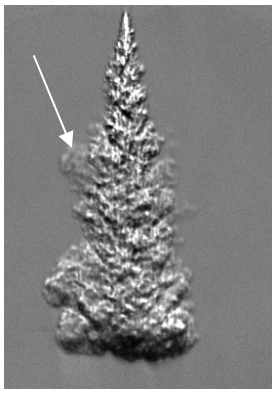

Figure 5.31. Example of extraneous clouds in jet flow field.

5.3.2.3.2 Normalized Data

The penetration data from the three- and seven-hole injectors recast in the nondimensional variables developed from nozzle exit properties that include the variation of the jet angle, e.g eqs. 5.2 and 5.3 combined with eqs. 5.4-5.7 are presented in Figs. 5.32 and 5.33.

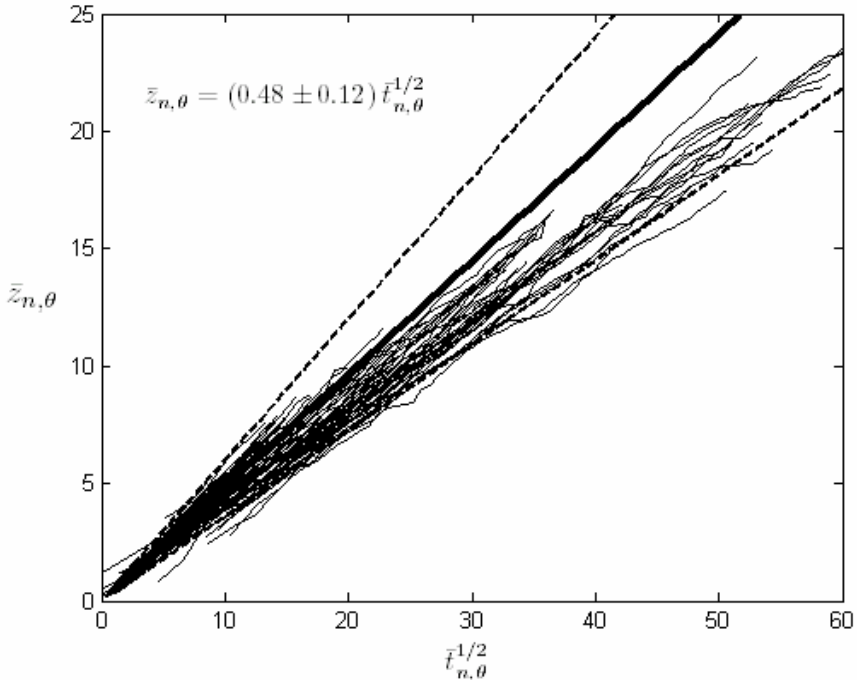

Figure 5.32. Normalized penetration as a function of the square root of the normalized time using nozzle properties and jet angle, θ, variation for the three-hole injector, includes all choked hydrogen and helium injection data.

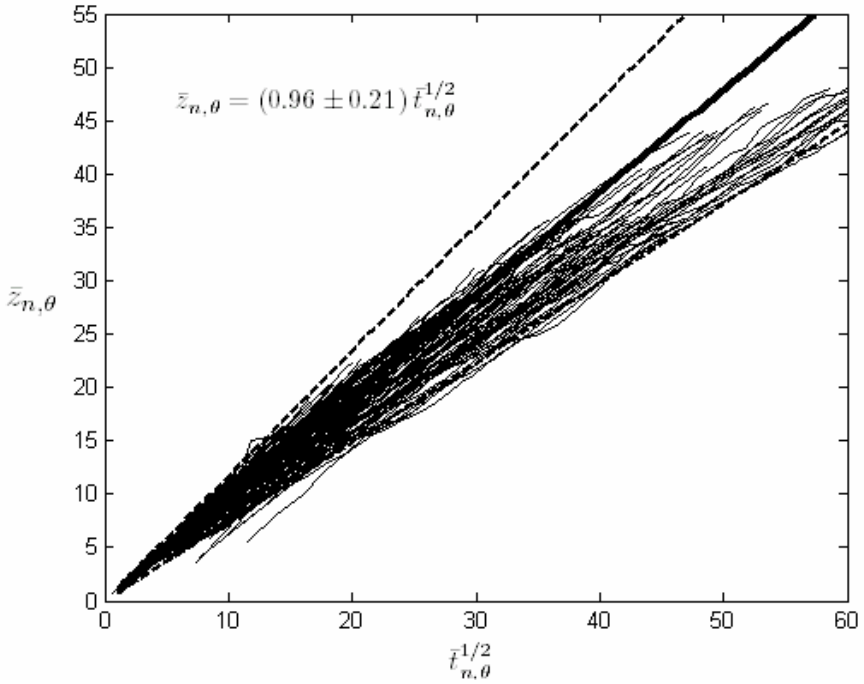

Figure 5.33. Normalized penetration as a function of the square root of the normalized time using nozzle properties and jet angle, θ, variation for the seven-hole injector, includes all choked hydrogen and helium injection data.

The collapse of the slopes for the three-hole injector data is ±25.0% compared to ±31.4% when the jet angle variation was not incorporated. This indicates that incorporating the jet angle variation does further collapse the normalized penetration rate data for the three-hole injector. Contrarily, the collapse of the slopes for the seven-hole injector is ±21.9% when the jet angle variation is included and ±14.5% when it was not, indicating the jet angle variation does not collapse the data better for the seven-hole injector. This contradiction between the three- and seven-hole injectors can mainly be attributed to the unreliable jet angle measurements. The opposing jet angle trends seen between the two injectors and the inability to make good jet angle measurements make it impossible to properly access the effectiveness of the scaling parameters that utilize jet angle variation to collapse the data.

5.3.2.3 Normalization via PMD Parameters with Jet Angle

The normalization method involving a combination of the jet angle used in the integral momentum conservation model with the PMD model of an underexpanded jet was also investigated. It incorporates the expansion and pressure variation outside of the nozzle exit by utilizing the PMD properties and also includes the additional mass entrained by jets with larger values of θ at higher nozzle exit to chamber density ratios. A similar model was previously used by Tsujimura *et al.*[36]. The characteristic time and length scales and corresponding nondimensional penetration and time used in this model are given in eqs. (5.14) and (5.15).

$$\overline{z}_{PMD,\theta} \equiv \frac{Z_t}{z^+_{PMD,\theta}} \quad ; \quad z^+_{PMD,\theta} = \frac{d_{PMD}\sqrt{\rho_{PMD}/\rho_{ch}}}{a\tan(\theta/2)} \tag{5.14}$$

$$\overline{t}_{PMD,\theta} \equiv \frac{t}{t^+_{PMD,\theta}} \quad ; \quad t^+_{PMD,\theta} = \frac{d_{PMD}\sqrt{\rho_{PMD}/\rho_{ch}}}{a\tan(\theta/2)u_{PMD}} \tag{5.15}$$

The data collected in this study recast in these nondimensional variables for all of the hydrogen and helium data under choked nozzle exit conditions are presented in Figs. 5.34 and 5.35 for the three- and seven-hole injectors respectively.

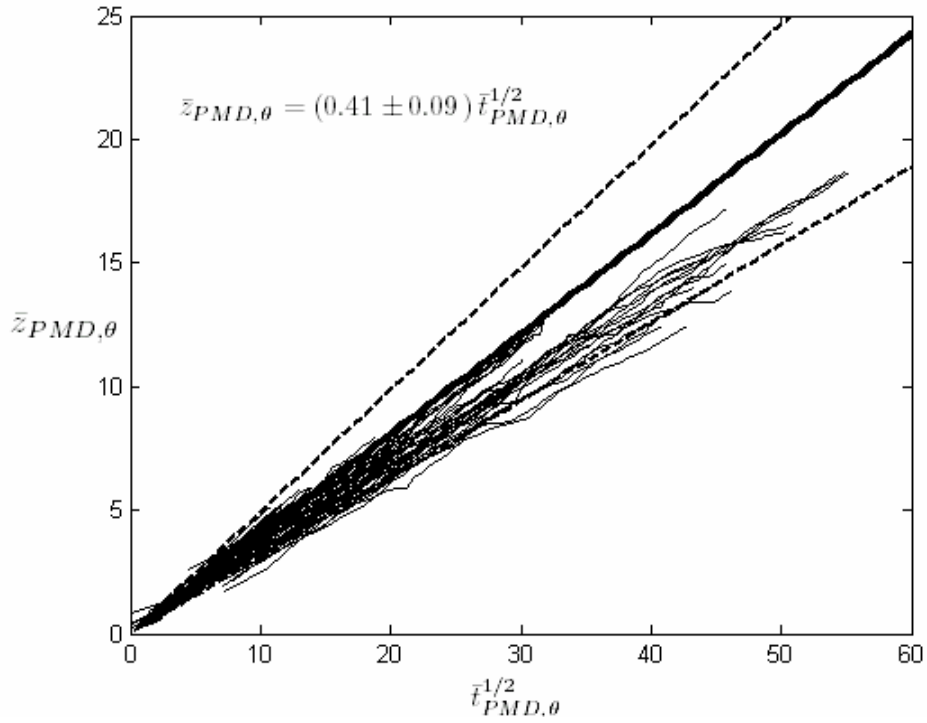

Figure 5.34. Normalized penetration as a function of the square root of the normalized time using PMD properties and jet angle, θ, variation for the three-hole injector, includes all choked hydrogen and helium injection data.

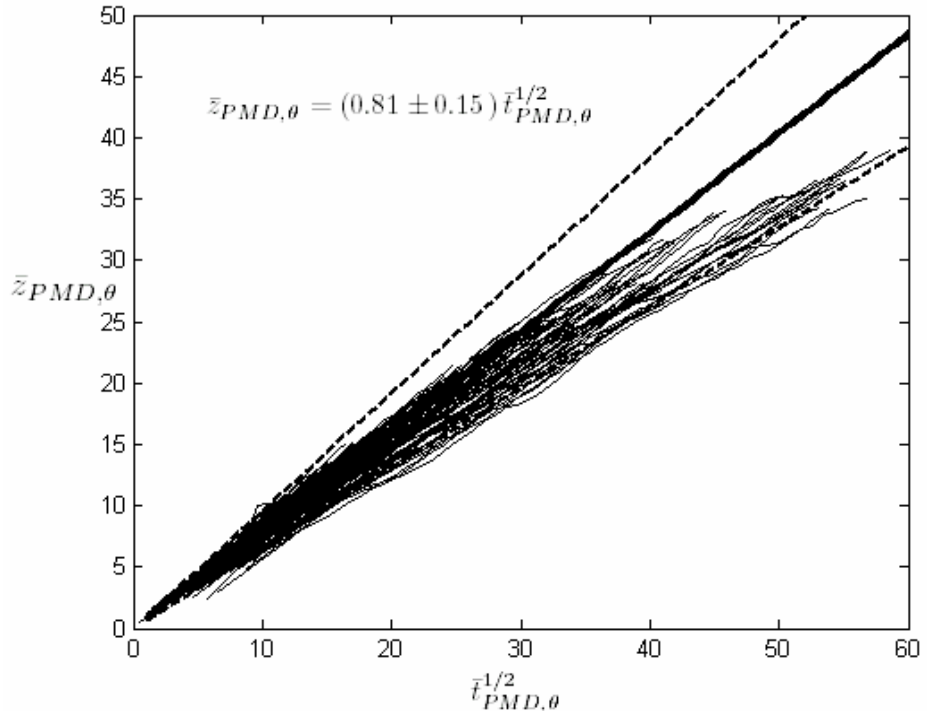

Figure 5.35. Normalized penetration as a function of the square root of the normalized time using PMD properties and jet angle, θ, variation for the seven-hole injector, includes all choked hydrogen and helium injection data.

The collapse of the data is slightly better relative to the collapse seen with the nozzle exit parameter normalization that includes the jet angle, θ. The data for the three-hole injector collapses within ±21.9%, compared to ±25.0% when the jet angle variation is used with the nozzle exit parameters. Also, the seven-hole injector data collapses within ±18.5%, reducing from ±25.3% for the nozzle exit-θ normalization scheme. Again, the highly variable jet angle measurements do not allow any conclusions on these scaling relationships, because of the inclusion of the jet angle.

5.3.3.3 Injector Characteristic Measurements

Two injector characteristics were determined in order to quantify the performance of the prototype injectors and investigate their importance on the nondimensionalization of the penetration rate data. First the discharge coefficient was measured to characterize the effect of non-ideal processes at the nozzle exit. Secondly, the mass flow rate as a function of time, the rate shape, was measured to investigate the transient behavior of each injector.

5.3.3.3.1 Discharge Coefficient

The discharge coefficient of a nozzle, C_d, can be broken down into two components, an area contraction coefficient, C_a, and a velocity coefficient, C_v, as shown in eq. (5.16) [25].

$$C_d = C_a C_v \tag{5.16}$$

The area contraction coefficient, C_a, accounts for the non-uniform velocity profile at the nozzle exit that is assumed in the ideal mass flow rate calculation and the velocity coefficient, C_v, accounts for non-ideal processes that affect the exit velocity of the flow. The data analyzed here will be for conditions where the flow is choked at the nozzle exit.

Therefore, C_v was assumed to hold a value of one since the exit velocity is necessarily the speed of sound at the exit temperature. The discharge coefficient is then equal to the area contraction coefficient, C_a, i.e. $C_d = C_a$.

The discharge coefficients measured for the four injectors are shown in Figs. 5.36 through 5.39. The values varied from approximately 0.28 to 0.33 for the seven- and thirteen-hole injectors and 0.19 to 0.22 for the three- and nine-hole injectors. The discharge coefficient also increased with increasing nozzle exit to chamber pressure ratio and, therefore, Reynolds number. The low values could be caused from the injector being choked at both the nozzle exit and also somewhere upstream of the exit.

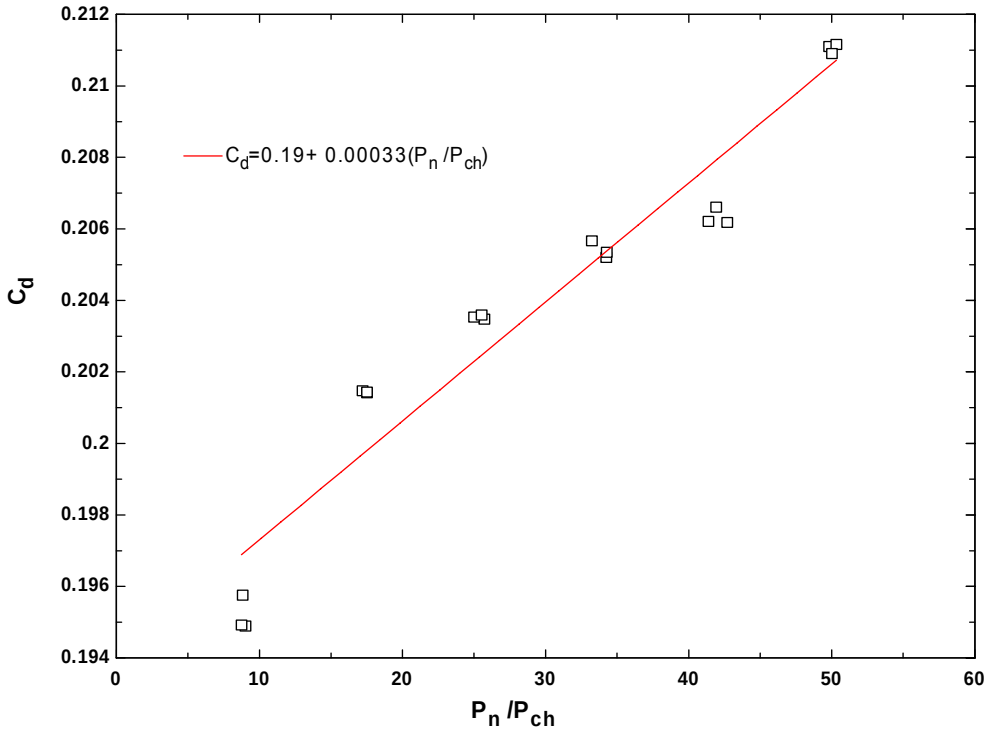

Figure 5.36. Discharge coefficient as a function of nozzle exit to chamber pressure ratio for three-hole injector.

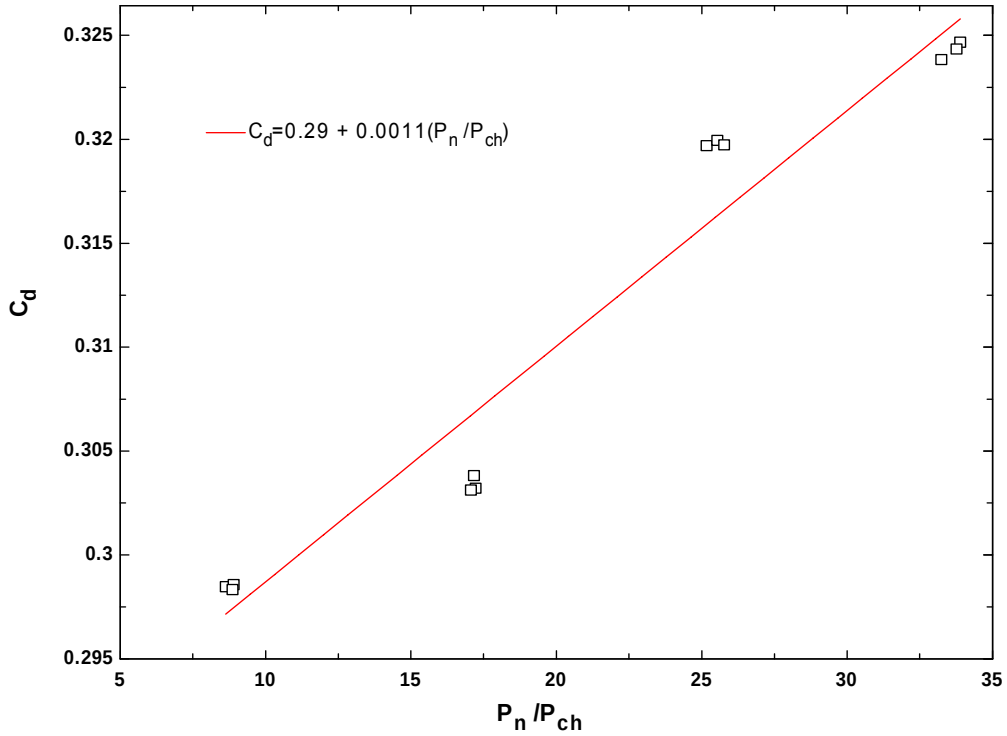

Figure 5.37. Discharge coefficient as a function of nozzle exit to chamber pressure ratio for seven-hole injector.

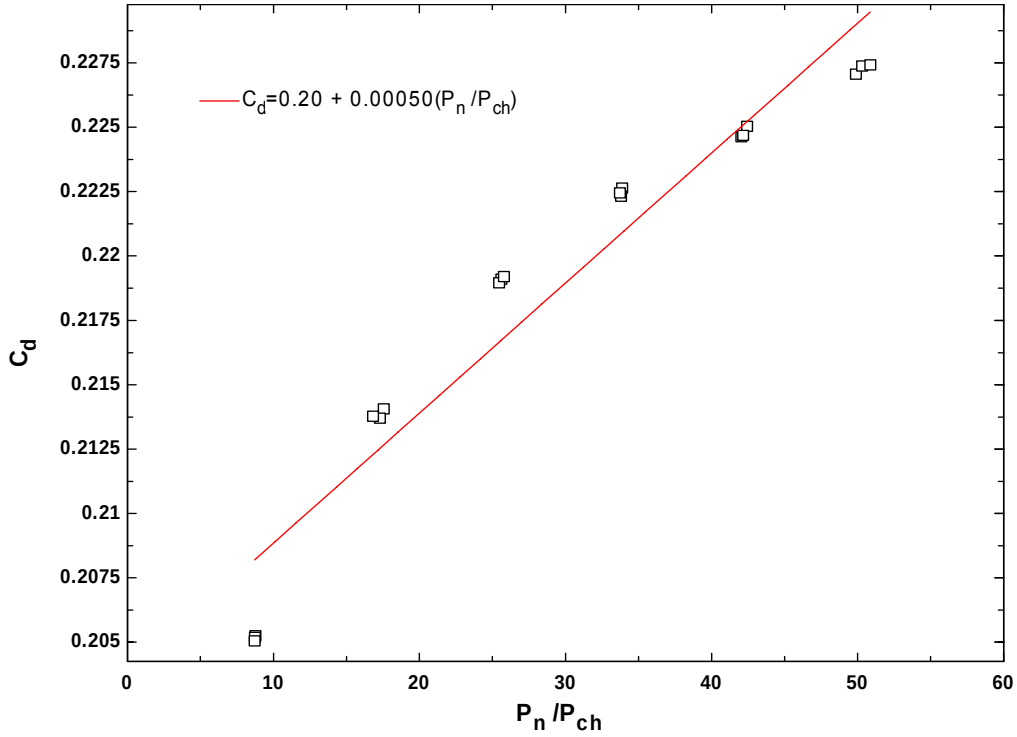

Figure 5.38. Discharge coefficient as a function of nozzle exit to chamber pressure ratio for nine-hole injector.

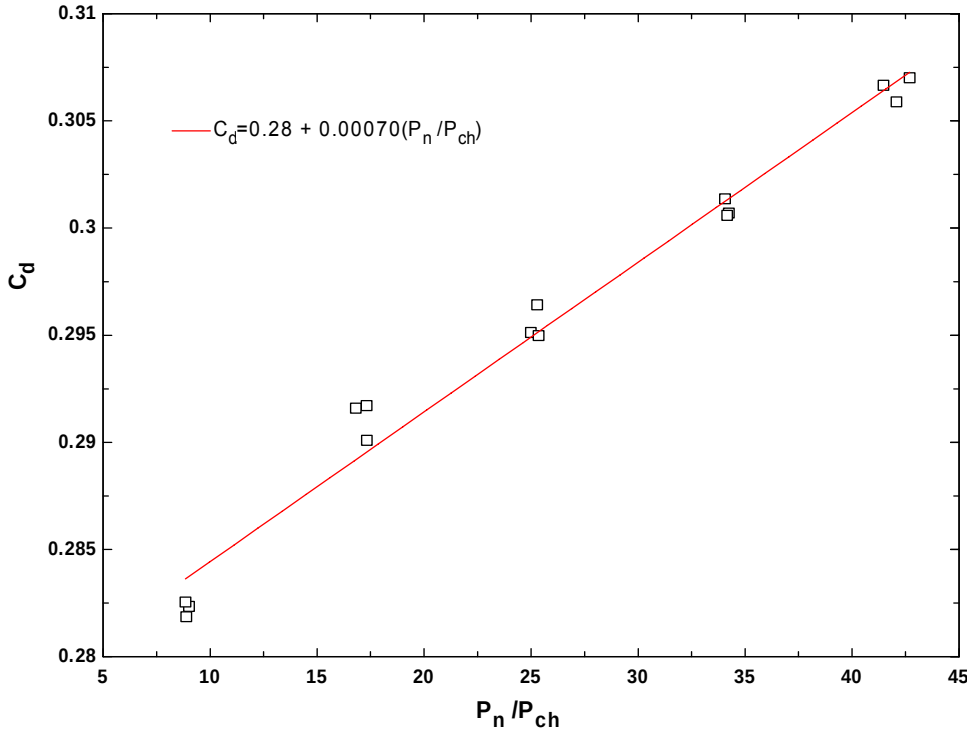

Figure 5.39. Discharge coefficient as a function of nozzle exit to chamber pressure ratio for thirteen-hole injector.

5.3.3.3.2 Data Normalization – Nozzle Exit Properties, Jet Angle, and Discharge Coefficient

Naber and Siebers [25] then utilized the area contraction coefficient to modify the nozzle diameter to develop an effective fuel diameter, d_f, shown in eq. (5.17).

$$d_f = \sqrt{C_a} d_n \tag{5.17}$$

This effective diameter replaced the nozzle diameter in the nozzle exit normalization scheme that included jet angle variation effects. Figures 5.40 and 5.41 show the penetration rate data normalized with nozzle exit properties and the effective diameter, d_f.

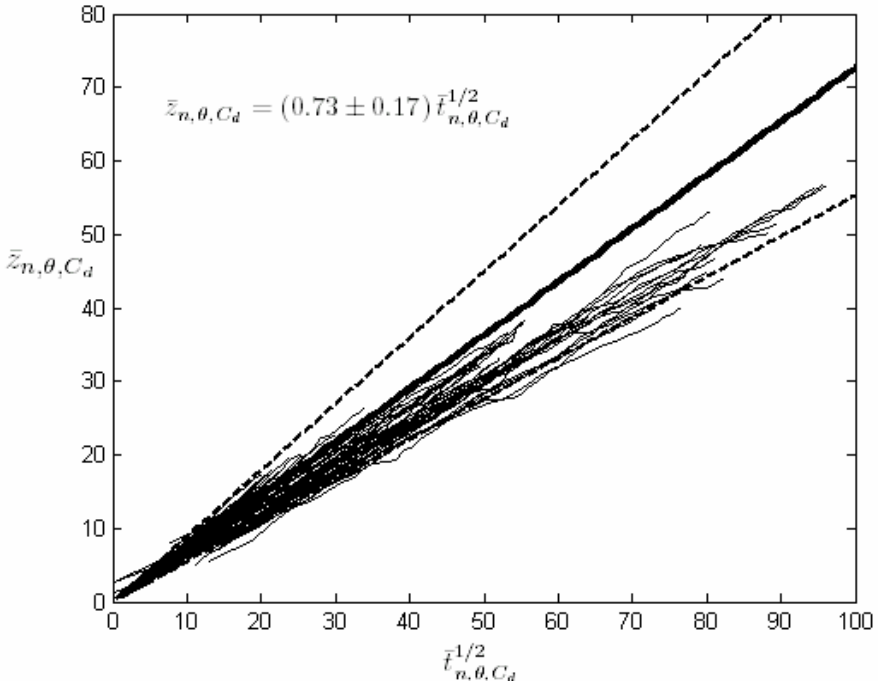

Figure 5.40. Normalized penetration as a function of the square root of the normalized time using nozzle properties, jet angle variation, and discharge coefficient, three-hole injector, includes all choked hydrogen and helium injection data.

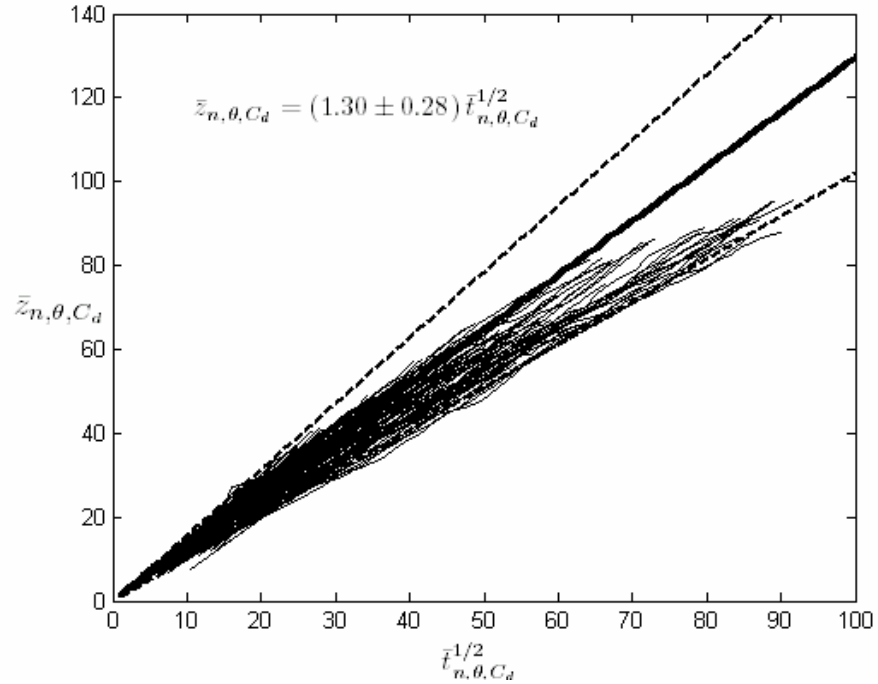

Figure 5.41. Normalized penetration as a function of the square root of the normalized time using nozzle properties, jet angle variation, and discharge coefficient, seven-hole injector, includes all choked hydrogen and helium injection data.

The three-hole data in Fig. 5.40 collapses within ±23.3%, which is slightly better than the ±25.0% when the discharge coefficient is ignored. The slopes of the seven-hole injector collapse to within ±21.2% of the mean slope, slightly better than the ±21.9% when the discharge coefficient is not incorporated into the analysis. Although the data collapse is similar for each injector, the main issue is that the mean slope for the three-hole injector remains to be almost a factor of two smaller than the mean slope of the seven-hole injector data.

5.3.3.3.3 Rate Shape

Finally, the rate shape was investigated to determine the transient behavior of each injector. Abnormal injector behavior, such as long opening and closing times, can show up in the rate shape and possibly give clues on differences in penetration behavior between different injectors or even different conditions.

The pressure as a function of time during injection was initially measured with a Kistler 7061 piezoelectric transducer attached directly to the constant volume chamber. The resulting pressure trace from a 3 ms injection of helium with a stagnation injection pressure, P_0, of 104 bar and a helium chamber density, ρ_{ch}, of 0.16 kg/m^3 is shown in Fig. 5.42.

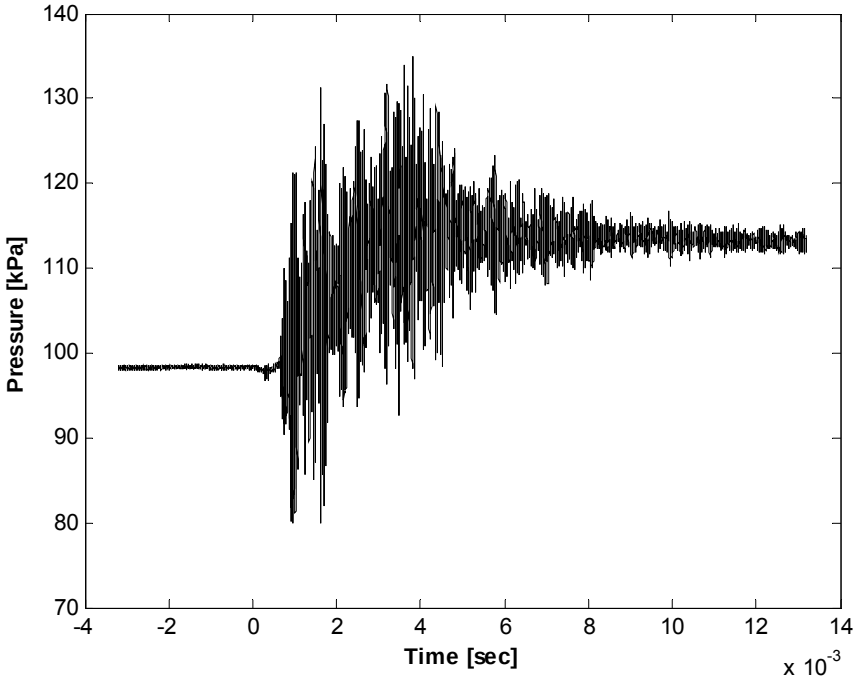

Figure 5.42. Pressure trace during an injection of P_0 = 104 bar (helium) into ρ_{ch} = 0.16 kg/m^3 (helium), with Kistler 7061 piezoelectric transducer directly attached to chamber.

A significant amount of high-amplitude noise is clearly present throughout the injection duration and almost entirely obscures the actual pressure trace. An FFT analysis was performed on the pressure data to investigate the frequency of the noise. Figure 5.43 shows that a frequency of approximately 48 kHz is prevalent within the data. The natural frequency of the Kistler 7061 transducer is reported as approximately 45 kHz and, therefore, the noise within the pressure trace was assumed to be oscillation at the transducer's natural frequency excited by the injector. It should be noted that various tests were performed to eliminate electronic processes as the source of the noise.

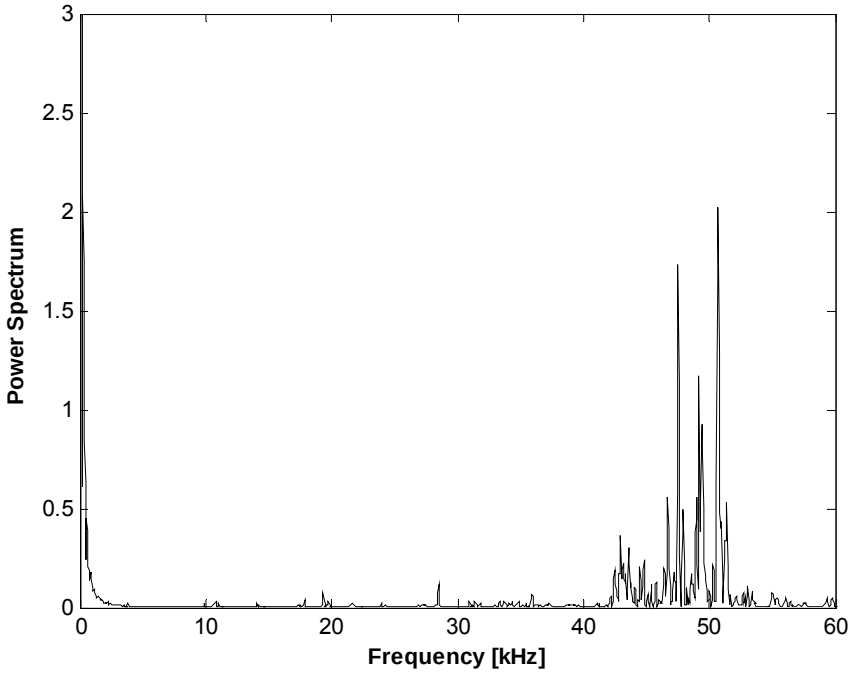

Figure 5.43. Power spectrum from FFT of pressure data with piezo-electric transducer directly attached to chamber.

An 80 mm section of Teflon tubing was then added as a flexible chamber-to-transducer linkage. This additional tubing was added in order to damp out the 48 kHz ringing. A pressure trace and corresponding FFT from a 3 ms helium injection with a stagnation injection pressure, $P_{0,}$ of 104 bar and a helium chamber density, $\rho_{ch,}$ of 0.16 kg/m^3 are shown in Figs. 5.44 and 5.45.

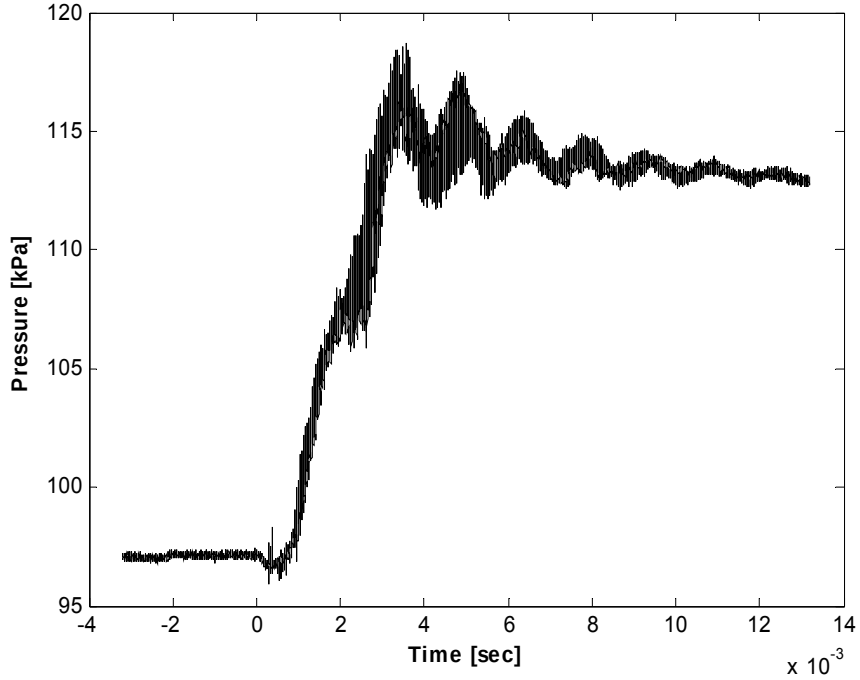

Figure 5.44. Pressure trace during an injection of P_0 = 104 bar (helium) into ρ_{ch} = 0.16 kg/m^3 (helium), with Kistler 7061 piezoelectric attached to chamber with 80 mm of Teflon tubing.

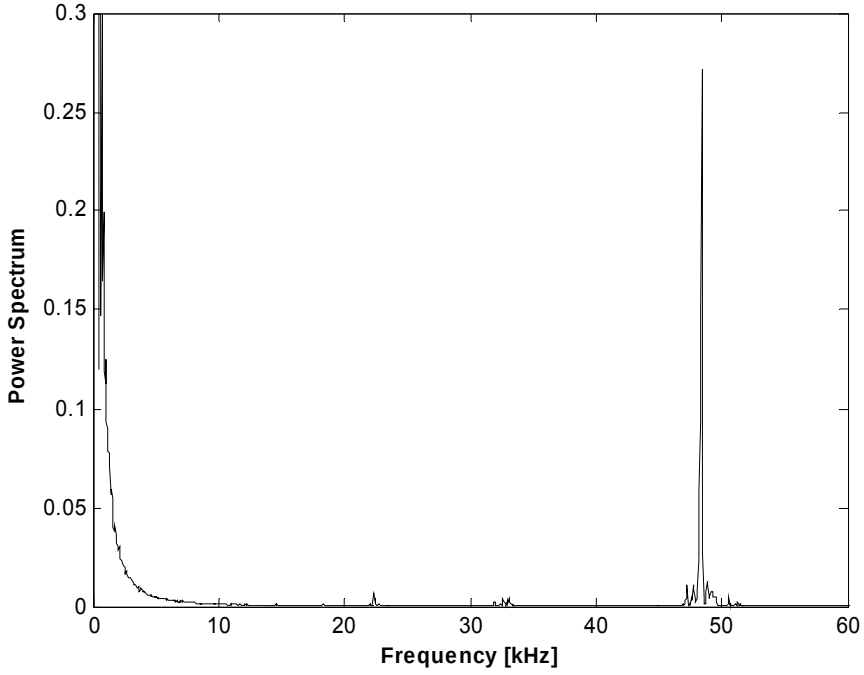

Figure 5.45. Power spectrum from FFT of pressure data with piezoelectric transducer attached to chamber with 80 mm of Teflon tubing.

Figure 5.45 shows that the 48 kHz vibration has been damped down to a lower magnitude, but is still prevalent within the pressure data. Another frequency of approximately 0.5 kHz is introduced into the pressure measurement with the addition of the tubing. Finally, an additional 1 m of Teflon tubing was added to the transducer linkage to further damp the vibration caused by the injection. Figures 5.46 and 5.47 show the resulting pressure trace and FFT from an injection with the same conditions as the previous two setups.

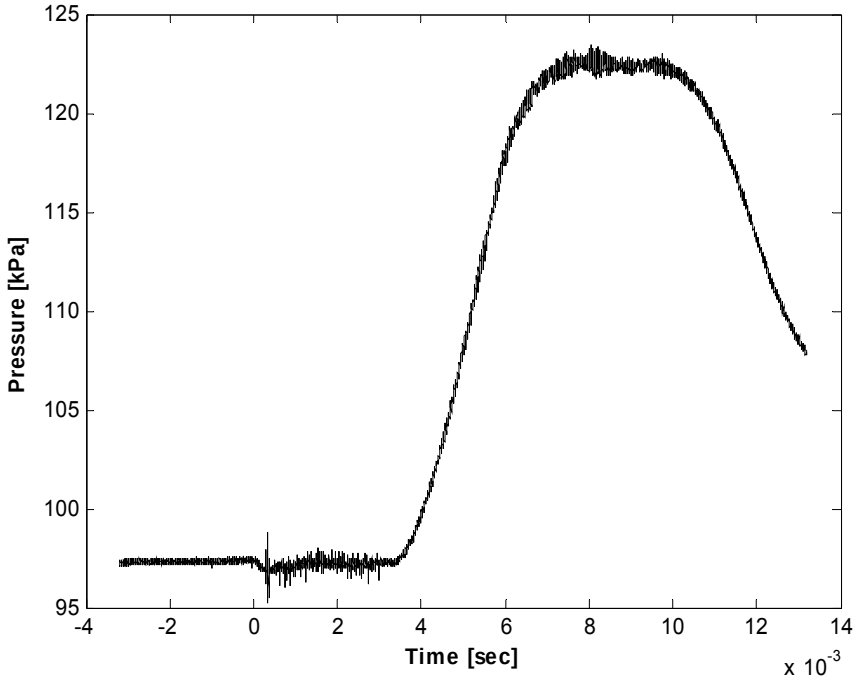

Figure 5.46. Pressure trace during an injection of P_0 = 104 bar (helium) into ρ_{ch} = 0.16 kg/m^3 (helium), with Kistler 7061 piezoelectric attached to chamber with 1 m of Teflon tubing.

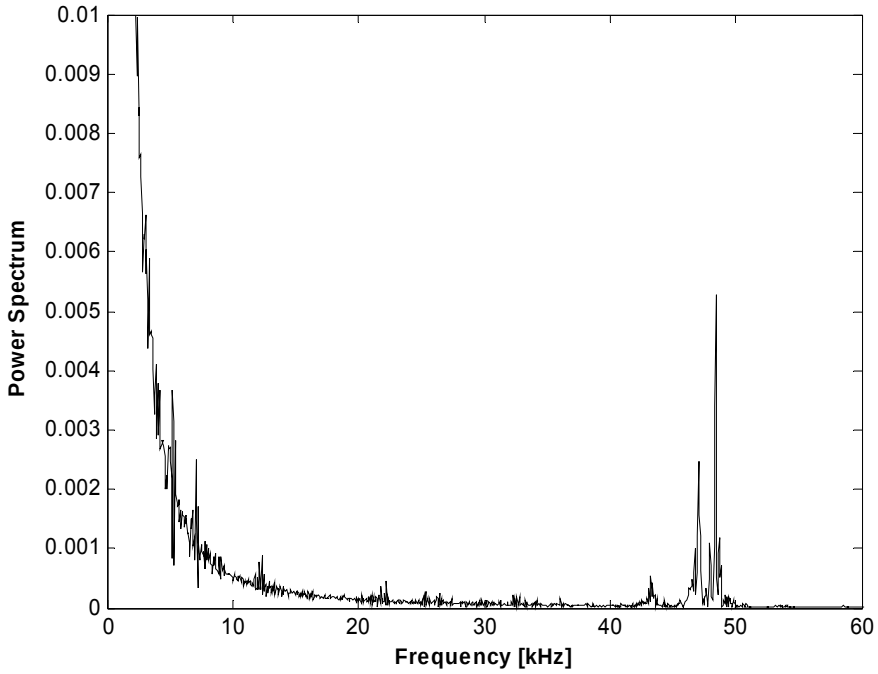

Figure 5.47. Power spectrum from FFT of pressure data with piezoelectric transducer attached to chamber with 1 m of Teflon tubing.

The 48 kHz frequency is further damped with the additional tubing, but two additional issues arise. First, the pressure rise is delayed approximately 4 ms from the start of injection (near time zero), with the entire injection ending after 3 ms. Secondly, a significant pressure drop occurs approximately 7 ms after the injection has ended. The absolute pressure was measured and found to remain constant after injection, ensuring that the chamber did not have any leakage issues.

Although the addition of a flexible linkage between the chamber and the transducer did reduce the magnitude of the 48 kHz vibration from the injector, the additional anomalies introduced into the pressure trace (additional noise frequencies, delay, pressure drop) are unwarranted and ultimately obscure the mass flow rate calculation. Therefore, the initial pressure trace obtained with the transducer attached directly to the chamber was utilized in conjuction with several filtering processes to

calculate the rate shape. First, a Fourier type filter was used to eliminate the high frequencies from the pressure data. The FFT values for frequencies above 5 kHz were set to zero to eliminate the high frequency noise and finally inverse transformed back to pressure data. The filtered pressure trace resulting from the original data is shown in Fig. 5.48.

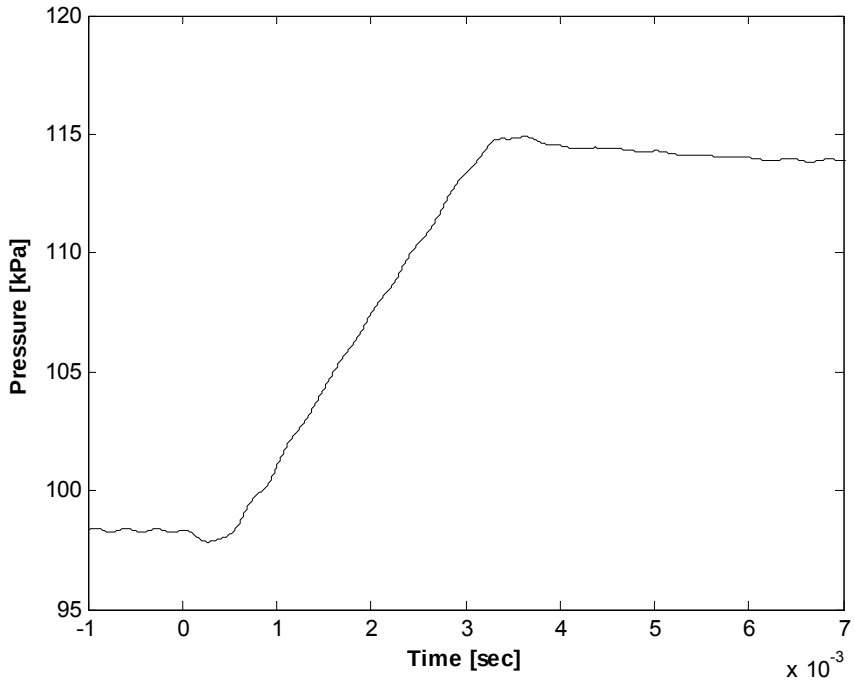

Figure 5.48. Filtered pressure trace, 5 kHz Fourier filter.

A de-noising function within Matlab was further used to smooth the pressure trace and the rate shape of each injector was calculated for a wide range of injection pressures. An example of the rate shape calculated for the nine-hole injector is shown in Fig. 5.49. The rate shape measurement still contains oscillations due to the remaining small amplitude frequencies in the pressure trace.

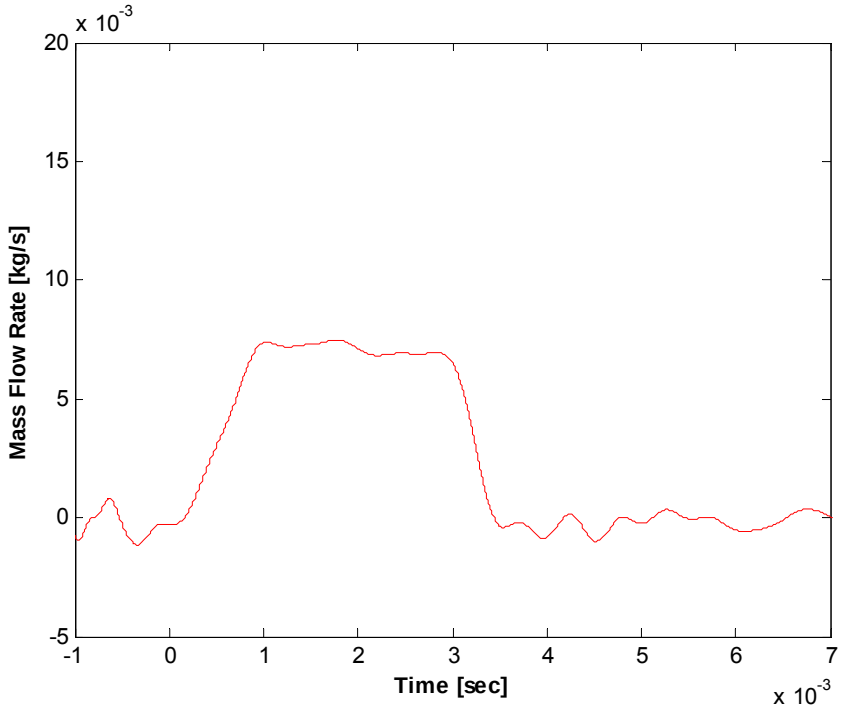

Figure 5.49. Rate shape for nine-hole injector P_0 = 104 bar (helium), ρ_{ch} = 0.16 kg/m^3 (helium).

Although the pressure trace needed to be extensively filtered in order to calculate a noisy rate shape, the main goal of investigating the transient behavior of the injector was accomplished. The filtered pressure trace shows no strange transient behavior at either the opening or closing of the injector. The flow appears to abruptly become choked, the chamber has a constant pressure rise rate, and, therefore, the rate shape displays a "top hat" behavior. It should be noted that the same behavior was seen for all conditions tested for all four injectors. Therefore, differences in the jet tip penetration rate cannot be directly attributed to varying behavior of the rate shape between injectors or even conditions.

5.4 Summary

Five penetration rate normalization methods were presented in this chapter:

- **Nozzle Exit Parameters (*n*):** previously used with mainly incompressible jets, but has been extended to compressible, underexpanded jets [11,20,21,23]
- **PMD Parameters (*PMD*):** developed parameters from a mass- and momentum-conservation model, includes expansion outside of the nozzle exit and subsequent normal shock for choked, underexpanded jets.
- **Nozzle Parameters and Jet Angle (n,θ):** scaling parameters incorporate the angle of the initial quasi-steady jet region, corresponds to momentum control volume model presented by Naber and Siebers [25] neglecting effects of discharge coefficient, C_d.
- **PMD Parameters and Jet Angle (*PMD*, θ):** used by Tsujimura *et al.* [ref] to incorporate the effects of underexpansion and the increased mass entrainment.
- **Nozzle Parameters, Jet Angle, and Discharge Coefficient (n,θ, C_d):** full nondimensional parameters used by Naber and Siebers [25] including nozzle discharge coefficient effects.

A statistical summary of the penetration data under unchoked conditions normalized by the characteristic scales at the nozzle exit for the three- and seven-hole injector is provided in Table 1. The table includes the mean slope value of the individual curves, the 95% confidence interval in the mean slope value, and the relative confidence interval with respect to the mean slope. Tables 5.2 and 5.3 summarize the choked data sets and include the nozzle exit to chamber pressure ratio ranges the data were analyzed over and also the specific normalization method. Table 5.4 displays results from previous authors

that used the nozzle exit parameter scaling. It should be noted that these authors mainly investigated incompressible jets. Hill and Oulette [21] were the only ones to study underexpanded jets and determined that the slope of their data remained approximately 2.82. The results presented in all the tables are given as the slope, α, in the relationship:

$$\bar{z} = \alpha \bar{t}^{1/2} \tag{5.18}$$

where $\bar{z}$ is the nondimensional penetration and $\bar{t}$ is the nondimensional time corresponding to the particular normalization scheme of interest.

Table 5.1. Summary of normalization results from three- and seven-hole injectors, unchoked, subsonic conditions.

Injector	Slope (α)	95% Cofidence Interval	Relative Interval
3 Hole	1.27	$\pm$ 0.35	$\pm$ 27.6%
7 Hole	2.43	$\pm$ 0.29	$\pm$ 11.9%

Table 5.2. Summary of normalization results from three-hole injector, choked conditions.

Normalization Method	P_n/P_{ch}	Slope (α)	95% Confidence Interval	Relative Interval
Nozzle Exit Parameters (*n*)	All	2.26	$\pm$ 0.71	$\pm$ 31.4 %
	> 3.0	2.49	$\pm$ 0.36	$\pm$ 14.5 %
	< 3.0	1.82	$\pm$ 0.25	$\pm$ 13.7 %
Nozzle Exit and Jet Angle (n, θ)	All	0.48	$\pm$ 0.12	$\pm$ 25.0 %
PMD Parameters (*PMD*)	All	1.81	$\pm$ 0.62	$\pm$ 34.3 %
	> 3.0	2.01	$\pm$ 0.31	$\pm$ 15.4 %
	< 3.0	1.42	$\pm$ 0.19	$\pm$ 13.4 %
PMD and Jet Angle (PMD, θ)	All	0.41	$\pm$ 0.09	$\pm$ 21.9 %
Nozzle Exit, Jet Angle, C_d (n, θ, C_d)	All	0.73	$\pm$ 0.17	$\pm$ 23.3 %

Table 5.3. Summary of normalization results from seven-hole injector, choked conditions.

Normalization Method	P_n/P_{ch}	Slope (α)	95% Confidence Interval	Relative Interval
Nozzle Exit Parameters (*n*)	All	2.76	± 0.4	± 14.5%
	> 1.7	2.86	± 0.26	± 9.1%
	< 1.7	2.57	± 0.35	± 13.6%
Nozzle Exit and Jet Angle (n, θ)	All	0.96	± 0.21	± 21.9%
PMD Parameters (*PMD*)	All	3.281	± 0.59	± 18.0%
	> 1.7	3.45	± 0.42	± 12.2%
	< 1.7	2.97	± 0.43	± 14.5%
PMD and Jet Angle (PMD, θ)	All	0.81	± 0.15	± 18.5%
Nozzle Exit, Jet Angle, C_d (n, θ, C_d)	All	1.30	± 0.28	± 21.2 %

Table 5.4. Summary of previous results from various author using nozzle exit parameters.

Author(s)	Slope (α)
Hill and Oullete [21]	2.82
Johari [18]	2.14 - 2.58
Lahbabi [17]	2.9
Abraham (1994) [20]	2.5

A comparison between the results presented in these tables raises six main issues:

- When the nozzle exit parameters are used to scale the penetration results for subsonic, unchoked conditions, the slope between the square root of the nondimensional time, $\overline{t}_n^{1/2}$, and nondimensional penetration, $\overline{z}_n$, is approximately 1.27 for the three-hole injector and 2.43 for the seven-hole injector. The 1.27 ± 0.35 value determined for the three-hole injector is significantly lower than any of the values (2.14 to 2.82) reported by previous authors or the value of 2.43 ± 0.29 measured for the seven-hole injector.

- The compressible, underexpanded nozzle exit normalization of the seven-hole injector penetration data produced a slope of 2.76 ± 0.4, which is very close to the value of 2.82 reported by Hill and Oulette [21] for both incompressible and underexpanded jets. Again, the three-hole injector data slope is much lower at 2.26 ± 0.71. The slope, α, for both injector's underexpanded data increases relative to the corresponding subsonic values.
- The inclusion of the discharge coefficient in the nozzle exit, θ normalization method caused the data to collapse approximately ± 2.0% better than when the discharge coefficient was ignored. The value of the mean slope for the three-hole injector data remained approximately a factor of two smaller than the corresponding mean slope for the seven-hole injector data.
- The best method at collapsing the three-hole injector's underexpanded data according to the relative confidence intervals is the PMD parameter method that does include jet angle variation. The relative confidence interval represents ±21.9% of the mean slope value. The nozzle exit, θ method produced a similar value of ±25%.
- The best method at collapsing the seven-hole injector's underexpanded data is the nozzle exit parameter method. The relative confidence interval represents ±14.5% of the mean slope value. The PMD method produced a similar value of ±18.0%.

- Finally, the methods that include the jet angle in the time and length scales cause the nondimensional data to collapse worse than their counterparts where the angle is not included. This is most likely due to the difficulty in obtaining reliable jet angle measurements as discussed above, which make it impossible to properly make any conclusions about the methods that include the variance of the jet angle.

6.0 Conclusions and Recommendations

6.1 Conclusions

Injections from four prototype, multi-hole, high pressure gaseous injectors into a constant volume chamber were visualized using two high frame rate schlieren systems. A Z-type schlieren system was used to investigate the jet structure and morphology, most importantly the penetration rate. A double-pass schlieren system was used to further investigate the interaction between the individual plumes and provide more information about the jet structure. Combined, the two views provide a qualitative view of the entire structure of the flow patterns produced by the multi-hole injectors.

The schlieren systems had sufficient sensitivity to allow expansion wave structures outside of the nozzle to be visualized with hydrogen injection into a nitrogen ambient, helium injected into nitrogen, and with nitrogen injected into nitrogen. The latter was performed to confirm that the observed structures were independent of the mixing process. The spacing of the periodic structures that were identified was found to scale directly with the ratio of the nozzle exit pressure to the chamber pressure. A similar scaling has been observed previously for the barrel shock length.

The jet tip penetration rate was measured for a wide range of injection pressures and chamber densities, and was found to increase with injection pressure and decrease with increasing chamber density. A square-root fit time correction was used to properly shift the data back to the initiation of injection. It was also determined that the penetration rate was similar when either hydrogen or helium were used as the injection medium.

The angle of the quasi-steady region of the jet was measured to determine its effect on the physical processes within the jet. The main issue with measuring the jet angle was isolating the jet from the background of each image. Two methods were utilized to determine the jet outline and both provided angle data that contained a significant amount of scatter. Two main reasons were assumed to cause this scatter. First, the schlieren system's sensitivity includes extraneous clouds of injected fluid that are not part of the jet and artificially increase the measured jet angle value for particular runs. Second, the methods used to isolate the jet either over- or under-identify the jet outline in an inconsistent fashion.

Two injector characteristics, the discharge coefficient and rate shape, were measured to investigate the performance of each injector. The discharge coefficients for the seven- and thirteen-hole injectors ranged from 0.28 to 0.33 and from 0.19 to 0.22 for the three- and nine-hole injectors. The rate shape was also determined from transient pressure measurements during injection. The injector excited vibration of the piezoelectric transducer at its natural frequency and made quantitative results difficult to process. Through filtering of the pressure traces, the injector was found to immediately become choked upon opening, maintain a constant pressure rise, and therefore a constant mass flow rate, during injection, and finally close quickly. No abnormal transients were found that could ultimately lead to anomalous behavior in the penetration data.

Five jet-scaling models were used to investigate the far-field behavior of jets. Nondimensional length and time coordinates were formed, and all of the data were found to follow a linear relationship between the nondimensional length and the square root of the nondimensional time for all of the analyzed scaling relations. The individual models

each used or included different jet properties to normalize the jet penetration rate data. Traditionally, nozzle exit properties were used to nondimensionalize jet data, with some investigators including additional characteristics, such as; the jet angle variation, or the effects of the discharge coefficient, to further collapse their nondimensional data. All of these normalization methods were investigated and the collapse of the slopes of individual runs was quantified. Additional models were developed and analyzed to incorporate the expansion and shock processes that occur outside the nozzle exit for underexpanded jets. It was determined that the expansion model that incorporated the variation in jet angle (PMD,θ model) collapsed the three-hole injector slope data to within ±21.9% of the mean slope value, the best of all methods tested. The seven-hole data collapsed best when only the nozzle exit properties were used to nondimensionalize the data with jet angle and discharge coefficient effects being ignored. The slope collapse was determined to be within ±14.5% of the mean slope value. It should be noted that the significant scatter in the jet angle measurements make it impossible to properly access all methods that include jet angle variation in their scaling relations. In the end, no superior method was found to collapse the penetration rate data. The main issue is that the mean slopes differ by approximately a factor of two between the three- and seven-hole injectors.

6.2 Recommendations

The significant scatter in the jet angle measurements should be addressed by developing a more consistent method of isolating the jet from the background in the collected images. A more statistical approach could produce better, more realistic results. One method would be to develop a correlation function for the same pixel location as a

function of time. Pixel locations that are uncorrelated throughout time would be inside the jet, while the remaining pixels would be considered as part of the background.

It would also be advantageous to compare the flow results from the three- and seven-hole injectors to data obtained from an injector with a single nozzle hole. The three- and seven-hole injectors did allow for single jets to be isolated, but jet-to-jet interactions in the flowfield may lead to changes in penetration behavior. Data from a single-hole injector would provide a baseline for other data to be compared to.

Although, the main goal of studying the rate shape was achieved, that the injector displayed "top hat" behavior with respect to the mass flow rate, the large amount of noise in the data obscured the quantitative results. Different transducer-to-chamber linkages should be investigated to damp out the high-amplitude frequencies that are initiated by the injector. Additional pressure transducers with higher natural frequencies could alternatively be used to obtain cleaner pressure data.

Finally, high magnification imaging of the near-nozzle portion of the flow field would provide more information on the complex flow exiting each nozzle hole. Better measurements of the dimensions of the barrel shock structure along with how many times these structures repeat and for how far downstream could provide details to a better, more physically realistic model of underexpanded transient jets.

Appendix

A.1 Jet Angle Measurement Derivations

A.1.1 Jet Angle Including Jet Origin

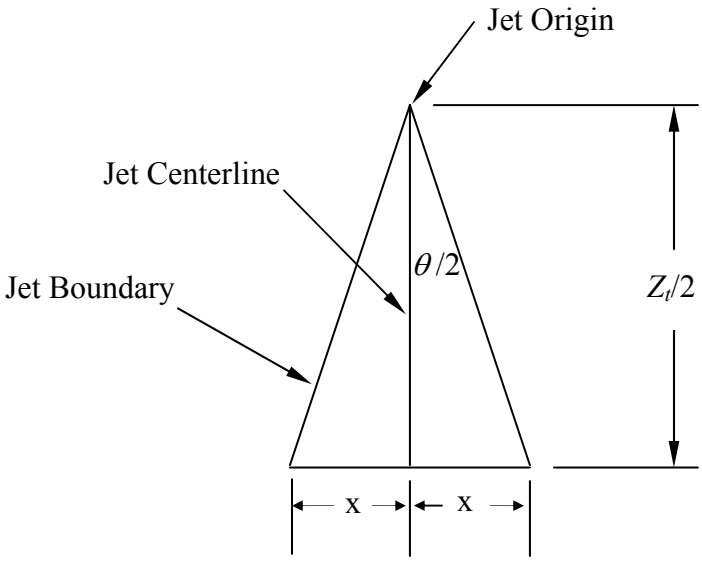

$$\tan\frac{\theta}{2} = \frac{x}{Z_t/2} \tag{A.1}$$

$A_{P,Z_t/2} \equiv$ projected area inside approximated jet geometry up to $Z_t/2$.

$$A_{P,Z_t/2} = x\left(Z_t/2\right) \tag{A.2}$$

Rearranging

$$x = \frac{A_{P,Z_t/2}}{Z_t/2} \tag{A.3}$$

$$\tan\frac{\theta}{2} = \frac{A_{P,Z_t/2}}{\left(Z_t/2\right)^2} \tag{A.4}$$

A.2.2 Jet Angle Excluding Jet Origin

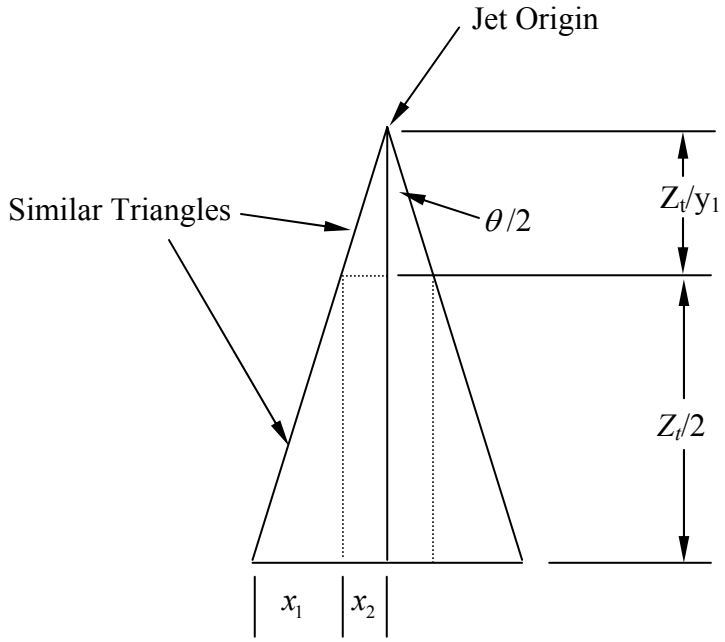

$$\tan\frac{\theta}{2} = \frac{x_1}{Z_t / 2} \tag{A.5}$$

$$\tan\frac{\theta}{2} = \frac{x_2}{Z_t / y_1} \tag{A.6}$$

Rearranging

$$x_2 = \tan\frac{\theta}{2}\left(\frac{Z_t}{y_1}\right) \tag{A.7}$$

$A_{P,Z_t/2} \equiv$ projected area inside approximated jet geometry from $\left(\frac{Z_t}{y_1}\right)$ to $\left(\frac{Z_t}{2}+\frac{Z_t}{y_1}\right)$

$$A_{P,Z_t/2} = \frac{Z_t}{2}(x_1) + 2\left(\frac{Z_t}{2}\right)x_2 \tag{A.8}$$

Rearranging

$$x_1 = \frac{A_{P,Z_t/2} - Z_t x_2}{Z_t / 2} \tag{A.9}$$

Combining with eq. (A.5)

$$\tan\frac{\theta}{2}=\frac{A_{P,Z_t/2}-Z_t x_2}{\left(Z_t/2\right)^2} \tag{A.10}$$

Combining with eq. (A.8)

$$\tan\frac{\theta}{2}=\frac{A_{P,Z_t/2}-Z_t\tan\left(\frac{\theta}{2}\right)\left(\frac{Z_t}{y_1}\right)}{\left(Z_t/2\right)^2} \tag{A.11}$$

Simplifying

$$\tan\frac{\theta}{2}=\frac{A_{P,Z_t/2}}{\left(Z_t/2\right)^2}-4\left(\frac{\tan\left(\theta/2\right)}{y_1}\right) \tag{A.12}$$

Simplifying further

$$\tan\frac{\theta}{2}=\frac{1}{1+4/y_1}\left(\frac{A_{P,Z_t/2}}{\left(Z_t/2\right)^2}\right) \tag{A.13}$$

A.2 Example Jet Angle Measurements

A.2.1 Three-hole Injector

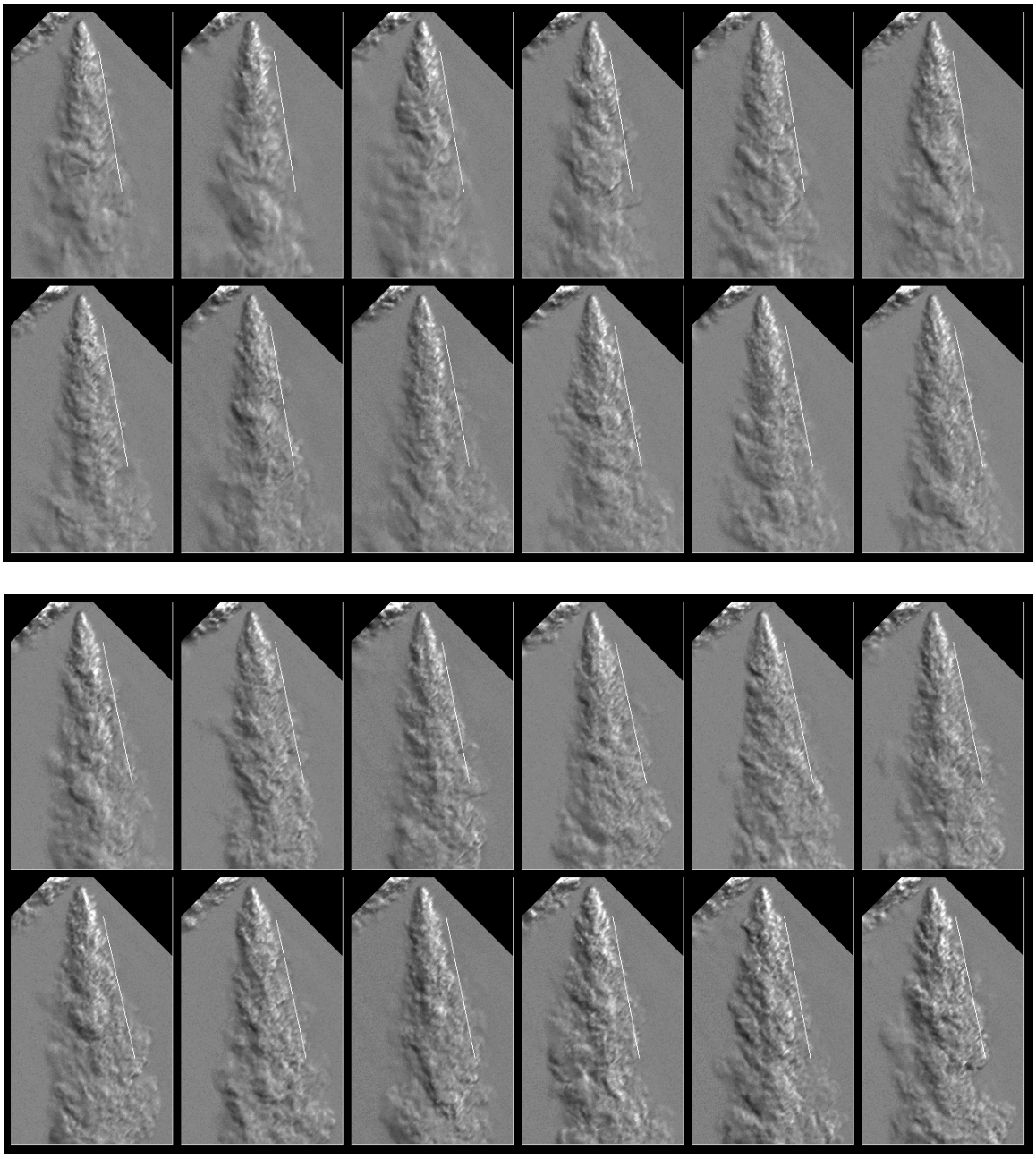

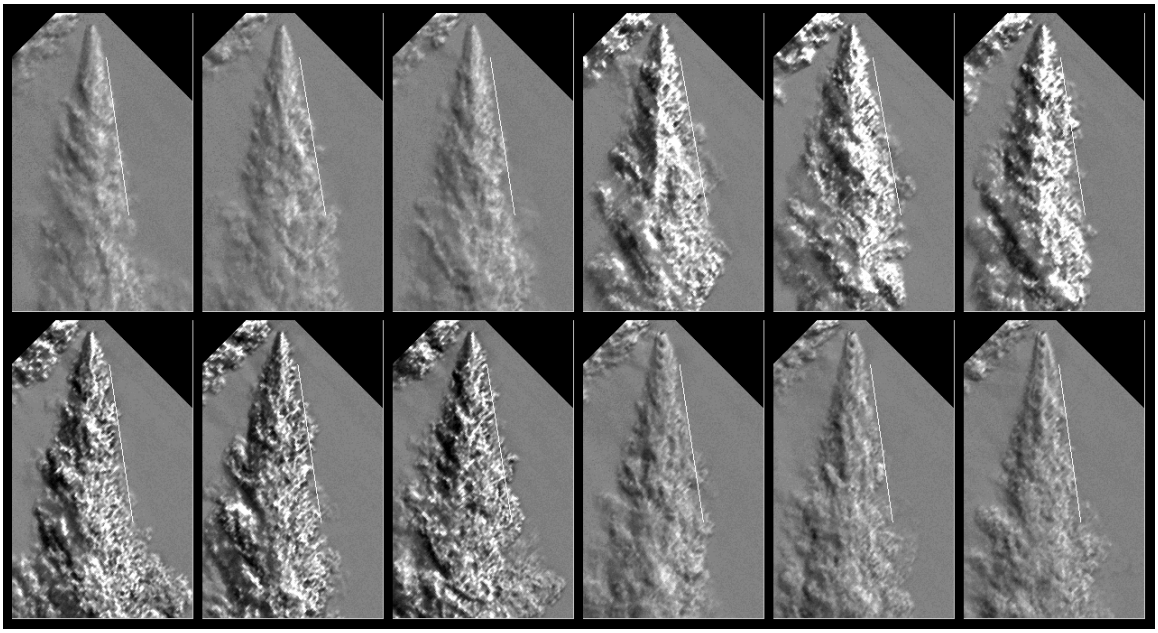

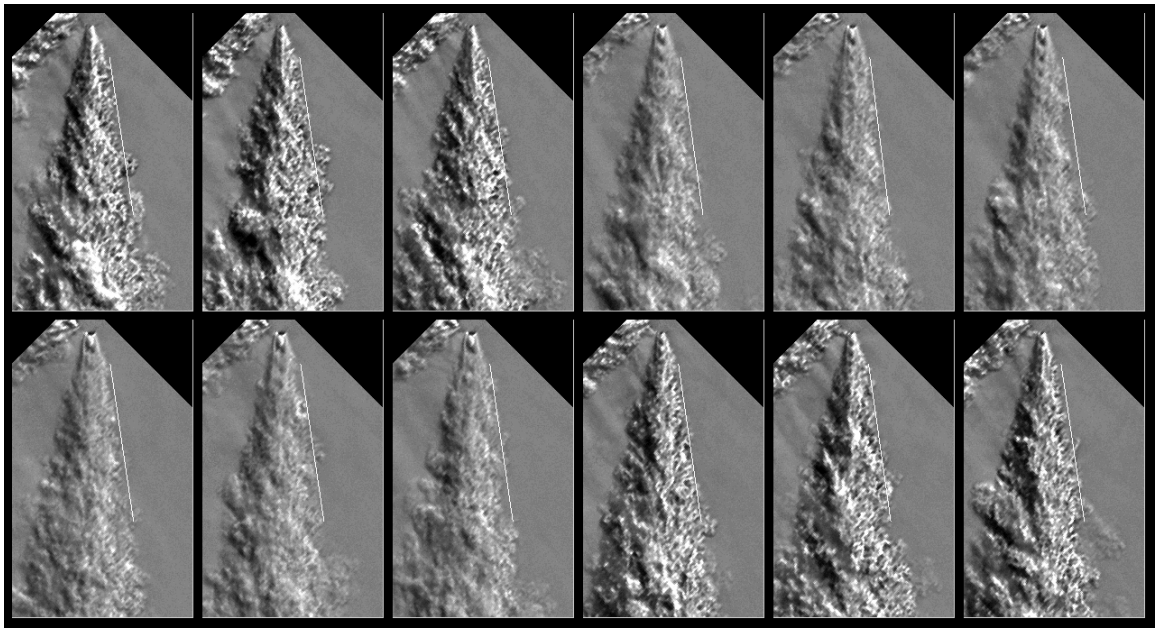

A.2.2 Seven-hole Injector

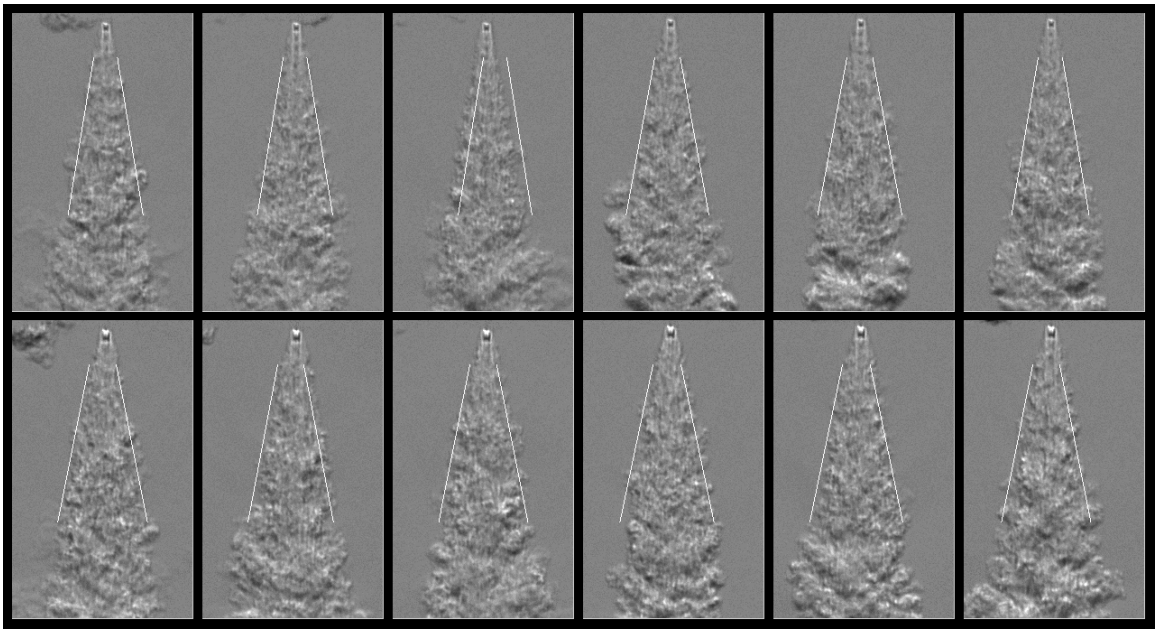

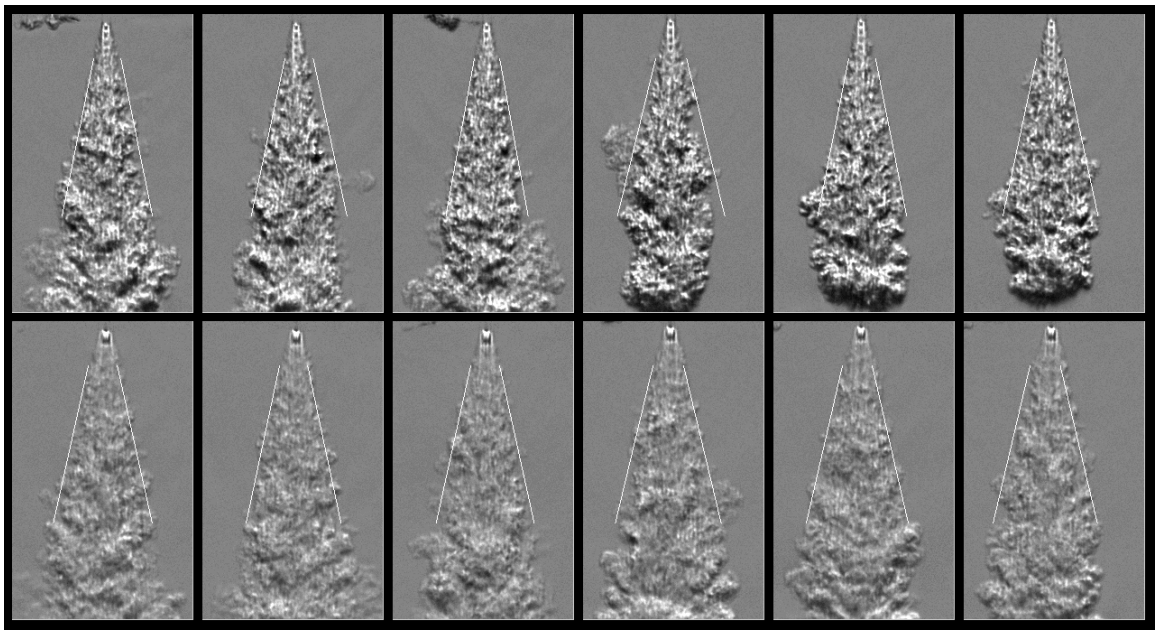

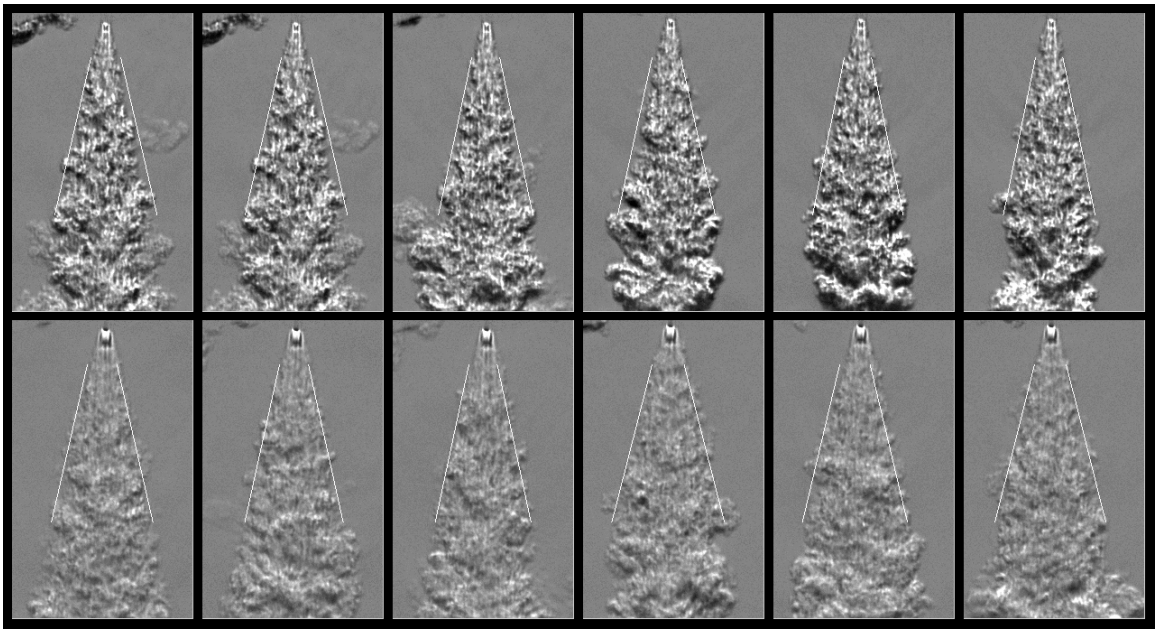

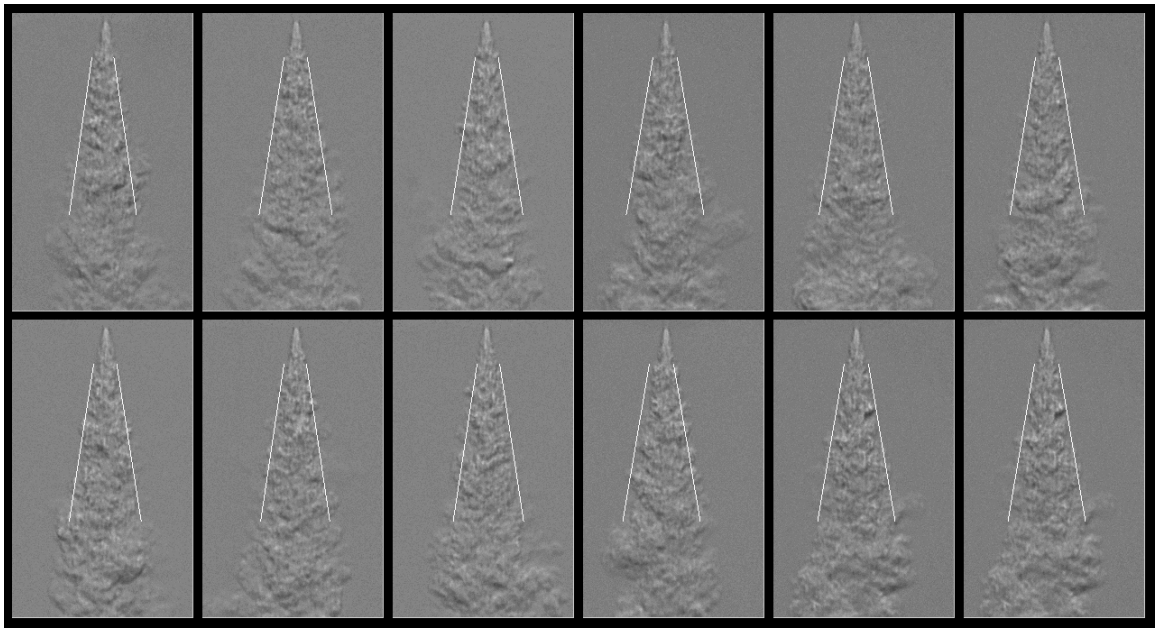

Cited References

1. Das, M., L., "Hydrogen engines: a view of the past and a look into the future," *Int. J. Hydrogen Energy*, Vol. 15, No. 6, pp. 425-443, 1990

2. Stockhausen, W. F., Natkin, R. J., Kabat, D. M., Reams, L., Tang, X., Hashemi, S., Szwabowski, S. J., Zanardelli, V. P., "Ford P2000 hydrogen engine design and vehicle development program," SAE Paper 2002-01-0240, 2002.

3. Wimmer, A., Wallner, T., Ringler, J. and Gerbig, F., "H2-Direct Injection~A Highly Promising Combustion Concept," SAE Paper 2005-01-0108, 2005.

4. Tang, X., Kabat, D. M., Natkin, R. J., Stockhausen, W. F. and Heffel, J., "Ford P2000 Hydrogen Engine Dynamometer Development," SAE Paper 2002-01-0242, 2002.

5. Eichlseder, H., Wallner, T., Freymann, R., Ringler, J., "The potential of hydrogen internal combustion engines in a future mobility scenario," SAE Paper 2003-01-2267, 2003.

6. Berckmuller, M., Rottengruber, H., Eder, A., Brehm, N., Elsasser, G., Muller-Alander, G., and Schwarz, C., "Potentials of a charged SI-hydrogen engine," SAE Paper 2003-01-3210, 2003.

7. Rajaratnam, N., Turbulent Jets, Elsevier Scientific Publishing Company, Amsterdam, 1976.

8. Ouellette, P., 1996, "Direct Injection of Natural Gas for Diesel Engine Fueling," Ph.D. thesis, Department of Mechanical Engineering, University of British Columbia.

9. Ricou, F.P. and Spalding, D.B., "Measurements of entrainment by axisymmetrical turbulent jets, *J. Fluid Mech.*, 11, pp. 21-32, 1961.

10. Birch, A.D., Brown, D.R., Dodson, M.G., Thomas J.R., "The turbulent concentration field of a methane jet," *J. Fluid Mech*., vol. 88, pp. 431-449, 1978.

11. Abraham, J., "Entrainment characteristics of transient gas jets," *Numerical Heat Transfer, Part A*., 30, pp. 3478-364. 1996.

12. Ra, Y., Kong, S.C., Reitz, R.D., Rutland, C.J., Han, Z., "Multidimensional modeling of transient gas jet injection using coarse computational grids," SAE Paper 2005-01-0208, 2005.

13. Turner, J.S., "The starting plume in neutral surroundings, *J. Fluid Mech*,, 13, pp.356-368, 1962.

14. Abramovich S., Solan, A., "The initial development of a submerged laminar round jet," *J Fluid Mechanics*, Vol 59 pp. 791-801, 1973.

15. Sato, H., Sakao, F., "An experimental investigation of the instability of a two-dimensional jet at low Reynolds numbers," *J. Fluid Mech.,* vol. 20, pp. 337-352, 1964.

16. Witze, P.O., “The impulsively started incompressible turbulent jet,” Sandia Laboratories Report, SAND80-8617.

17. Lahbabi, F. Z., Botee, J., Nuglisch, H. J., and Charnay, G., 1993, "Analysis of Starting and Steady Turbulent Jets by Image Processing Techniques," *Experimental and Numerical Flow Visualization*, ASME Fluids Engineering Division, Vol. 172, pp. 315–321.

18. Johari, H., Zhang, Q., Rose, M., Bourque, S., “Impulsively started turbulent jets,” *AIAA J*., **35** pp. 657-662, 1997.

19. Joshi, A., Schreiber, W., “An experimental examination of an impulsively started incompressible turbulent jet,” *Experiments in Fluids,* **40** pp.156-160, 2006.

20. Abraham, J., Magi, V., MacInnes, J., Bracco, F.V., “Gas versus spray injection: which mixes faster?,” SAE Paper 940895, 1994.

21. Hill, P., G., Ouellette, P., “Transient turbulent gaseous fuel jets for diesel engines,” *ASME J. Fluids Eng.,* **121**, pp. 93-101, 1999.

22. Rizk, W., “Experimental studies of the mixing processes and flow configurations in two-cycle engine scavenging,” *Proceedings of the IMECHE, Series E*, 172, pp.417-424, 1958.

23. Ouellette, P., Hill, P., G., “Turbulent transient gas injections,” *ASME J. of Fluids Eng*., vol. 122, pp. 743-751, 2000.

24. Schlichting, H., Boundary Layer Theory, McGraw-Hill, New York, 1976.

25. Naber, J.D. and Siebers, D.L. “Effects of gas density and vaporization on penetration and dispersion of diesel sprays,” SAE Paper 960034, 1996.

26. Pai, S-I, Fluid dynamics of jets, D. Van Nostrand Company, Inc., 1954.

27. Cumber, P.S., Fairweather, M., Falle, S.A.E.G., Giddings, J.R., “Predictions of the structure of turbulent, highly underexpanded jets,” *Journal of Fluids Engineering*, Vol. 117, pp. 599-604.

28. Adamson Jr., T.C., Nicholls, J.A., “On the structure of jets from highly underexpanded nozzles into still air,” *Journal of the Aero/Space Sciences,* January, 1959, pp.16-24.

29. Ewan, B.C.R., Moodie, K., “Structure and velocity measurements in underexpanded jets,” *Combust. Sci. and Tech.,* vol. 45, pp. 275-288, 1986.

30. Kleinstein, G., “Mixing in turbulent axially symmetric free jets,” Journal of Spacecraft, **1**(4), pp. 403, 1964.

31. Warren, W.R., “An analytical and experimental study of compressible free jets,” HSE Report No. HSE/SRD/PD039/WPI, 1957.

32. Eggins, P.L., Jackson, D.A., “Laser doppler velocity measurements in underexpanded free jet,” *J. Phys.*, vol 7, 1984.

33. Miyake, M., Biwa, T., Endoh, Y., Shimotsu, M., Murakami, S. and Komoda, T, "The development of high output, highly efficient gas burning diesel engines," Paper D11.2, CIMAC Conference, Paris, 1983.

34. Chepakovich, A., "Visualization of transient single- and two-phase jets created by diesel engine injectors," M.A.Sc. thesis, University of British Columbia, 1993.

35. Settles, G., Schlieren and shadowgraph techniques : visualizing phenomena in transparent media, New York, Springer, 2001.

36. Tsujimura, T., Mikami, S., Achiha, N., Tokunaga, Y., Senda, J., Fujimoto, H., "A study of direct injection diesel engine fueled with hydrogen," SAE Paper 2003-01-0761.